

ASSEMBLY, CHARACTERIZATION, AND
OPERATION OF LARGE-SCALE TES DETECTOR
ARRAYS FOR ACTPOL

CHRISTINE GOODWIN PAPPAS

A DISSERTATION
PRESENTED TO THE FACULTY
OF PRINCETON UNIVERSITY
IN CANDIDACY FOR THE DEGREE
OF DOCTOR OF PHILOSOPHY

RECOMMENDED FOR ACCEPTANCE
BY THE DEPARTMENT OF
PHYSICS
ADVISER: PROFESSOR SUZANNE STAGGS

JANUARY 2016

© Copyright by Christine Goodwin Pappas, 2015.

All rights reserved.

Abstract

The Polarization-sensitive Receiver for the Atacama Cosmology Telescope (ACTPol) is designed to measure the Cosmic Microwave Background (CMB) temperature and polarization anisotropies on small angular scales. Measurements of the CMB temperature and polarization anisotropies have produced arguably the most important cosmological data to date, establishing the Λ CDM model and providing the best constraints on most of its parameters. To detect the very small fluctuations in the CMB signal across the sky, ACTPol uses feedhorn-coupled Transition-Edge Sensor (TES) detectors. A TES is a superconducting thin film operated in the transition region between the superconducting and normal states, where it functions as a highly sensitive resistive thermometer. In this thesis, aspects of the assembly, characterization, and in-field operation of the ACTPol TES detector arrays are discussed. First, a novel microfabrication process for producing high-density superconducting aluminum/polyimide flexible circuitry (flex) designed to connect large-scale detector arrays to the first stage of readout is presented. The flex is used in parts of the third ACTPol array and is currently being produced for use in the AdvACT detector arrays, which will begin to replace the ACTPol arrays in 2016. Next, we describe methods and results for the in-lab and on-telescope characterization of the detectors in the third ACTPol array. Finally, we describe the ACTPol TES $R(T,I)$ transition shapes and how they affect the detector calibration and operation. Methods for measuring the exact detector calibration and re-biasing functions, taking into account the $R(T,I)$ transition shape, are presented.

Acknowledgements

I would like to thank first and foremost my wonderful adviser, Prof. Suzanne Staggs. Prof. Lyman Page has also been very kind and supported my research. I would also like to thank my thesis committee, Professors William Bialek, Bill Jones, Lyman Page, and Suzanne Staggs.

The Princeton Physics Department has great staff who have helped me almost daily with my research. I would like to thank Glen Atkinson, Bill Dix, Geoff Gettelfinger, Darryl Johnson, Angela Lewis, Ted Lewis, and Steve Lowe for their help and kindness.

The procedures for assembling the ACTPol detectors laid out in Chapter 2 of this thesis were developed under the advisement of Bert Harrop, who contributed countless hours of support to our group's projects. The development of the flex process discussed in Chapter 3 was also a collaboration with Bert Harrop. Pat Watson and Joe Palmer of the Princeton MNFL also provided helpful advice and assistance with MNFL tools.

The assembly and testing of the three ACTPol detector arrays was a group effort with Emily Grace, Patty Ho, Dr. Laura Newburgh, and Sara Simon. Our undergraduates Joshua Millings, Kevin Mizes, Prajwal Niraula, and Albert Zhou also assisted this research.

I have enjoyed the company and support of the many students and postdocs in our lab during my research and thesis writing, including Steve Choi, Kevin Crowley, Emily Grace, Patty Ho, Yiaqiong Li, Laura Newburgh, Prajwal Niraula, Maria Salatino, and Sara Simon.

I would like to thank my grandparents, my parents, Lauren, and James for their enthusiastic support of whatever I choose to do. Most of all, I would like to thank my partner Lukas, who has been there for me through all of graduate school.

To Lukas.

Contents

Abstract	iii
Acknowledgements	iv
List of Tables	x
List of Figures	xi
1 Introduction	1
1.1 The Cosmic Microwave Background (CMB)	2
1.1.1 Secondary CMB Anisotropies	5
1.1.2 CMB Polarization	6
1.2 The ACTPol Instrument	6
1.3 ACTPol Science Goals	8
2 ACTPol detector arrays and readout: Overview and assembly	11
2.1 Pixels	12
2.2 TES Bolometers	13
2.3 Detector array readout: SQUID time-domain multiplexing	16
2.3.1 Measuring TES I, V, and R with the ACTPol readout	20
2.4 ACTPol detector array assembly	25
2.4.1 Detector arrays and readout: physical design	25
2.4.2 Assembly process overview	29
2.4.3 Wedge Wire bonding	31

2.4.4	Assembly with Tech-Etch flex	31
2.4.5	Assembly with Princeton flex	33
2.4.6	Assembly yield	33
3	Flex fabrication for ACTPol and Advanced ACTPol	35
3.1	Introduction	35
3.2	Flex Design	37
3.2.1	Maximum Trace Density	37
3.2.2	Flex Structure	42
3.3	Flex fabrication process	45
3.3.1	Silicon passivation layer	45
3.3.2	Fabricating and patterning polyimide films	46
3.3.3	Depositing and patterning metal on polyimide	56
3.3.4	Release of polyimide from silicon substrate	57
3.3.5	AdvACT flex fabrication process summary	61
3.4	Flex Performance	62
3.4.1	Superconducting properties	62
3.4.2	Electrical yield	64
3.4.3	Ease of assembly and wire bond strength	64
3.4.4	Robustness under mechanical and cryogenic stress	65
3.5	Conclusion	65
3.6	Acknowledgements	65
4	PA3 Detector Array	67
4.1	PA3 array overview	67
4.2	Dark measurements	68
4.2.1	Dark measurement methods	70
4.2.2	TES critical temperature	73

4.2.3	Thermal conductivity between TES island and bath	74
4.2.4	P_{sat} at operating bath temperature	76
4.3	Detector optical efficiency	79
4.3.1	Lab measurements of FH4 optical efficiency	80
4.3.2	Optical efficiencies on telescope, from atmosphere	83
4.4	Conclusion	86
5	ACTPol TES $R(T, I)$ transitions	88
5.1	Introduction	88
5.2	Physical models of the TES $R(T, I)$ transition	89
5.2.1	Comparison with Data	90
5.3	Measurement of the $R(T, I)$ function from IV curves	92
5.4	Detector Responsivity	94
5.4.1	Responsivity as a function of I_{bias} and TES resistance	95
5.4.2	Measuring $\%R_n$ with bias steps	102
5.5	Responsivity measurement accuracy	105
5.5.1	Bias step resistance measurement accuracy	105
5.5.2	Responsivity function accuracy	108
5.5.3	Improvements to ACTPol responsivity calculation procedure	112
5.6	Detector biasing with bias step measurements	114
5.7	Conclusions and future work	115
6	Conclusions and Future Work	118
A	Detector and readout diagnostic techniques	122
A.1	Warm diagnostics and pre-screening	124
A.2	Cold diagnostics	126
A.2.1	Cold diagnostics: Critical lines	126
A.2.2	Cold diagnostics: Individual TES circuits	129

B Flex Fabrication Recipes	130
B.1 Aluminum oxide ALD	130
B.2 Oxygen plasma etch of polyimide	131
B.3 DRIE silicon etch	132
C Lab optical efficiency measurement apparatus	133

List of Tables

3.1	Maximum trace density	42
5.1	Responsivity calculation method definitions	109
A.1	Cold diagnosis of critical lines	126
B.1	ALD recipe for 1000 atomic layers of Al ₂ O ₃ : Step 1	131
B.2	ALD recipe for 1000 atomic layers of Al ₂ O ₃ : Step 2	131
B.3	ALD recipe for 1000 atomic layers of Al ₂ O ₃ : Step 3	131
B.4	PlasmaTherm 790 RIE oxygen plasma etch recipe	132
B.5	PVA TePla M4L ICP oxygen plasma etch recipe	132
B.6	Samco 800 recipe 3	132

List of Figures

1.1	CMB polarization, temperature anisotropy measurement status 2015	3
1.2	Atacama Cosmology Telescope and ACTPol receiver diagrams	8
2.1	PA2, PA3 pixels	12
2.2	TES island	14
2.3	TES bolometer bias circuit	15
2.4	SQUID TDM diagram	17
2.5	SQUID V-phi curve	18
2.6	IV curve example	23
2.7	Mutual inductance ratio data	25
2.8	ACTPol PA3 detector Array	26
2.9	Assembled ACTPol hex wafer	28
2.10	Assembled ACTPol semihex wafer	29
3.1	Minimum bond pad pitch tests	39
3.2	Flex bond pad spacing	40
3.3	Wire bonds on flex	41
3.4	Indium bump bonded flex	43
3.5	Flex diagram	44
3.6	ACTPol flex	45
3.7	AdvACT flex	46

3.8	Polyimide shadow mask patterning	51
3.9	Polyimide grassy residue	55
3.10	AdvACT fab process overview	61
3.11	Wire bond pull strength	64
4.1	FH4 lab data G fit example	71
4.2	On-telescope measurements of G	72
4.3	PA3 Array T_c data	74
4.4	PA3 Array κ data	75
4.5	PA3 P_{sat} at $T_{bath}=123.5$ mK	77
4.6	PA3 array biasability vs. optical loading, T_{bath}	78
4.7	FH4 simulated band pass	80
4.8	FH4 optical efficiency measurement example	81
4.9	FH4 lab optical efficiency results	82
4.10	Relative optical efficiency measurement example	83
4.11	Optical efficiency normalization with FH4 lab data	84
4.12	Telescope optical efficiency results	85
4.13	PA3 FTS spectra	86
5.1	Low bias current $R(T, I)$	91
5.2	$R(T, I)$ function, PA3 FH4 col3 row4	93
5.3	Responsivity data example	99
5.4	$R(T, I)$ PA2 col7 row17	100
5.5	$R(T, I)$ PA2 col11 row0	101
5.6	Bias step fit function	106
5.7	Bias step resistance measurement results	107
5.8	Propagation of error in resistance to responsivity	109
5.10	Uranus responsivity approximation error	111

6.1	Thermal Pickup	120
A.1	Column critical lines wiring from MCE to detector PCB	123
A.2	Row select wiring from MCE to detector PCB	125
A.3	Individual TES circuit cold diagnosis flow chart	128
C.1	Optical efficiency apparatus: Detector assembly	134
C.2	Optical efficiency apparatus: Cold load	135
C.3	Optical efficiency apparatus: filters	135

Chapter 1

Introduction

ACTPol is the first polarization-sensitive receiver for the Atacama Cosmology Telescope (ACT). It is designed for precision measurements of temperature and polarization anisotropies in the Cosmic Microwave Background (CMB), radiation that was emitted only 380,000 years after the Big Bang. By measuring the CMB we can observe the state of the very early universe at the time the CMB was released. With ACTPol, it is also possible to observe the universe at later times because the CMB signal is slightly altered as it passes by intervening matter, further constraining cosmological parameters. Galaxy clusters are observed through gravitational lensing of the CMB photons by massive structures and the Sunyaev-Zeldovich (SZ) effect, interaction between the CMB photons and the hot ionized gas in the intracluster medium as they pass through.

The focus of this thesis is on the ACTPol receiver detector arrays, which convert the CMB optical signal into electrical signals we can record. To measure the very small CMB anisotropy signal, we use highly sensitive feedhorn-coupled TES bolometers, read out with a time-division SQUID multiplexing system. In the remainder of this introductory chapter, we introduce the physics of the CMB anisotropies and summarize the science goals of the ACTPol experiment. The detectors, the SQUID

readout system, and the assembly of the detectors with the readout are described in detail in Chapter 2.

In Chapter 3, we present a novel microfabrication process for producing high-density superconducting cables with a wedge wire bonding interface, which we use to connect the detectors to the first stage of readout. These cables were fielded successfully in parts of the third ACTPol detector array and will also be used in the Advanced ACTPol detector arrays, which will begin to replace the ACTPol detector arrays in 2016.

In Chapter 4, we discuss aspects of the third ACTPol detector array performance and detector property measurement methods. Finally, in Chapter 5, we discuss the R(T,I) transitions of the ACTPol TESes and how the transition shape affects detector operation and performance. The measurement methods presented are used to inform the calibration of the CMB data time streams. In the future, they will also be useful for screening detectors, improving detector operation, and possibly for filtering out systematic noise from CMB data.

1.1 The Cosmic Microwave Background (CMB)

After the Big Bang, the universe was so hot that the photons, electrons, and nuclei formed a tightly bound primordial plasma. Any bound atoms that formed were quickly ionized again by the high-energy photons. It took about 380,000 years for the universe to cool enough for bound atoms to begin to form. The photons then decoupled from the baryonic matter and traveled mostly unimpeded through the universe to our telescopes.

Measuring the CMB allows us to observe the state of the universe at the time of decoupling. CMB experiments have measured a perfect black body spectrum of radiation at a temperature that is nearly constant over the sky, of about 2.73K [30].

The temperature fluctuates across the sky with a very small amplitude, on the order of one part in 10,000. This tells us that the very early universe had little structure, with only small spatial fluctuations in mass-energy density. Over time, these very small fluctuations grew under gravitational collapse into the large-scale structure of the universe we observe today.

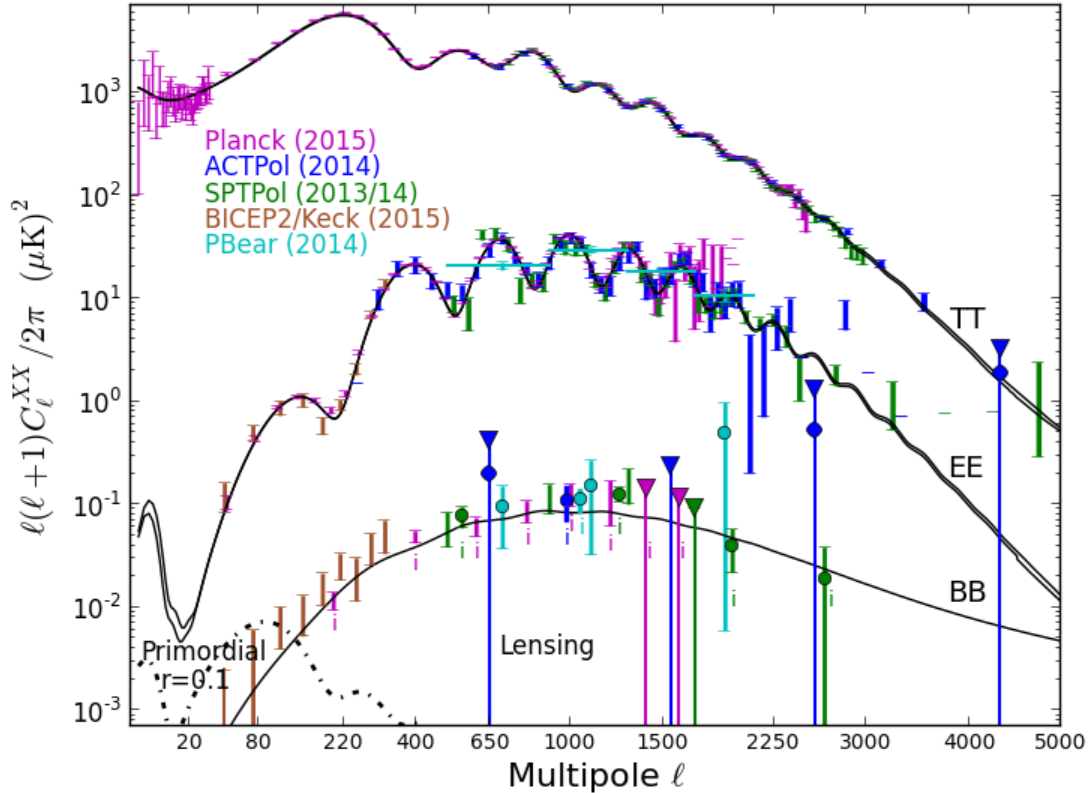


Figure 1.1: The current status of measurements of the TT, EE, and BB CMB anisotropy spectra as of May 2015. The CMB temperature (TT) anisotropy spectrum is shown for ACT [24], Planck [6], and SPT [86]. The E-mode polarization (EE) anisotropy spectrum is shown for ACTPol [71], BICEP2/Keck Array [5], Planck [6], POLARBEAR [4], and SPTPol [22]. Direct measurements of the B-mode polarization (BB) spectrum are shown for ACTPol [71], BICEP2/Keck Array [5], Planck, POLARBEAR [4], and SPTPol [52]. Indirect measurements of the BB signal, indicated with an "i" below the data point, are shown for ACTPol [90], Planck [3], POLARBEAR [1], and SPTPol [40]. Figure courtesy Lyman Page.

The origin of the small anisotropies observed in the CMB temperature can be understood by looking more closely at their structure. The anisotropies are not

random, but have a distinct spectrum as a function of l when decomposed over the sky into the spherical harmonics Y_l^m . The highest amplitude fluctuations are on angular scales of about one degree, or $l = 200$, and the amplitude continues to fluctuate in a series of peaks and troughs as l increases. (See Fig. 1.1)

Although there are many different inflation and alternative models of the beginning of the universe, we know from the CMB that small spatial fluctuations in energy density were somehow created at the beginning of the universe. Over time, these perturbations created sound waves in the primordial plasma due to competing photon pressure and gravitational compression. The pattern of peaks and troughs we observe in the CMB temperature anisotropy spectrum is due to these sound waves. The higher temperature spots of the CMB sky are where the primordial plasma was compressed and hotter at the time of decoupling, and the lower temperature regions are where it was rarefied and cooler. At decoupling, the plasma sound waves with some wavelengths were maximally compressed, others were maximally rarefied, and some are right in between- maximally uniform. These give rise to the odd peaks, the even peaks, and the troughs, respectively in the power spectrum [45].

Measurements of the CMB anisotropy spectrum have provided arguably the most powerful cosmological information of cosmology experiments to date. With the release of the WMAP satellite data, the Λ CDM model was firmly established. Because the exact position and height of the peaks and troughs in the CMB anisotropy spectrum depends on the values of the Λ CDM model parameters, the spectrum can be fit to constrain them.

The primordial CMB anisotropies are especially powerful when combined with information about the universe at later times to break degeneracies between the parameters of the Λ CDM model, such as between curvature and dark energy. The measured distribution of matter at later times is consistent with predictions of how the CMB anisotropies would evolve over time.

1.1.1 Secondary CMB Anisotropies

While the CMB photons mostly flow freely from the surface of last scattering to our telescope, there are small interactions with the ionized gas in galaxy clusters by inverse Compton scattering and gravitational lensing by large mass structures. These secondary anisotropies make measuring the primordial CMB anisotropies somewhat more challenging, but allow us to observe the state of the universe both at the time of decoupling and at later times through the CMB alone.

Gravitational lensing occurs when the CMB photon trajectories are altered by gravitational interaction with large-mass structures between the surface of last scattering and our telescope. Unlike optical galaxy surveys, gravitational lensing directly probes the dark matter distribution rather than the light-emitting baryonic matter. It is also most sensitive to massive structures at higher red shift, of $z=2-4$.

When CMB photons pass through regions of the universe occupied by ionized gas, such as the hot gas between galaxies in a cluster, they are inverse Compton scattered by the electrons. The CMB spectrum is altered from a blackbody with a characteristic signature by this interaction, known as the Sunyaev-Zeldovich (SZ) effect, such that the intensity is higher than a 2.725K blackbody at frequencies above about 218 GHz, and lower than the 2.725K blackbody spectrum at lower frequencies. [14] [18]. The amplitude of the effect depends on the temperature of the ionized gas. Because the effect is redshift independent, it can be used to find high redshift galaxy clusters. The kinetic Sunyaev-Zeldovich (kSZ) effect is a similar effect due to interaction between CMB photons and ionized gas, but its amplitude depends on the velocity of the galaxy cluster along the line-of-sight. Although it is a lower amplitude effect, it allows measurement of the cluster velocity [38].

1.1.2 CMB Polarization

The primordial CMB signal is partially polarized due to scattering of the photons off electrons at the surface of last scattering [46]. Because the polarization of a CMB photon is given by the quadrupole pattern of CMB temperature around it at its point of release, the polarization anisotropies also have a distinct spectrum as a function of l . The polarization pattern is conventionally divided into two orthogonal components with different spatial symmetries, B-modes and E-modes.

Experiments are currently measuring the polarization E-mode (EE) anisotropy spectrum in addition to the temperature (TT) anisotropy spectrum to greater and greater accuracy because the EE spectrum provides a check of our model of the origin of the TT anisotropies, gives us more data to fit cosmological parameters with better precision, and could enable new science [17].

At low- l , very low-amplitude B-mode fluctuations in the polarization spectrum due to tensor perturbations may be a detectable signature of inflation, depending on the energy scale [12]. B-mode polarization is also created by gravitational lensing, which transforms the primordial E-mode polarization signal into B-mode. By combining the lensing signal in temperature and polarization, we can significantly increase the statistical significance of a lensing signal detected in temperature alone. Lensing B-modes were first indirectly detected by SPTpol in 2013 and later by POLARBEAR, BICEP2, and ACTPol [39][1][5][90].

1.2 The ACTPol Instrument

ACTPol is the first polarization-sensitive receiver for the Atacama Cosmology Telescope (ACT). ACT is a 6-meter off-axis Gregorian telescope located on the Cerro Toco Mountain, at an elevation of 5200 meters, in the Atacama Desert, Chile. The telescope's 6-meter primary mirror enables CMB measurements with arc-minute an-

gular scale resolution. Its location was selected for its dry climate and high altitude, which minimize microwave signals from the atmosphere.

Even in ACT's dry climate and high altitude location, the amplitude of atmosphere emission fluctuations is much larger than the amplitude of the CMB anisotropies we are trying to measure. The atmosphere emissions are strongest at the resonant frequency bands of the atmospheric gases' rotational modes, and these regions must be avoided when selecting ACTPol's observing frequency bands. All CMB experiments are also sensitive to contaminating signals from objects well outside of our atmosphere, such as foreground emissions from dust and synchrotron radiation. The amplitude of these contaminating signals also depends on frequency, with synchrotron radiation dominating at lower frequency and dust dominating at higher frequency. We select 150 GHz and 90 GHz observing bands for ACTPol where the CMB signal is strongest in comparison to the contaminating signals from atmosphere emissions, synchrotron radiation, and foreground emissions.

ACT began CMB observations with the millimeter bolometer array camera (MBAC) receiver from 2008 to 2011, then started observations with the polarization-sensitive ACTPol receiver in 2013, which will continue through the 2015 season.¹ The ACTPol upgrade now allows ACT measurements of the CMB polarization anisotropies in addition to the temperature anisotropies with higher sensitivity (signal:noise) than MBAC.

ACTPol can observe with up to three optics tubes cooled to cryogenic temperatures, each with its own polarization-sensitive transition-edge sensor (TES) bolometer detector array. The ACTPol receiver was deployed in 2013 with the first detector array, PA1; PA2 was added before the 2014 observing season; and PA3 was added in 2015. PA1 and PA2 measure radiation in a band centered at 150 GHz, while PA3 features dichroic pixels that measure radiation in both 90 GHz and 150 GHz bands.

¹Before the 2016 season, the ACTPol detector arrays will begin to be replaced by Advanced ACTPol detector arrays.

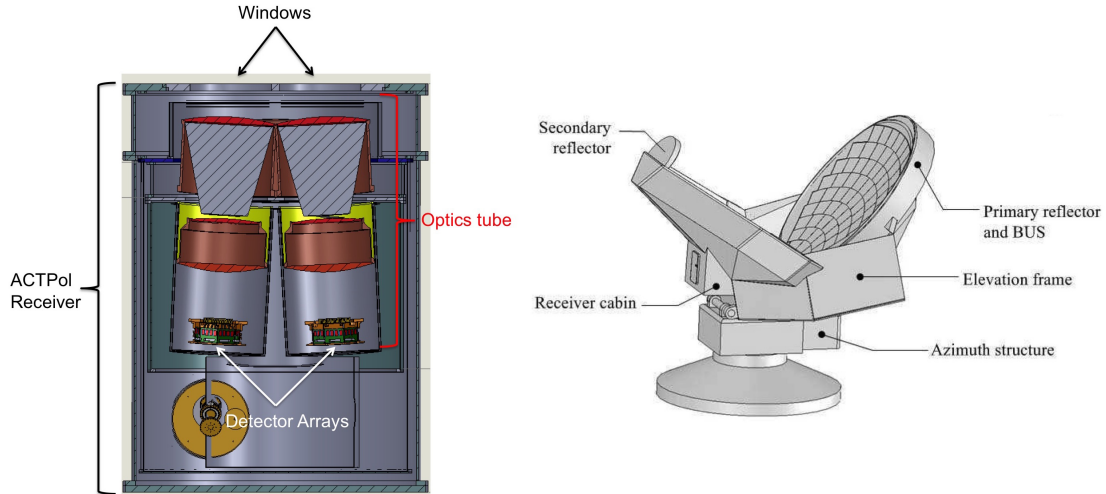


Figure 1.2: *Right:* Diagram of the Atacama Cosmology Telescope (ACT). Light is first reflected off the 6 m primary mirror, then the 2 m secondary mirror, then enters the ACTPol receiver. *Left:* Cross-sectional diagram of the ACTPol receiver. There are three optics tubes, two of which are visible in this diagram. Light enters each optics tube through the window at the top of the diagram, passes through a series of cold filters and lenses, and is finally measured by the detector array.

The detector arrays are cooled to 80-120 mK with a dilution refrigerator [82], instead of a Helium-3 sorption refrigerator with a base temperature of 300 mK like the one used for MBAC, because the thermal noise of the detectors is lower at lower temperatures. The dilution refrigerator also allows for 24-hour-a-day observations, unlike a helium-3 sorption fridge, which needs to be cycled each day, a 9.5 hour-a-day process for MBAC [28].

1.3 ACTPol Science Goals

Precision measurements of the primordial CMB temperature anisotropies by experiments prior to ACTPol such as WMAP, Planck, SPT, and ACT have constrained the cosmological parameters of the Λ CDM model to high accuracy [57] [2] [53] [83]. However, there are still many aspects of the model that are not well understood at the time of writing, for example the nature of dark energy and dark matter, and some

parameters of the model that still need to be measured with higher precision, such as the sum of the neutrino masses. Here, I will give a very brief summary of the science goals of ACTPol. For more details, see Niemack et al [72].

As a ground-based experiment, ACT is more sensitive to CMB temperature and polarization anisotropies at high- l than low- l because atmosphere fluctuations are larger over larger time scales and larger distances across the sky [58]. During the 2015 ACTPol season, PA1 observed some of the time with a prototype spinning half-wave plate that will allow observations of CMB polarization anisotropies at lower l . The spinning half-wave plate modulates the polarized sky signal, allowing the subtraction of noise and atmosphere fluctuations, which are largely unpolarized, at frequencies lower than the modulation frequency. This method was successfully used in the Atacama B-mode Search (ABS) [56] experiment and we also plan to implement it in Advanced ACTPol [42].

By measuring the primordial CMB polarization and temperature anisotropies at high l , ACTPol aims to constrain the number of neutrino species, the sum of the neutrino masses, the primordial helium abundance, and the running of the spectral index, n_s . The primordial CMB polarization and temperature spectra, shown in Fig. 1.1, are sensitive to each of these parameters at high- l . For example, the larger the primordial helium abundance, the more the fluctuations in the CMB temperature anisotropy spectrum at high- l are suppressed. The high- l temperature fluctuations are smeared out due to photons diffusing to neighboring areas over the time length of the decoupling process, a phenomenon known as Silk Damping [84]. Because the helium atoms recombine before the hydrogen, an increase in the primordial helium abundance will decrease the number of electrons in the primordial plasma at decoupling, increasing the photon mean free path and enhancing Silk Damping [48].

ACTPol's sensitivity at higher l also enables precision measurements of the secondary CMB anisotropies due to interaction of the CMB photons with large-scale

structure by gravitational lensing and the SZ and kSZ effects. Through these measurements, we can probe the growth of structure, putting constraints on early dark energy and the sum of the neutrino masses. For example, using the gravitational lensing signal and the primordial CMB temperature anisotropy spectrum from MBAC, the ACT team was able to detect dark energy from ACT CMB data alone [81]. Many clusters were also discovered by the ACT team through the SZ effect [62] [41].

Due to the location of ACT, we can cross correlate the CMB lensing, SZ, and kSZ findings with optical surveys such as SDSS BOSS [7]. Combining our data with other experiments increases the statistical significance of the findings of each experiment alone. Another advantage of ACT overlap with large optical surveys is that those surveys can provide estimates of redshifts and masses of clusters detected by ACT from their SZ signal. These data are vital for using the clusters for cosmology.

Chapter 2

ACTPol detector arrays and readout: Overview and assembly

To measure the very small anisotropies in CMB polarization and temperature, very sensitive detectors are needed. The ACTPol detectors are polarization-sensitive superconducting devices cooled to 80-120 mK by a dilution refrigerator. Light is coupled to each pixel by a feedhorn, then split into orthogonal polarizations and coupled to on-chip signal lines by an ortho-mode transducer (OMT). The microwave signal lines are routed to transition-edge sensor (TES) bolometers, where the optical power is measured. The development of this type of detector is described in detail in the following references: [94][64][15][47][65].

To limit the number of wires routed from room temperature to the cold stages and to amplify the TES signals, each detector array is read out with a time-division superconducting quantum interference device (SQUID) multiplexing system. In this chapter, we first give an introduction to the ACTPol detectors and readout. Then, we describe the electrical and mechanical assembly of the detector arrays with the readout.

2.1 Pixels

In the ACTPol detectors, TES bolometers are used to measure the CMB photon power. Because TES bolometers measure thermal power, it is necessary to somehow convert the CMB photon power into thermal power. This can be done by simply integrating a photon-absorbing material into the TES bolometer, as in the case of MBAC. In the case of ACTPol, to provide polarization sensitivity, the CMB signal is coupled through feedhorns to ortho-mode transducers (OMTs) that transmit two orthogonal polarizations to separate niobium transmission lines. Each signal travels to a TES bolometer, where it is terminated in a lossy gold resistor and deposited as heat. (see Fig. 2.1)

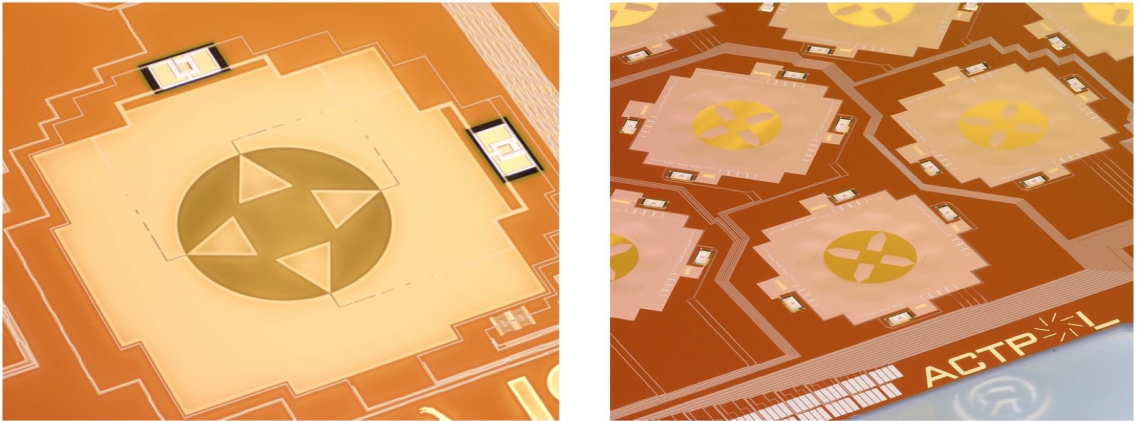


Figure 2.1: *Left:* PA2 pixel. The OMT consists of four triangle-shaped fins suspended on a silicon nitride membrane. OMT fins across from one another form a pair that couples the component of the light signal with polarization pointing parallel to the fins. The microwave signal is transmitted from the OMT fins to coplanar waveguide (CPW) signal lines, which transition to microstrip (MS) transmission lines that travel to the TES island. On the TES island, the MS lines transition to lossy gold resistors, where the microwave signal is transformed into heat. *Right:* PA3 pixels are the same as PA2 pixels except each pixel detects radiation in two frequency bands, defined by on-chip filters. Each polarization and frequency band is measured by its own TES, so there are four TESes per pixel.

In addition to providing polarization-sensitivity, the coupling of the photon signal to signal lines by the OMT also allows for on-chip frequency filtering of the signal.

The PA3 pixels measure radiation in both 90 GHz and 150 GHz bands. As shown in Fig. 2.1, the PA3 pixels have four TESes each, one for each polarization and frequency band. After the signal is split into two polarizations by the OMT, it is split into a 90 GHz band component and a 150 GHz band component by on-chip filters, and each band is measured by its own TES [65] [26].

Note that we do not use the on-chip filters for the PA1 and PA2 pixels, which only detect one frequency (150 GHz), because they introduce about 20% loss. We instead define the frequency band by the waveguide section of the feedhorns and low-pass filters in the optics tube. Including the loss introduced by the on-chip filters, the PA3 dichroic pixels should still be over 30% more sensitive than pixels detecting only 90 GHz [26].

2.2 TES Bolometers

One could imagine building a bolometer to measure thermal power as shown on the left side of Fig. 2.2. The thermal power we are trying to measure is deposited on an “island” that is only weakly thermally connected to a constant-temperature thermal reservoir (the bath). There is a sensitive thermometer on the island to measure its temperature. When the system is in thermal equilibrium, the thermal power deposited on the island is equal to the power conducted away from the island to the bath:

$$P_{on} = P_{off} = \int_{T_{bath}}^{T_{island}} G(T)dT, \quad (2.1)$$

where G is the thermal conductivity between the island and the bath. If we first calibrate the detector by measuring G , we can calculate the thermal power incident on the island from the island thermometer reading.

When the thermal power on the island changes, the TES island temperature will take some time to respond. For ACTPol, the time constant of the bolometer is

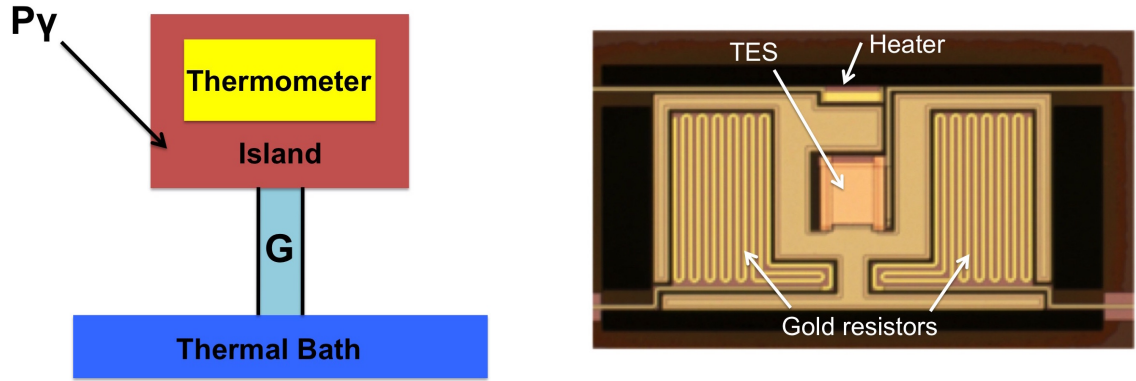


Figure 2.2: *Left:* Toy model of the ACTPol bolometer, used to measure thermal power. An island weakly thermally connected to a thermal bath absorbs the thermal power to be measured. When the system is in thermal equilibrium, we can calculate the thermal power on the island by measuring the temperature of the island. *Right:* Microscope image of a PA1 TES island. Four silicon nitride legs weakly thermally couple the TES island to the rest of the detector wafer. Microstrip lines carrying the photon signal are carried onto the TES island on the two bottom legs, then their signal is deposited as heat onto the TES island in the lossy gold resistors. The TES bias lines come onto the TES island on top of the upper right leg, and the heater bias lines enter via the upper left leg. The TES bias current runs vertically in this image. The two rectangles on the left and right of the TES are the copper banks used to suppress edge effects. Most of the TES island is covered by PdAu to increase its heat capacity.

important because we would like it to keep up with the telescope scan speed. In this toy model, if the photon power changes, the island temperature will exponentially decay from the initial temperature to the final temperature with a characteristic time constant given by the ratio of the island heat capacity, C , to the thermal conductivity, G .

In Fig. 2.2, a microscope image of an actual ACTPol bolometer is shown. The island is a thin silicon nitride membrane, fabricated on a silicon wafer. At the end of the fabrication process, the silicon is etched from the backside so that the island is only weakly thermally connected to the bulk of the silicon wafer, which acts as the thermal bath, by four narrow silicon nitride membrane legs [51]. There is a small heater on the island used during detector testing to provide a thermal test signal.

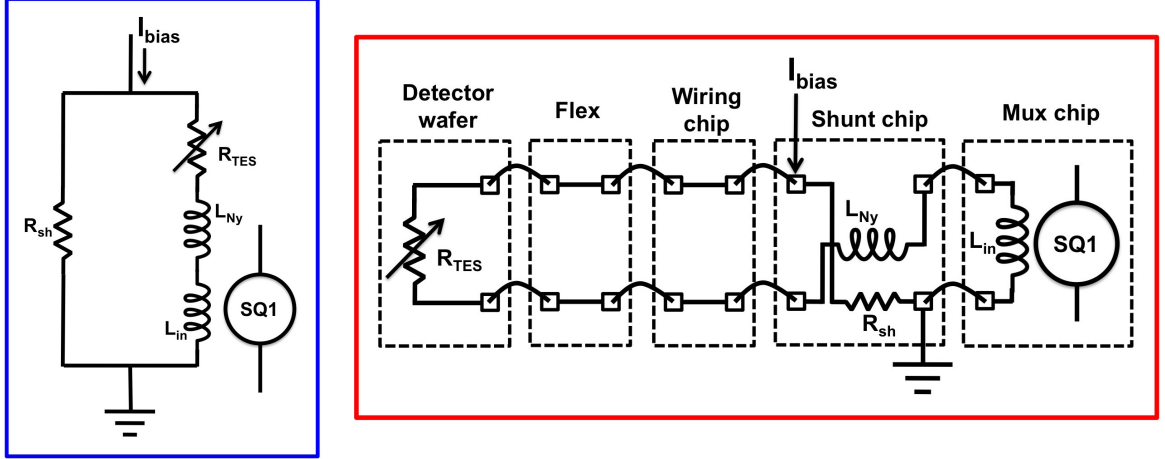


Figure 2.3: *Left*: TES bias circuit diagram. By current-biasing the TES in parallel with a small shunt resistor, the TES is effectively voltage-biased. The Nyquist inductor in series with the TES filters out high-frequency noise. The SQ1 input inductor, also in series with the TES, couples the TES current to the SQ1. *Right*: TES bias circuit diagram, showing on which chips TES bias circuit elements are housed.

The thermal conductivity of the ACTPol bolometer legs follows a power law, such that:

$$P_{off} = \kappa(T_{TES}^n - T_{bath}^n). \quad (2.2)$$

To make high signal to noise (S/N) measurements of the island temperature, we use TESes. A TES is a superconducting thin film used as a highly sensitive resistive thermometer. It is operated in the transition region between the normal and superconducting states, where there is a sharp transition from zero to non-zero resistance as a function of temperature.¹ The ACTPol TESes are Mo/Cu bilayer films with a T_c of about 150 mK.

During CMB observations, the TES is effectively voltage-biased onto its transition by applying a bias current to the TES in parallel with a shunt resistor, r_{sh} as shown

¹Although it would be nice if the TES resistance only depended on temperature, it is also a function of the bias current through the TES and magnetic field. The TES transition is discussed in detail in Chapter 5.

in Fig. 2.3. The power on the TES island is the sum of the electrical heating from the bias voltage, P_{bias} , and the microwave loading, P_γ :

$$P_\gamma + P_{bias} = \kappa(T_{TES}^n - T_{bath}^n). \quad (2.3)$$

Voltage biasing, as opposed to current biasing, the TES, provides negative electrothermal feedback that helps keep the TES state within the transition region as the signal power on the TES fluctuates. The electrical power in a voltage-biased configuration is $P_{bias} = V^2/R$, which decreases as the TES temperature and resistance increase. In contrast, in a current-biased configuration, the electrical power is $P_{bias} = I^2R$, which increases as the TES temperature and resistance increase. This can lead to thermal runaway and drive the TES out of the transition region.

The negative electrothermal feedback also decreases the TES bolometer time constant and suppresses the effect of the $R(T, I)$ transition shape on the bolometer response, as will be discussed more in Chapter 5.

2.3 Detector array readout: SQUID time-domain multiplexing

The large number of TESes in the ACTPol arrays and their high packing density both present readout challenges. With over 1,000 TESes in each of the three ACTPol arrays, reading out detectors individually would require routing over 6,000 wires from room temperature to the coldest stage of the dilution refrigerator. Attempting to route 6,000 wires through our cryostat would quickly become cumbersome and expensive. More importantly, it would also overload our cooling system.

To make the number of wires from room temperature manageable, each ACTPol detector array is multiplexed as a 32 column by 32 row array using SQUID time-

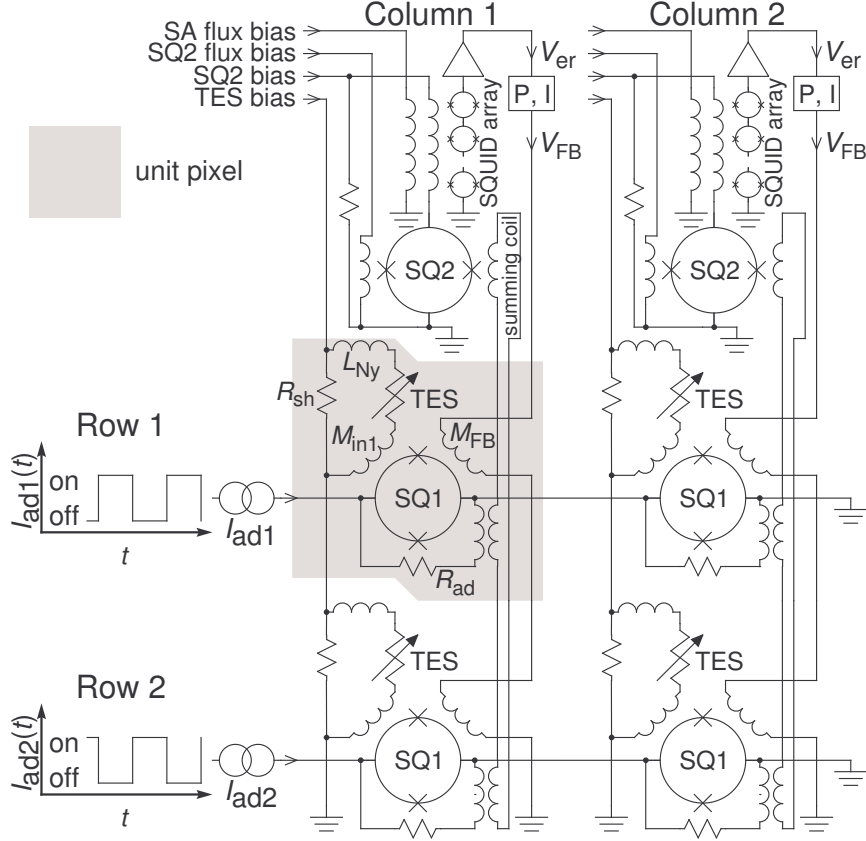


Figure 2.4: ACTPol TDM readout architecture. Here, the P,I box indicates the MCE, which processes the signal from the series array and applies the V_{fb} signal to the SQ1 necessary to keep it at its lock point. Figure courtesy Randy Doriese.

division multiplexing (TDM) [19] [49]. This reduces the number of wires per array entering the cryostat from room temperature from over 2,000 to 500.² The SQUIDs also amplify the small TES current signals.

We use three stages of DC SQUIDS for multiplexing and amplification, as shown in Fig. 2.4. The DC SQUID is a highly sensitive sensor of magnetic fields. As shown in the Fig. 2.5, when it is biased with a constant current, the voltage across the DC SQUID is a periodic function of the magnetic flux through the SQUID, with a period of one flux quantum ($\Phi_o = h/(2e)$). (For an introduction to DC SQUIDS, see M.

²We route five 100-pin cables and therefore 500 wires from room temperature to the 1K stage, but only 444 wires are used.

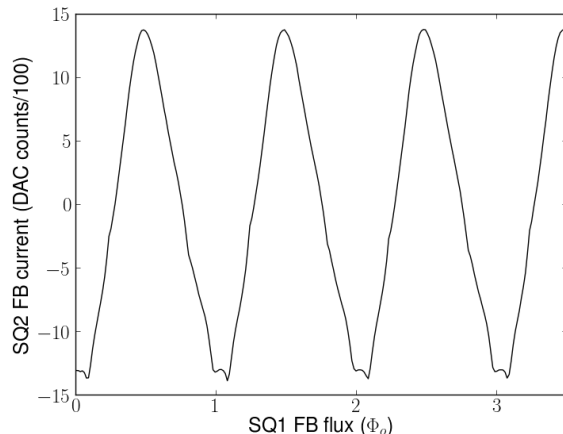


Figure 2.5: A SQ1 V- ϕ curve. To take this data set, the SQ2 FB current was varied to keep its voltage constant as the SQ1 FB current was swept at a constant rate. Here, the SQ2 FB current, which is proportional to the SQ1 voltage, is plotted vs. the magnetic flux applied to the SQ1. The SQ1 voltage is a periodic function of the flux coupled to the SQ1, with a period of Φ_o .

Tinkham 2012 [88].) In the ACTPol readout, we use DC SQUIDS as amplifiers of current signals by transforming them into magnetic flux with inductors.

Each TES signal is coupled to its own first-stage SQUID, which we call the SQ1, by an inductor in series with the TES. As shown in Fig. 2.3, there is also a Nyquist inductor in series with the TES to filter out high-frequency noise. The SQ1 signals in a column are all summed by a transformer loop and coupled into one second-stage SQUID, which we call the SQ2. The first and second stage SQUIDS are housed on Mux11c model multiplexing (mux) chips fabricated at NIST. The SQ2 signal is sent to the third stage of SQUIDS, an array of SQUIDS we call the series array or SA (also fabricated at NIST), that amplifies the signal before it is sent to the room temperature multi-channel readout electronics (MCE) [11].

The SQ1s in each row are biased in series by one bias line that we call either the row select or SQ1 bias line. Each row is switched on one at a time so that each column's SQ2 only receives a signal from one TES at a time. We cycle through the rows at as high a rate as possible to minimize multiplexing of higher frequency noise

into our band. This rate is limited by the settling time of the SQ2, which is about $2\mu\text{s}$ for ACTPol, so our cycle rate is about 15 kHz.

To linearize the response of the SQ1 to the TES current, the SQ1 is operated in a locked feedback loop at a linear section of the SQ1 curve. As shown in Fig. 2.4, there are two coils coupled to each SQ1, the input coil, in series with the TES, and the feedback (FB) coil. The current through the FB coil is varied as the TES current changes to keep the SQ1 voltage constant. By operating the SQ1 in a locked feedback loop, we are also able to calculate changes in the TES current without knowing the $V\text{-}\Phi$ functions of the SQUIDS. We only need to know the change in feedback flux applied to the SQ1, and multiply by -1 to find the change in flux through the TES input coil.

Because only one SQ1 on a column is read out at a time, all SQ1 FB coils on one column are biased in series by one line, further reducing the number of wires. The SQ2 and SA SQUIDS each have their own feedback line. We apply a constant feedback value to these SQUIDS so that they operate within linear portions of their $V\text{-}\phi$ curve. They remain within a good region of the curve during data acquisition because of the feedback loop on the SQ1.

To further reduce the number of wires routed from room temperature, multiple TES circuits are biased in series on one bias line. For PA1 and PA2, we have 15 TES bias lines. PA3 has 30 TES bias lines because TESes measuring 150 GHz and 90 GHz experience different loading conditions and so need to be biased on separate bias lines. We require that all wiring in the individual TES bias circuit shown in Fig. 2.3 be superconducting to avoid differences in stray resistance amongst TESes circuits on one bias line.

2.3.1 Measuring TES I, V, and R with the ACTPol readout

In this section, we discuss the procedures for calculating the TES voltage, current, and resistance with our readout system. This will be important in later sections, especially in Chapter 5, when the detector operation and calibration are discussed.

We would like to measure the TES current from the SQ1 FB current. When the SQ1 is at its lock point, the magnitude of the magnetic flux from the FB coil is equal to the magnitude of the magnetic flux from the TES input coil, modulo 2π :

$$I_{fb} * M_{fb} = I_{TES} * M_{TES}, \text{ mod } \Phi_o. \quad (2.4)$$

The mutual inductance between the FB coil and the SQ1, M_{fb} , and the mutual inductance between the TES input coil and the SQ1, M_{TES} , are in general not equal. We refer to the ratio of the former and latter mutual inductances as M_{rat} :

$$M_{rat} = M_{TES}/M_{fb}. \quad (2.5)$$

The M_{rat} value can be accurately measured, as described in the section below. However, because of the periodic relation between flux on the SQ1 and its measured voltage, measuring I_{fb} alone only constrains I_{TES} modulo one flux quantum:

$$I_{TES} = I_{fb}/M_{rat}, \text{ mod } \frac{\Phi_o}{M_{TES}}. \quad (2.6)$$

We can calculate the offset, δI_{fb} we need to add to I_{fb} to calculate I_{TES} , usually by taking an IV curve, and we have:

$$I_{TES} = (I_{fb} + \delta I_{fb})/M_{rat} \quad (2.7)$$

The TES voltage, V_{TES} , is almost constant at constant I_{bias} (the TES is effectively voltage-biased), but depends slightly on the TES current:

$$V_{TES} = r_{sh} * (I_{bias} - I_{TES}), \quad (2.8)$$

where during CMB observations I_{bias} is typically about $500 \mu A$, and I_{TES} is typically about $30\text{-}40 \mu A$.

Thus, R_{TES} is given by:

$$R_{TES} = r_{sh} * \left(\frac{M_{rat} I_{bias}}{I_{fb} + \delta I_{fb}} - 1 \right). \quad (2.9)$$

In practice, the MCE applies the voltages V_{fb} and V_{bias} , and I_{fb} and I_{bias} are calculated by measuring the resistance of the cables and any resistors in the MCE backplane. (The SQUID and TES resistances are very small compared to the cable resistance and MCE resistors, which add up to a few $k\Omega$, so they can be neglected in the calculation.) If R_{bias} is the resistance of the TES bias line, R_{fb} is the resistance of the feedback line, and δV_{fb} is the V_{fb} offset analogous to δI_{fb} , we have in summary:

$$I_{TES} = \frac{V_{fb} + \delta V_{fb}}{R_{fb} M_{rat}} \quad (2.10)$$

$$V_{TES} = r_{sh} \left(\frac{V_b}{R_b} - \frac{V_{fb} + \delta V_{fb}}{R_{fb} M_{rat}} \right) \quad (2.11)$$

$$R_{TES} = r_{sh} \left(\frac{V_b R_{fb} M_{rat}}{R_b (V_{fb} + \delta V_{fb})} - 1 \right) \quad (2.12)$$

$$P_{TES} = r_{sh} \left(\frac{V_b (V_{fb} + \delta V_{fb})}{R_b M_{rat} R_{fb}} - \left(\frac{V_{fb} + \delta V_{fb}}{M_{rat} R_{fb}} \right)^2 \right). \quad (2.13)$$

IV Curves

In this thesis, we will often talk about taking detectors' IV curves. We use IV curves to measure detector properties, as will be discussed in chapters 4 and 5. Currently,

we take an IV curve about once every hour during CMB observations to determine the optimal V_{bias} that should be applied to bias the TESes onto their transitions. A typical detector IV curve is shown in Fig. 2.6. At high voltage the TES is normal and has a constant resistance, R_n . As the voltage is decreased, the TES transitions to its superconducting state, where its resistance is zero.

To measure a detector’s IV curve, the I_{TES} vs. V_{TES} function, with our bias and readout configuration, we sweep V_{bias} and measure V_{fb} . As discussed above, the SQ1 FB flux is only defined modulo one flux quantum. During an IV curve, a SQ1 FB flux between $-\Phi_o/2$ and $+\Phi_o/2$ is applied. As the TES current either increases or decreases and the feedback flux jumps from say $+\Phi_o/2$ to $-\Phi_o/2$, this “flux jump” event is recorded by the software. At the end, the IV curve is stitched back together by adding in the recorded flux jumps. After the flux jumps are added into the data, there is still an overall V_{fb} offset, δV_{fb} , that needs to be calculated to determine the actual TES current.

To calculate δV_{fb} , we can fit a line to the part of the V_{fb} vs. V_{bias} curve where the TES is normal, as shown in Fig. 2.6. Because the resistance of the normal branch is (roughly) constant, its y -intercept should be zero. The V_{fb} offset is therefore the negative of the normal branch y -intercept. After δV_{fb} is calculated, we can convert the V_{fb} vs. V_{bias} curve to an I_{TES} vs. V_{TES} curve using the equations in the section above.

We can also convert the I_{TES} vs. V_{TES} data into other useful quantities. For example, in Fig. 2.6, a $\%R_n$ vs. V_{bias} curve is shown, which we use to determine which V_{bias} value should be applied to optimally bias the detectors during CMB observations. Usually we want to apply a V_{bias} value such that the detectors are biased near the center of the transition, at $50\%R_n$. Because there are 32-96 TESes on one bias line, it may not be possible to bias all detectors onto their transitions with one V_{bias} value if the detector properties are not uniform enough.

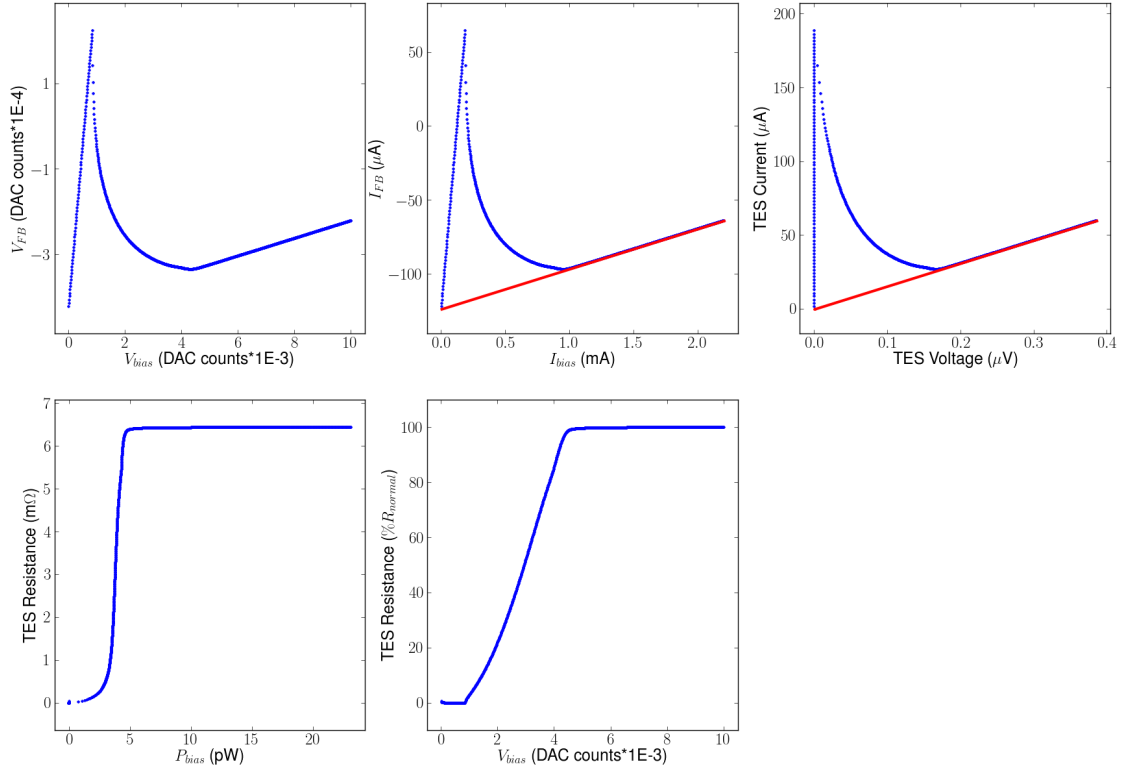


Figure 2.6: IV curve example. To take the data, V_{bias} is swept from high to low and V_{FB} is measured. In the five plots shown here, this data is converted into different units. *Upper left:* The V_{FB} in DAC units is plotted vs. V_{bias} in DAC units. *Upper middle:* The V_{FB} is again plotted vs. V_{bias} , but the units are converted from DAC counts to volts. To calculate the V_{FB} offset, a line is fit to the normal branch. *Upper right:* The offset is applied and the data is converted to units of TES voltage vs. TES current. This data can be converted to different useful quantities. For example, in the *Bottom left* plot, the TES resistance is plotted vs. the P_{bias} applied to the TES. In the *Bottom middle* plot, the $\%R_n$ at each bias voltage, in raw DAC units, is shown. This data is used to determine which V_{bias} value should be applied to optimally bias all TESes on a bias line onto their transitions.

The δV_{fb} value we calculate from the IV curve also needs to be added to the measured V_{fb} during observations to calculate I_{TES} . Because we will be interested in changes in photon power as we scan across the sky, it may seem like an offset on I_{TES} would not matter. However, as we will see in Chapter 5, measuring δV_{fb} , or equivalently, R_{TES} , is necessary to measure changes in photon power accurately. (To first order, this is because the TES is “effectively” voltage-biased but not exactly

voltage-biased. So at constant V_{bias} the TES voltage is not constant, but depends slightly on the TES current, or equivalently the TES resistance.)

Mux11c M_{rat} measurements

We measure M_{rat} by measuring the slope of the superconducting branch of the TES IV curve. When the TES resistance is zero, $I_{TES} = I_{bias}$ and the slope of the IV curve in raw units of V_{fb} vs. V_b is given by:

$$\frac{dV_{fb}}{dV_b} = \frac{R_{fb}M_{rat}}{R_b}, \quad (2.14)$$

so we can solve for M_{rat} by measuring this slope:

$$M_{rat} = \frac{R_b}{R_{fb}} \frac{dV_{fb}}{dV_b}. \quad (2.15)$$

Histograms of the measured M_{rat} values for the three ACTPol arrays are shown in Fig. 2.7. The median values for the PA1, PA2, and PA3 arrays are 8.81, 8.85, and 8.80, respectively. These agree within 1%, indicating that we have accurately measured the cable resistances for each array. (The cable resistances can vary depending on how much length is thermally coupled to colder stages, at which point the niobium-titanium (NbTi) cables will be superconducting, vs. warmer stages, at which the cables will be normal.)

If there were stray resistance, R_{stray} , in an individual TES bias circuit, we would measure a non-zero resistance when the TES is in its superconducting state. Instead of expression 2.15 above, the slope of the V_{fb} vs. V_b curve when the TES is superconducting would be:

$$\frac{dV_{fb}}{dV_b} = \frac{r_{sh}}{R_{stray} + r_{sh}} \frac{M_{rat}R_{fb}}{R_b}. \quad (2.16)$$

If R_{stray} is non-zero, the estimated M_{rat} will be smaller than the actual value:

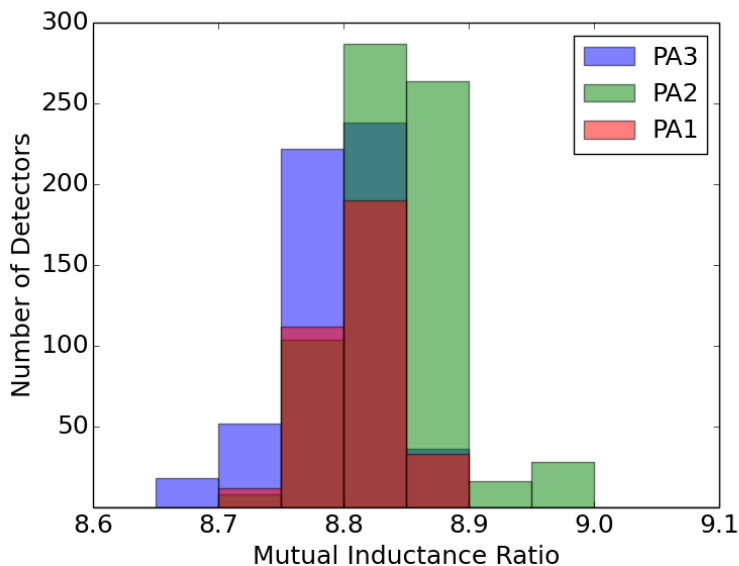


Figure 2.7: Histograms of the measured mutual inductance for each detector in ACT-Pol. The median value over all three arrays is 8.82, and the standard deviation is 0.04.

$$M_{rat,measured} = M_{rat,actual} * \frac{r_{sh}}{R_{stray} + r_{sh}}. \quad (2.17)$$

The smallest M_{rat} measured over the three arrays is 8.65, and the largest is 8.9. This could be accounted for by a difference in stray resistance between the two detectors of about 3% the shunt resistance, $R_{sh} = 180\mu\Omega$. This indicates the spread in stray resistance values over all detectors is less than $6\mu\Omega$.

2.4 ACTPol detector array assembly

2.4.1 Detector arrays and readout: physical design

The ACTPol detectors are fabricated on 76 mm diameter silicon wafers. As shown in Fig. 2.8, each detector array consists of three “hex” wafers, each fabricated on their own 76 mm wafer and etched into a hexagonal shape at the end of the process,

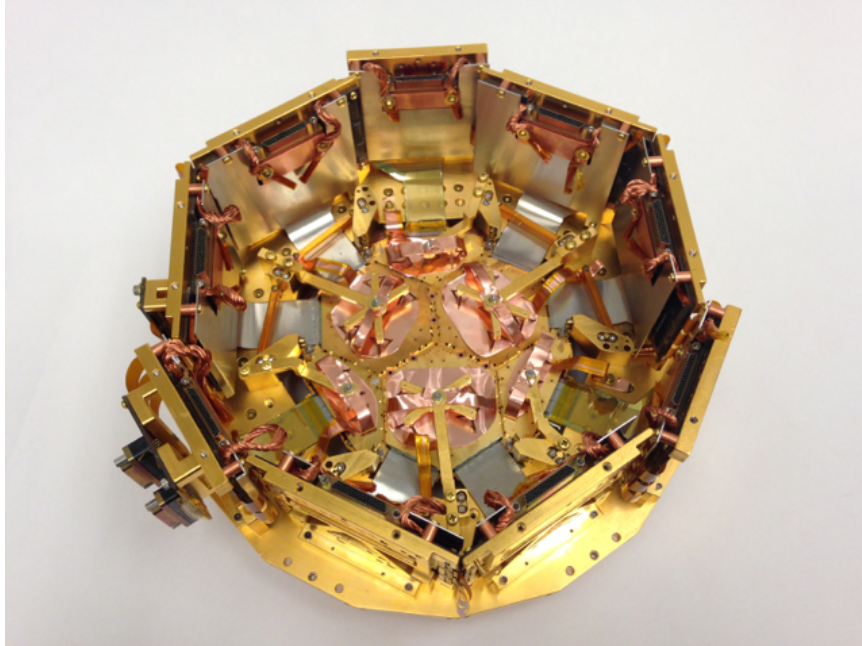


Figure 2.8: The ACTPol PA3 array. This view is from the backside of the detector wafers (light enters the bottom of the array as pictured here). The feedhorns, not visible here, support the detector wafers. The detector wafers are secured to the feedhorns with gold-plated copper clamps to provide heat sinking and hold the detector wafers in place when the feedhorns are pointed towards the sky. The MC PCBs surround the detector array. They are covered by aluminum panels that act as superconducting shields against magnetic fields for the mux chips. Figure courtesy Ben Schmitt.

and three “semihex” wafers, fabricated as a pair on one 76 mm wafer. The detector wafers sit on top of a gold-plated, monolithically fabricated 150 mm silicon array of corrugated feedhorns [16]. The feedhorns are made of a stack of 150 mm diameter silicon wafers, each etched with differently sized holes. When the silicon wafers are stacked together, the holes form a cone shape.

The first and second stage readout components reside on PCBs surrounding the detector array, heat sunk to the mixing chamber (MC) stage along with the detectors. We will call these the MC PCBs. The series array SQUIDs are housed in modules attached to PCBs at the still stage (1K). Niobium-titanium (NbTi) superconducting

cables with MDM connectors connect the MC PCBs to the SA PCBs and the SA PCBs to the MCE.

We use PCBs as the base for the MC readout assembly because we can both solder and wire bond components to them and they are mechanically robust: they won't break during handling or plugging and unplugging of cables. The material used for PCB substrates, FR4, also has a thermal contraction similar to OFHC copper, which we use for the array package hardware to which the PCBs are attached because of its high thermal conductivity at low temperatures.

As described above, each TES requires its own first-stage readout circuit, and the wiring connecting the circuit components must be superconducting. One drawback of current mainstream PCB technology is that high-density superconducting wiring is not available. The wiring in the PCBs we use is all copper and is only used for the multiplexing lines. All the individual TES readout circuit wiring on the MC PCB assemblies is on the silicon chips glued to the PCB, and superconducting aluminum wire bond interconnects.

To connect each TES to its first-stage readout circuit on the MC PCB, we use flex with superconducting aluminum traces. (See Chapter 3 for more details on the flex.) In addition to enabling the PCBs to be folded perpendicular to the detector array, saving focal plane area for detectors, the flex also allows for differential thermal contraction between the copper ring to which the MC PCBs attach and the silicon detector wafers.

As shown in Fig. 2.10, each column in the array has a wiring chip, shunt chip, and multiplexing (mux) chip. The wiring chips house niobium superconducting wires with 90 degree turns that connect the individual TES bias lines from the flex to the shunt chips. The SQ1s and SQ2s reside on the mux chips, and the shunt resistors and L/R filter inductor are on the shunt chip. The multiplexing lines for each column come in through the NbTi cable to the MC PCB. The TES bias lines are wire bonded

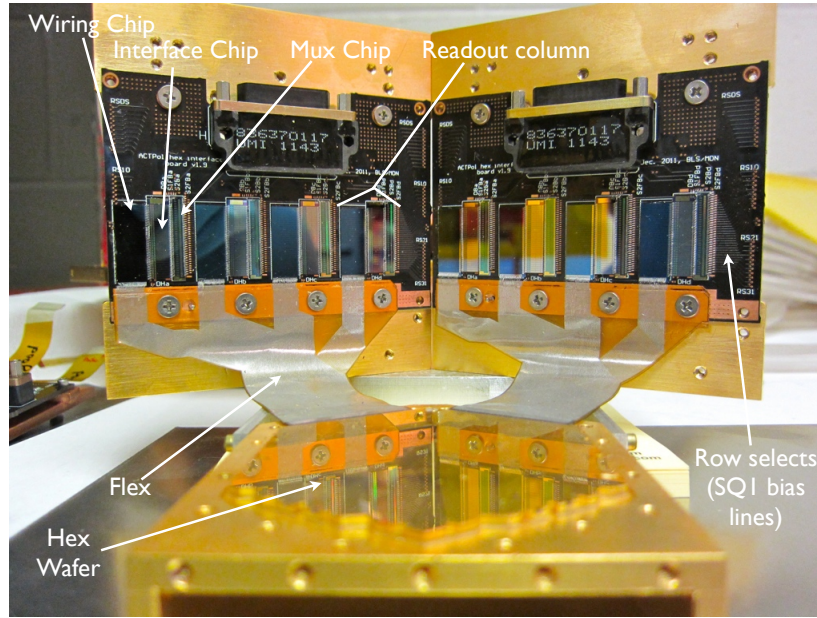


Figure 2.9: Assembled ACTPol hex wafer. There are two MC PCBs per hex wafer, folded perpendicular to the detector wafer. Each PCB has four readout columns, and there is a wiring chip, shunt chip, and mux chip on the PCB for each column. The detector wafer and MC PCBs are connected by TechEtch aluminum superconducting flexible cables with a wedge wire bonding interface. Figure courtesy Emily Grace.

from the MC PCB to the shunt chips (at the top in Fig. 2.10), and the SQ1 FB, SQ2 bias, and SQ2 FB lines are wire-bonded from the PCB to the the mux chips (also at the top in Fig. 2.10). The row select lines run across the MC PCB. For each row, the SQ1 bias lines are wire bonded from the mux chip to the PCB row selects in series. Row select lines are connected between MC PCBs with copper flexible cables (flex) that attach to the MC PCBs with zero insertion force (ZIF) connectors.

The ACTPol detector wafers, readout chips, and series array modules described above were all fabricated at NIST. The mechanical mounting parts were designed at the University of Pennsylvania. The assembly of the detector wafers with the readout components was performed at Princeton University. The arrays were assembled one at a time, starting with PA1, then PA2, then PA3. The electrical yield of each array steadily improved as more advanced assembly procedures were developed.

The ACTPol detector wafers, readout chips, and series array modules described above were all fabricated at NIST. The mechanical mounting parts were designed at the University of Pennsylvania. The assembly of the detector wafers with the readout components was performed at Princeton University. The arrays were assembled one at a time, starting with PA1, then PA2, then PA3. The electrical yield of each array steadily improved as more advanced assembly procedures were developed.

2.4.2 Assembly process overview

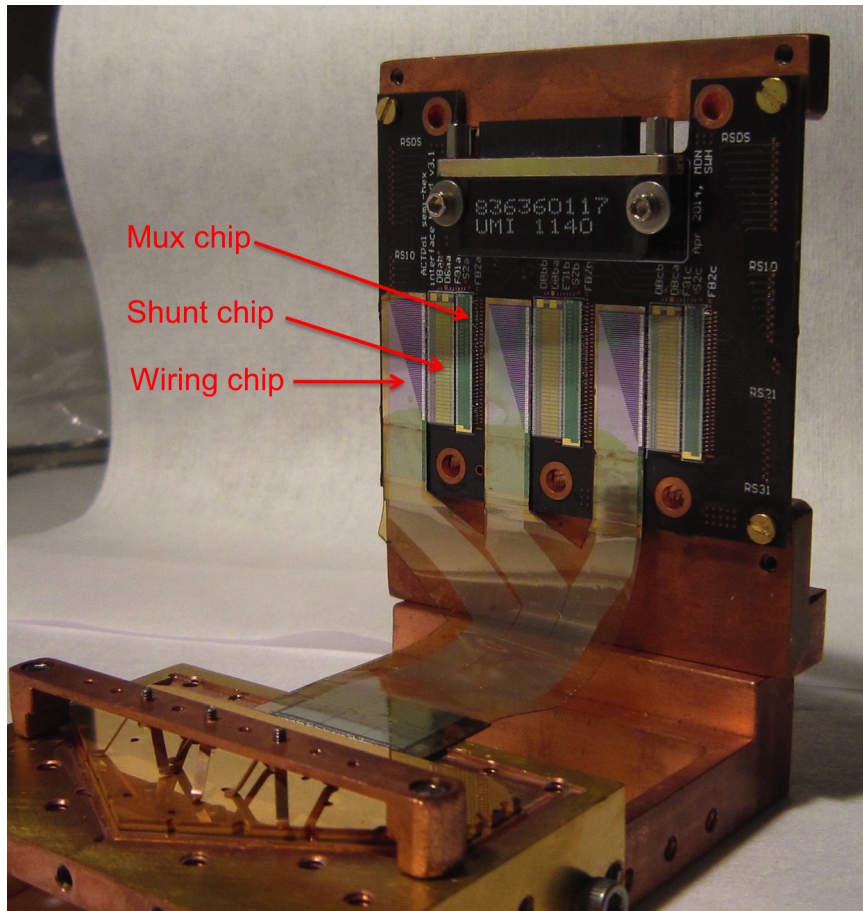


Figure 2.10: Assembled ACTPol semihex wafer on testing hardware. The semihex wafer assembly is identical to the hex assembly (Fig. 2.10), except that there is only one PCB per semihex with three readout columns. In the image above, flex fabricated at Princeton (see Chapter 3) is used for the assembly. In this flex, the wiring chips and the flex are monolithically fabricated as one piece.

All electrical connections to the readout chips, flex, and detector wafers were made with aluminum wedge wire bonding. We use rubber cement for die bonding (gluing) of the chips and flex because it provides a flexible bond that allows for differential thermal contraction between silicon and PCB. (If stronger adhesives such as Stycast are used to glue silicon components to FR4, the silicon chips may crack at low temperatures.) The rubber cement is also not permanent, so the chips and flex are semi-removable after gluing.

The first step of assembling a detector wafer with its mixing chamber-stage readout components is to assemble the MC PCBs. To start, we prep the MC PCB: we have the connectors professionally soldered onto the board, we scrub the PCB bond pads with an eraser or Scotch-BriteTM to remove the copper oxide, and we clean the PCB with isopropanol. Next, we die bond the readout chips to the PCB with rubber cement adhesive. After a few hours, when the rubber cement is dry, we make the wire bonds between readout chips and between chips and the PCB. Then, an electrical check is performed from the PCB connectors to look for shorts between multiplexing lines and check for open multiplexing lines.

After the MC PCB is assembled, we glue the flex to the MC PCB and detector wafer using rubber cement. At this point, the detector assembly is in the “flat” assembly configuration: the detector wafer, flex, and MC PCB all lie in one plane. After the rubber cement dries, we wire bond between the flex and the wiring chips on the PCB side and between the flex and the detector wafer on the other side. We perform another electrical check on the multiplexing lines and inspect the assembly under the microscope to see if there are any wire bonds that need to be fixed, then fold the MC PCB perpendicular to the wafer.

After running individual cryogenic performance tests on the detector wafer, it is assembled onto the feedhorns using a vacuum chuck and XYZ micrometer stage (see E. Grace PhD thesis).

2.4.3 Wedge Wire bonding

We use a K&S 1470 wedge wire bonder with 25 μm thick aluminum wire to make all wire bonds for electrical connections. (Gold wire bonds are used in some places to improve thermal conductivity between components.) The K&S 1470 bonder is a programmable machine capable of fully automatic wire bonding. Wedge wire bonders use pressure perpendicular to the chip and ultrasonic vibrations parallel to the chip to weld the wire to a metal bond pad. In order for these forces to be exerted between the wire and the bond pad, the chip must be well mechanically secured. It is also important for the bond pads to be clean to form strong wire bonds. Residue on the bond pads can inhibit the welding process or cause it to fail completely.

2.4.4 Assembly with Tech-Etch flex

Traditional, commercially available superconducting flex from Tech-Etch was used for the first and second ACTPol arrays and the hex wafers in the third ACTPol array.³ The process used to make this flex is similar to that used for PCB manufacture. First, a freestanding aluminum foil layer is manufactured. It is then glued to a Kapton[®] substrate with an adhesive layer and wet etched into traces.

The pitch of the Tech-Etch flex was limited to 200 μm due to the large grain size of the aluminum foil used. In ACTPol, two interleaved, stacked layers of the flex were used to meet our 100- μm pitch requirement. The traces on the Tech-Etch flex were often over-etched, due to the large grain size of the aluminum foil and our tight 200- μm pitch requirement on a single layer. We found the flex pieces with over-etched traces were very difficult to wire bond. This seemed to be caused by tilting of the trace if the bond tool tip did not hit the trace exactly in the center, due to the large aspect ratio of the traces (which are 25 μm thick) and the softness of the Kapton substrate

³Tech-Etch, Inc., 45 Aldrin Road, Plymouth, MA 02360 USA

underneath them. It was important to screen the flex and use only the pieces with traces greater than 100 μm wide in the final assembly.

Because the Tech-Etch flex bond pads sit on a soft (Kapton[®] and adhesive layer) substrate, it is necessary to mount the flex to a hard substrate for wire bonding.⁴ For consistently robust wire bonds across the piece of flex, the flex should be well secured to the stiffener underneath all of the bond pads. For ACTPol, we glued the flex to copper or silicon stiffeners with Stycast 1266, then glued the stiffener to the PCB and the detector wafer with rubber cement during assembly, as described above.

The detectors in PA1 and most of PA2 were assembled with Tech-Etch flex that was glued to stiffeners by hand using an alignment jig. We had some problems using this method with Stycast coming up onto the traces so we couldn't bond to them, as well as residue on the bond pads from vacuum grease used during the process. The flex was also not well adhered to the stiffeners in some small areas, making wire bonding to these regions very difficult. This likely occurred due to uneven pressure and/or glue application during the gluing process.

Later, we developed an improved mounting process that we used for the FH6 hex in PA2 and all of the hex wafers in PA3. We used a flip chip bonder for this process to align the flex to the stiffener and apply even pressure. This process did not require vacuum grease and we were careful to apply only a very thin layer of Stycast, blotting off any excess. We used only silicon stiffeners, as the Stycast did not adhere well to the copper stiffeners used previously for the PCB side of the flex. The copper stiffeners were also flexible, leading to warping during gluing that made forcing the flex into contact with the stiffener along the entire length difficult.

The average yield (not counting open multiplexing lines) of detectors assembled with the advanced stiffener mounting method was 92%, 8% higher than the average

⁴It is also possible to purchase flex from Tech-Etch that is laminated onto stiffeners by the manufacturer.

yield (not counting open multiplexing lines) of detectors assembled with flex mounted by the original method, 84%.

2.4.5 Assembly with Princeton flex

The semihex detectors in PA3 were assembled using flex fabricated at Princeton University, described in Chapter 3. This flex does not have the assembly challenges of the Tech-Etch flex because the bond pads sit on a hard silicon substrate (uncoated with polyimide/Kapton[®]), making wire bonding to this flex as simple as wire bonding to ordinary chips. The average yield of the three PA3 semihex detectors assembled with the Princeton flex was 92% (not including open multiplexing lines).

2.4.6 Assembly yield

As our assembly methods improved, the yield of the ACTPol arrays steadily improved, from 59% for PA1, to 79% for PA2, to 86% for PA3. The main factors leading to these results were the bondability of the flex, discussed above, and the number of open multiplexing lines in each array.

The bulk of the large difference in yield between PA1 and the next two arrays was due to differences in the number of open multiplexing lines. There were four rows and six columns open in PA1, two columns open in PA2, and one column and one row open in PA3. When we look at the yield of detectors unaffected by open multiplexing lines, the numbers become more similar for the three arrays: 85% for PA1, 85% for PA2, and 92% for PA3.

The increase in the yield of detectors unaffected by open multiplexing lines from PA2 to PA3 is due to improvements in the bondability of the flex used, as discussed above. All of the flex in PA1 was mounted to stiffeners by the original method discussed above, and this array had an average yield of 85%. Most of the wafers in PA2 were assembled with Tech-Etch flex mounted by the old method and had an

average yield of 83%, similar to the PA1 result. One hex wafer in PA2 (FHB6) was assembled with Tech-Etch flex mounted by the new method and had a yield of 90%. The PA3 hex wafers were all assembled with Tech-Etch flex mounted by the new method and had an average yield of 92%. The PA3 semihex wafers were assembled with the flex fabricated at Princeton and also had an average yield of 92%.

Chapter 3

Flex fabrication for ACTPol and Advanced ACTPol

3.1 Introduction

Especially if multichroic pixels are used, CMB experiments can receive large scientific returns by increasing the number of detectors in the usable focal plane area [66] [36]. Due to cryogenic space constraints, large arrays of detectors need to be packed to high density, and high-density superconducting wiring is required to read them out. Although SQUID multiplexing reduces the number of wires at higher temperature stages, two superconducting wires must connect each TES to the first readout component (the SQ1 input coil in TDM or the resonator in frequency-domain multiplexing (FDM)) [49].

Connecting readout components to electrical contacts on the perimeter of the detector array, as in ACTPol, allows for a simple wire bonding assembly. Flexible circuitry (flex) is often used to connect the silicon-based detector arrays to the readout PCBs to accommodate differences in thermal contraction between the two materials.

The flex also allows the readout PCBs to be folded out of the focal plane, as in ACTPol, to save room in the focal plane for detectors.

For larger and/or higher density TES arrays, flex with superconducting wiring dense enough to match the wiring density at the perimeter of the detector array is not readily available commercially. A thick foil is used for the metallization layer in conventional PCB and flex manufacture, and the feature size of the wiring layer is limited by the large grain size of the foil. For example, the pitch of the aluminum flex from Tech-Etch used for ACTPol is limited to 200 μm or more. In recent years, researchers in the field have started developing fabrication processes capable of creating custom superconducting flexible circuitry with smaller feature sizes [9][91][75][76].

In this chapter, we discuss our fabrication process for high-density, superconducting flex for connecting large TES arrays to the first-stage readout. The flex was used in the ACTPol PA3 semihex assemblies and will be used in the AdvACT arrays. We have so far created flex with 100 μm trace pitch for ACTPol and 70 μm trace pitch for AdvACT. Because we use a thin sputtered metallization layer for the wiring and not a granular foil, the trace density can grow with array readout density requirements.

Another challenge of large TES arrays is the large-scale detector-readout assembly required. For example, the first AdvACT detector array, the high-frequency (HF) array, will require over 20,000 aluminum wire bonds and die bonding (gluing) of 300 chips and flex. For large assemblies like this, it is important to develop a foolproof assembly process to produce a robustly assembled array by the deadline.

As discussed in the previous chapter, wire bonding to pads on soft substrates is challenging. By increasing the bondability of flex in the ACTPol arrays through improved mechanical mounting of the Tech-Etch flex and replacing some of the Tech-Etch flex with the flex discussed in this chapter, we were able to increase the TES electrical yield by 8% [44]. The flex presented here features a robust wire-bonding

interface to bond pads that sit on a hard silicon (uncoated with polyimide) substrate, so wire bonding to these cables is as simple as wire bonding to ordinary chips.

3.2 Flex Design

3.2.1 Maximum Trace Density

In this section, we make a projection of the maximum trace density possible with our current fabrication process and testing results. We also discuss possible avenues for increasing this trace density if necessary. The flex trace density may be limited by lithography and etching capabilities, the superconducting critical current, and the necessary electrical contact size and spacing.

Lithography

With current laser-writing tools, it is possible to write masks for photolithography with $1\ \mu\text{m}$ feature size in a reasonable amount of time (about one hour per mask for a 4" wafer of flex, depending on mask complexity). As we will see, lithography capabilities will not limit the trace density, as this is higher resolution than we will need after other flex design constraints are taken into account.

Superconducting critical current

The flex traces are part of the individual TES bias circuits, connecting each TES to the shunt chip, so they must be superconducting with a critical current larger than the TES bias current. For ACTPol and AdvACT, we would like the flex traces to remain superconducting throughout the acquisition of an IV curve, as well as during CMB observations at a given TES bias current. The critical current density of a superconducting wire is determined by the superconducting properties of the wire

material, and the critical current generally scales with the cross-sectional area of the wire.

As will be discussed more in Sec. 3.4.1, we find that the critical current requirement for ACTPol and AdvACT is exceeded by at least a factor of two by flex with aluminum traces 400 nm thick and 20 μm wide at their narrowest point. The flex is currently successfully being used in the ACTPol PA3 semihex assemblies. It should be possible to decrease the trace width without running into critical current issues, especially if a thicker aluminum-wiring layer is used. For now, as a conservative estimate of the flex trace density that can be achieved, we will assume that a trace width of at least 20 μm is necessary to meet the critical current requirements of ACTPol and AdvACT-style TES bolometers.

We chose to use aluminum for the wiring layer because its nominal T_c of 1.2 K is well above our operating temperatures of 80-120 mK, it is a soft, flexible metal, so it should not be prone to cracking when used in flexible circuits, and it is easy to work with in fabrication. It can be easily etched in wet etchant, and unlike niobium, aluminum is not a “getter,” so the superconducting properties of aluminum films are not very sensitive to the cleanliness of the deposition chamber. However, if higher trace densities are desired and these obstacles can be overcome, niobium may be an attractive option as its T_c is much higher than aluminum, at 9.2 K, so narrower traces could be used. Niobium has been used in polyimide flexible cables successfully by other research groups (see, e.g., [91]).

Electrical contact size and spacing

Like the flex traces themselves, the electrical connections made to the flexible cables must be superconducting. The electrical connections also need to be placed at a high enough density to accommodate the trace density of the flex. The two best-

established options for making superconducting electrical connections between small pitch devices are indium bump bonding and aluminum wedge wire bonding [60].

For wedge wire bonding, the bond pad pitch is limited by the wire width and the tool tip width. The bond pads on the flex need to be at least as wide as the bond foot produced during bonding, about 1.5 times the width of the wire used. The bond pads also must be spaced at a pitch wide enough such that the tool tip does not hit adjacent bond feet. So, the pitch must be at least $(t + bf)/2$, where t is the width of the tool tip and bf is the width on the bond foot.

For ACTPol and Advanced ACTPol, we wire bond with a $90\ \mu\text{m}$ wide tool tip and $25\ \mu\text{m}$ thick aluminum wire. With these specs, we have shown that we can wire bond pads at an $80\ \mu\text{m}$ pitch (see Fig. 3.1). With $10\ \mu\text{m}$ wire, $40\ \mu\text{m}$ pitches have been demonstrated [60].

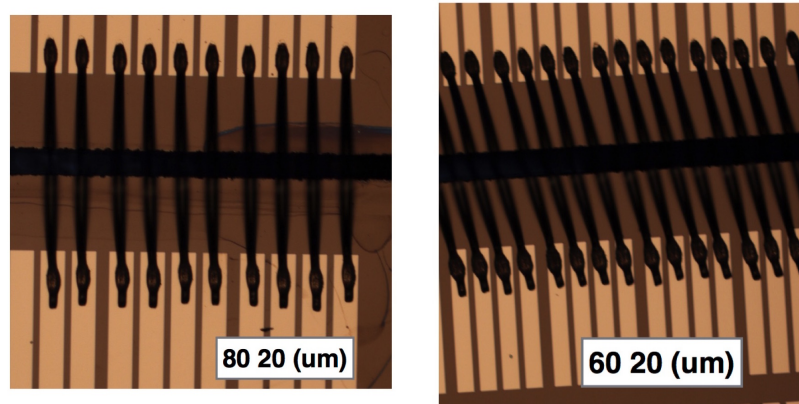


Figure 3.1: *Left:* Bond pads $80\ \mu\text{m}$ wide placed at a $100\ \mu\text{m}$ pitch, wire bonded with $25\ \mu\text{m}$ thick wire. *Right:* Bond pads $60\ \mu\text{m}$ wide placed at a $80\ \mu\text{m}$ pitch, wire bonded with $25\ \mu\text{m}$ thick wire. Figure courtesy Patty Ho.

The electrical contact size and pitch can be decreased if indium bump bonding is used instead of wire bonding. For indium bump bonding, thick indium “bumps” are first fabricated onto electrical contacts (as in Fig. 3.4) on the chips to be electrically connected. The bumps on the two chips are then aligned and pressed together with a flip chip bonder. Heat may also be applied to facilitate the bonding of the bumps,

but because indium is so soft, pressure alone is often enough to bond the bumps together. With the current flip chip technology, bumps can be aligned together with sub-micron accuracy. This allows the bump pad to be as small as 5-10 μm on both sides.

The fabrication of this flex is most straightforward if there is only one wiring layer. (However, flex with multiple wiring layers should certainly be possible with further process development.) To increase the trace density beyond the maximum bond pad density, multiple rows of offset bond pads may be used, as shown in Fig. 3.2. The smallest trace pitch achievable on flex with n rows of electrical contacts with equal electrical contact spacing in each row, a minimum allowable trace width of w , a minimum required spacing between all traces and bond pads of l , a minimum electrical contact width of b , and a minimum electrical contact pitch of p is:

$$pitch = \begin{cases} (b + w(n - 1) + ln)/n & \text{if } p > b + w(n - 1) + ln, \\ p/n & \text{if } p < b + w(n - 1) + ln. \end{cases} \quad (3.1)$$

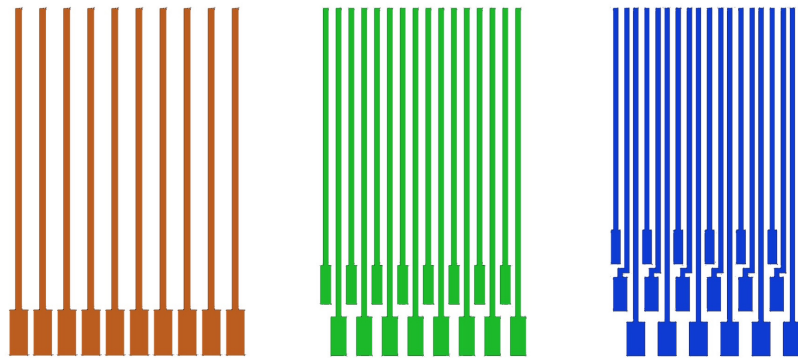


Figure 3.2: From left to right: Trace routing for one row, two rows, and three rows of bond pads

If only one row of bond pads is used, the pitch is equal to the sum of the bond pad width and the minimum bond pad spacing. Increasing the number of bond pad rows

allows for a tighter trace pitch, with the pitch approaching the sum of the minimum trace width and trace spacing as the number of bond pads rows approaches infinity.

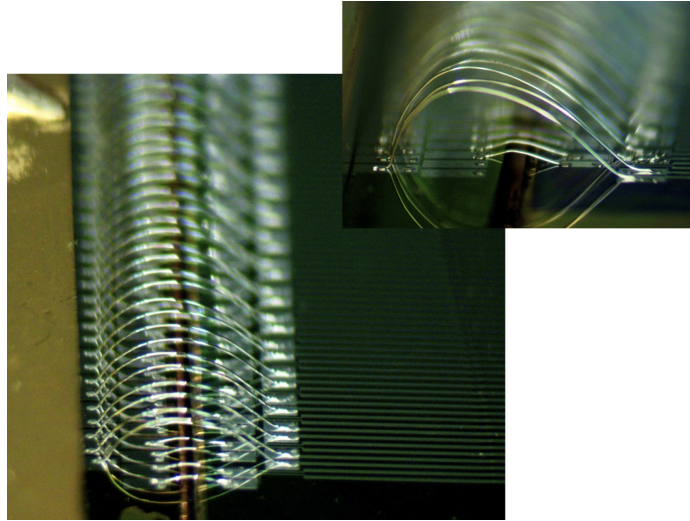


Figure 3.3: Wire bonds from an ACTPol detector wafer (on the left) to a piece of the flex discussed in this chapter. There are two layers of wire bonds: the low loop height wire bonds between the front rows of bond pads, and the high loop height wire bonds between the back rows of bond pads.

If a wire-bonding interface is used with this bond pad configuration, the outermost row is wire bonded to the outermost row of the mating chip first with a low loop height, then the next outermost row is bonded with a slightly larger loop height so that the bond wires do not short, and so on. We use two rows of bond pads in the ACTPol and AdvACT flex (see Fig. 3.3). The necessary loop height for the inner bond pad rows could become too high if three or four rows of bond pads were used. Increasing the height of the substrate under the inner rows of bond pads relative to the outer rows helps prevent shorts between bond wires so that very high loop heights are not necessary [60]. Steps could be created in flex with multiple rows using an isotropic silicon etch before the wiring layer is deposited. Indium bump bonding flex with any electrical contact layout is straightforward: the mirror image of the electrical contact configuration is simply fabricated on the mating chip.

Maximum trace density: Summary

We have shown (see Sec. 3.4.1) that we can provide the necessary I_c for ACTPol and AdvACT with a trace width of $20\ \mu m$. With our current wire bonding capabilities, the bond pad pitch can be as small as $80\ \mu m$ and the bond pad width can be as small as $40\ \mu m$. We assume $5\ \mu m$ separation between traces and bond pads. Using these numbers, the highest density flex we can currently achieve is shown in the table below. With two rows of bond pads, we should be able to create flex with a trace pitch as small as $40\ \mu m$.

Trace width	# bond pad rows	Bond pad width	Bond pad pitch	Trace pitch
$20\ \mu m$	1	$60\ \mu m$	$80\ \mu m$	$80\ \mu m$
$20\ \mu m$	2	$50\ \mu m$	$80\ \mu m$	$40\ \mu m$
$20\ \mu m$	3	$40\ \mu m$	$95\ \mu m$	$32\ \mu m$
$20\ \mu m$	4	$40\ \mu m$	$120\ \mu m$	$30\ \mu m$

Table 3.1: Projected maximum trace density

3.2.2 Flex Structure

We use aluminum wedge wire bonding to make electrical connections to the ACTPol and Advanced ACTPol flex. An aluminum wedge wire-bonding interface was the natural choice over indium bump bonding for the ACTPol and Advanced ACTPol detector wafers as this is how this type of detector wafer has always been made at NIST. Producing ACTPol-type detector wafers with indium bumps would require significant additional process development. In the future, if a tighter interface wiring pitch were needed than what is achievable with wire bonding, indium bump bonding would be an attractive option.

As discussed in the previous chapter, wire bonding to bond pads on a hard substrate such as silicon is straightforward and reliable, while wire bonding to bond pads on a soft substrate such as polyimide or polyimide-coated silicon has many potential

pitfalls. For the flex to have a hard substrate wire-bonding interface, the flex traces must somehow transition from the flexible polyimide substrate in the center of the flex to a hard silicon substrate at the ends.

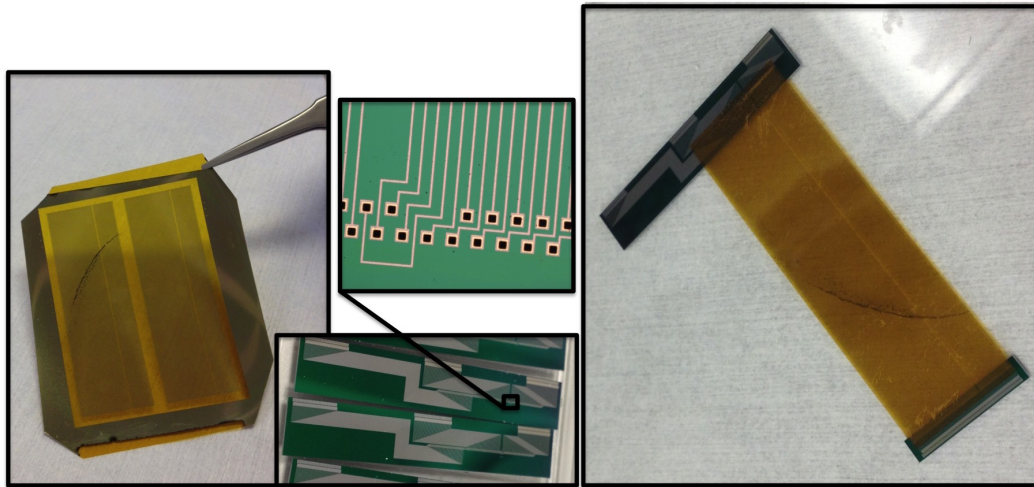


Figure 3.4: Indium bump bonded flex. *Left:* Aluminum traces, placed at a $100\text{-}\mu\text{m}$ pitch, fabricated on a pre-made electronic grade Kapton film. *Right:* The flex is bump bonded to hard silicon chips on either end. The electrical connections are made to the chips by wedge wire bonding. *Lower Middle:* Interface chips like the one bump bonded to the top side of the flex in the photo on the right. *Upper Middle:* Detail of bump bonding chip. Bump pads are $110\ \mu\text{m}$ wide squares with $50\ \mu\text{m}$ wide indium bumps about $10\ \mu\text{m}$ thick.

One method we explored for creating this transition, pictured in Figure 3.4, was to indium bump-bond a flexible cable to a hard silicon chip. An advantage of this method is that a pre-made electronic-grade polyimide substrate can be used for the flexible part of the cable, saving the time needed for fabricating a polyimide film from a precursor solution, as discussed in Sec. 3.3.2.

However, performing lithography on a freestanding polyimide film instead of a silicon wafer coated with a polyimide film is challenging. If the Kapton is not mounted completely flat each time, it is impossible to get the next lithography layer to line up with the previous one everywhere across the film. Fabricating the indium bumps and performing the bump bonding process is also a time-consuming process, taking

at least a full day. Additionally, the indium interface is another electrical connection, opening us up to an extra failure mode.

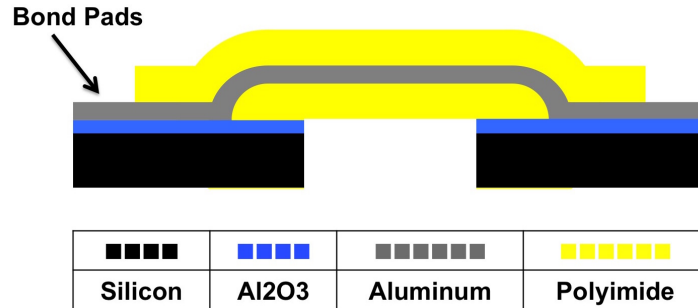


Figure 3.5: Diagram of flex from side view, not to scale. The traces are supported by a polyimide substrate in the middle of the cable, where it is flexible. At the ends of the cable, the substrate transitions to Al_2O_3 coated silicon for a robust wire-bonding interface. The wiring layer is 400 nm thick sputtered aluminum, and is covered everywhere but the bond pads by polyimide to protect the traces.

For this reasons, we have decided to instead accomplish the polyimide-to-silicon substrate transition by coating a silicon wafer with a patterned polyimide film. The cable structure is shown in Fig 3.5. We pattern the polyimide film with shallow-sloped sidewalls to ensure that they can be conformally coated by the sputtered aluminum-wiring layer. After fabricating the wiring layer, another polyimide layer is fabricated on top of the wiring layer to protect the traces. It is patterned to reveal only the bond pads. At the end of the fabrication process, the silicon is removed in the center of the cable, where we want it to be flexible.

The ACTPol flex and AdvACT flex fabricated by the process discussed in this chapter are shown in Figures 3.6 and 3.7, respectively. In the next section, we describe each element of the fabrication process in detail, starting with the procedures for patterning the polyimide layers.

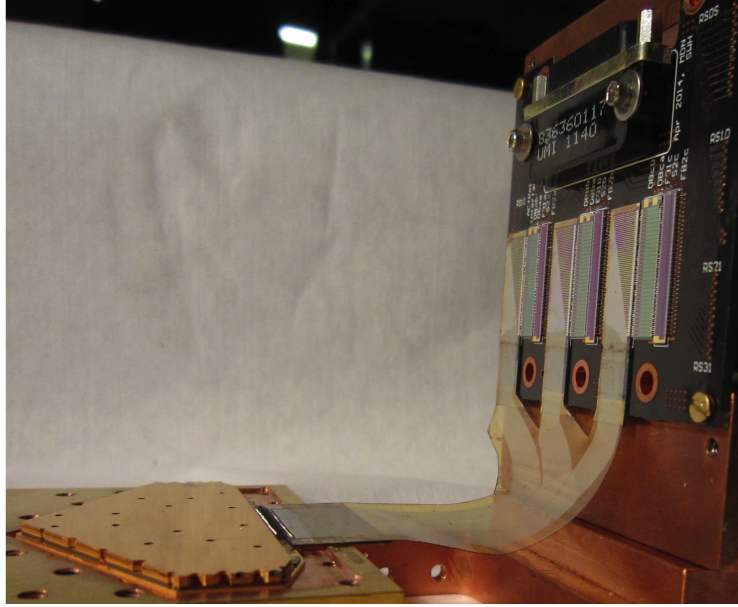


Figure 3.6: Flex fabricated by the process in this chapter was used to assemble the ACTPol PA3 semi-hexes, as shown here. The trace pitch is $100\ \mu\text{m}$ and the bond pad pitch is $200\ \mu\text{m}$. There are 64 traces in each of the three columns (192 traces in total). The wiring chips and flex are monolithically fabricated as one piece. After all other fabrication steps of the flex are completed, it is diced into the shape shown here with a yttrium aluminum garnet (YAG) laser dicer.

3.3 Flex fabrication process

In this section, we describe the flex fabrication process. First, the process development for each step is described. Then, an overview of the current best version of the process is given.

3.3.1 Silicon passivation layer

To accurately diagnose opens and shorts in the flex traces at room temperature, the silicon wafers need to be passivated with an insulating layer. We currently use an aluminum oxide (Al_2O_3) layer about 110 nm thick for this purpose because it doubles as an etch stop to protect the polyimide film during the backside silicon etch. We grow the Al_2O_3 layer by atomic layer deposition (ALD), which grows films one

atomic layer at a time. We use the Cambridge NanoTech Savannah 100 ALD tool in the MNFL cleanroom, with the recipe in Tables B.1-B.3, to grow 1000 monolayers of Al_2O_3 (about 110 nm).

3.3.2 Fabricating and patterning polyimide films

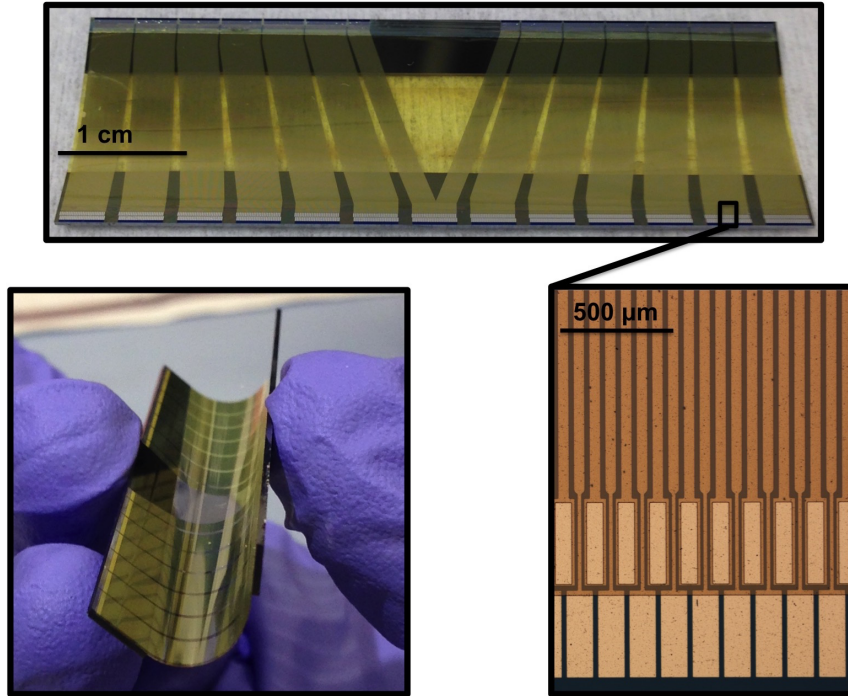


Figure 3.7: AdvACT HF array flex. *Top*: Photograph of a piece of HF flex. It is about 61 mm wide and 20 mm long and carries 676 traces. *Bottom Right*: Microscope image showing detail of HF flex traces and bond pads. The trace pitch is $70\ \mu\text{m}$ and the bond pad pitch is $140\ \mu\text{m}$.

Polyimide (brand name DupontTM Kapton) is a very strong and non-reactive flexible plastic. After the PI-2611 polyimide film is fully furnace-cured, it is resistant to most solvents, including 300 MIF photoresist developer, NMP-based photoresist removers, acetone, methanol, and isopropanol, and is only attacked by strong acids and bases. It does not melt, but will burn at very high temperatures, above about 500°C . The chemical and heat resistance of polyimide are necessary properties of the cable substrate as they allow it to withstand some harsh fabrication steps such as

etching of the wiring layer and the silicon. However, the chemical resistance and robustness of polyimide make it challenging to remove.

Both the bottom and top polyimide layers used in the flex need to be patterned. For both layers, we require that the polyimide patterning process does not leave residue, does not damage the layer underneath the polyimide, and can be completed in a reasonable amount of time. For the bottom layer of polyimide, we also require that the patterning process produce shallow-sloped sidewalls so that the wiring layer can fully coat them.

Photosensitive polyimides, such as the HD MicrosystemsTM HD 4100 series [68], can be patterned like photoresist by selectively exposing areas of the film to UV light through a patterned mask then dissolving in developer. One nice thing about photosensitive polyimides is that procedures have been developed to easily create sloped sidewalls, which are necessary for the first layer of polyimide [27]. In this work, we chose to use PI-2611, a non-photosensitive polyimide, because it is by far the lowest stress polyimide offered by HD MicrosystemsTM. A low-stress substrate is important for the flex because the superconducting properties of the wiring layer can be suppressed under mechanical stress. The residual stress of the PI-2611 is 2 MPa, while the next lowest stress polyimide offered, PI-6876G, has a residual stress of 16 MPa, and the residual stress of the photo-definable HD-4100 series is 34 MPa [70] [68]. The coefficient of thermal expansion (CTE) of the PI-2600, 3.3 ppm/°C, is also the most well-matched to silicon's CTE of 2.6-3.3 ppm/°C from room temperature to 400°C [92][70].

Polyimide, like other organics, can be etched in oxygen plasma, and this is usually the method of choice for patterning non-photo-sensitive polyimide. We use a dry plasma etch process to pattern the top layer of polyimide, as will be discussed in the next section. For patterning the first layer of polyimide, we use a novel shadow

mask process during spinning of the polyimide precursor that produces shallow-sloped polyimide sidewalls. This process will also be discussed more below.

We find that after the PI-2611 is soft-baked but before it is furnace-cured it is soluble in the developer 300 MIF. So it can be patterned by spinning a thick photoresist layer on top of the polyimide, exposing the photoresist to UV light through a mask, then placing in developer, similar to the wet-etching process that can be used to pattern the HD MicrosystemsTM PI-2545 polyimide [69]. The developer also quickly attacks aluminum, so this method did not work for patterning the top layer of polyimide. However, this method may be useful for patterning the top layer of polyimide more quickly than by oxygen etching after more process development. For example, a layer of chrome may be used to protect the aluminum bond pads and then removed after patterning the polyimide.

Fabrication of polyimide films from PI-2611

Polyimide precursor solutions consist of polyamic acid dissolved in a carrier solvent. The solution is spun onto a hard substrate to form a thin film. The film is soft-baked to evaporate off most of the solvent, then cured at high temperatures under a nitrogen atmosphere. In the furnace, the polymers undergo an imidization process and form cross-linking bonds with one another to form a polyimide film.

To coat a silicon wafer with a polyimide film, the PI-2611 solution is first poured onto the center of the wafer (about a 2.5 cm diameter area of solution is enough to coat a 100 mm wafer). Pouring the solution and not using a pipette minimizes air bubble formation in the solution. Air bubbles in the solution can produce indentations in the polyimide film and should be avoided. There are usually some air bubbles in the solution after pouring onto the wafer, which can be removed by sucking up with a pipette.

Besides lithography errors, most of our yield issues early on in the process development were due to fibers falling on the precursor film while it was still wet and becoming trapped in the polyimide solution.¹ The aluminum wiring layer either cannot fully coat the contaminants in the film, or the contaminants create stress points in the flex, cracking the traces. We find that we can consistently produce high-yield cables (>95%) if care is taken to keep the work area clean during spinning of the solution. In particular, it is important to clean the area before working, keep Texwipes and swabs out of the hood during spinning, and avoid leaning over the wafer or working at times when others are using the spin hood, as humans are a top producer of particles in the cleanroom.

After spinning the polyimide precursor film, the wafer is soft baked on a 90°C hotplate for about 5-10 minutes, until the film feels solid. Then, it is transferred to a 90°C furnace with nitrogen gas flowing at a rate of 5 sccm. The furnace temperature is ramped at 1°C/minute to 350°C, where it is held for 60 minutes, then the furnace is turned off and allowed to cool slowly to room temperature, which takes about 2 hours.²

The thickness of the polyimide film can be controlled by the spin speed: the faster the spin speed, the thinner the polyimide films. The PI-2611 solution is very viscous and designed to make thick polyimide films, from 4 μm (spin speed 5000 rpm) to 9 μm (spin speed 2000 rpm) [70]. We would like the flex to be at least 25 μm (1 mil) thick in total, including both the layer of polyimide under the traces and the layer on top, for mechanical robustness.

Thicker layers of polyimide can be formed, as suggested by HD MicrosystemsTM, by layering multiple films. It is necessary to either fully cure the preceding film in the furnace or perform a high-temperature soft-bake before applying another polyimide

¹We spin the polyimide film in the lithography room of the cleanroom, which is class 100. The rooms where etching and metal deposition are performed on the flex are class 1000.

²The slow ramp rate when raising or lowering the furnace temperature is necessary to prevent stress build-up in the film.

film on top. Otherwise, the base polyimide film will be attacked by the solvent in the PI-2611 solution and cracks will form. The full furnace cure takes about 6 hours, while the soft-bake option only requires baking the film for about 5 minutes at a higher temperature of 170°C, after the usual soft-bake at 90°C. However, we find that subjecting the first polyimide film (the one in contact with the silicon wafer) to high hotplate temperatures produces stress in the film, causing the cable to curl after release from the silicon wafer. We produced low-stress films by furnace curing the first film instead, then building up the next layers with the faster 170°C hotplate method, as suggested by Christiaens, 2009 [20]. We used this process for fabricating thick polyimide films for the ACTPol flex [75]. Fabricating thick polyimide films with this process takes about 6 hours longer than fabricating a single-layer polyimide film because of the extra furnace cure.

After making the ACTPol flex, we found that we could create a thick single-layer polyimide film using a very slow spin speed, saving 6 hours of process time. We spin the film for 15 seconds at 250 rpm, then 15 seconds at 500 rpm, and finally 60 seconds at 750 rpm. In between steps, the spin speed is ramped at a rate of 100 rpm/second. This spin recipe produces a polyimide film about 15 μm thick with good uniformity ($\pm 2 \mu m$) across the wafer. It is necessary to slowly accelerate the spin speed because the PI-2611 solution is so viscous. If the spin speed is brought to the final speed right away, the solution will fly off of the wafer instead of spreading out.

The polyimide coating sticks better to some substrates than others. In general, to achieve robust adhesion, we find it is best to always apply the VM-651 adhesion promoter, also from HD Microsystems, to the substrate before coating with polyimide. The VM-651 is a concentrated solution and is diluted with DI water by a factor of 1000:1 according to the manufacturers instructions before use. This solution is passed through a 2 μm filter and applied to the substrate so that the entire wafer is covered

with solution. The solution is left sitting on the wafer for at least 30 seconds before spinning the wafer at 3000 rpm for 30-40 seconds.

Adhesiveless shadow mask patterning of polyimide precursor solution

The first layer of polyimide needs to be patterned such that the area of the wafer where the bond pads will be is bare, and the area that will become the center of the cable is coated with polyimide. The polyimide sidewalls at the transition from coated to uncoated areas of the wafer must have a shallow slope so that the aluminum-wiring layer can fully coat the step. If the step is too sharp, the aluminum will coat the top and bottom of the step, but not the entire sidewall, and there will be discontinuities in the traces.

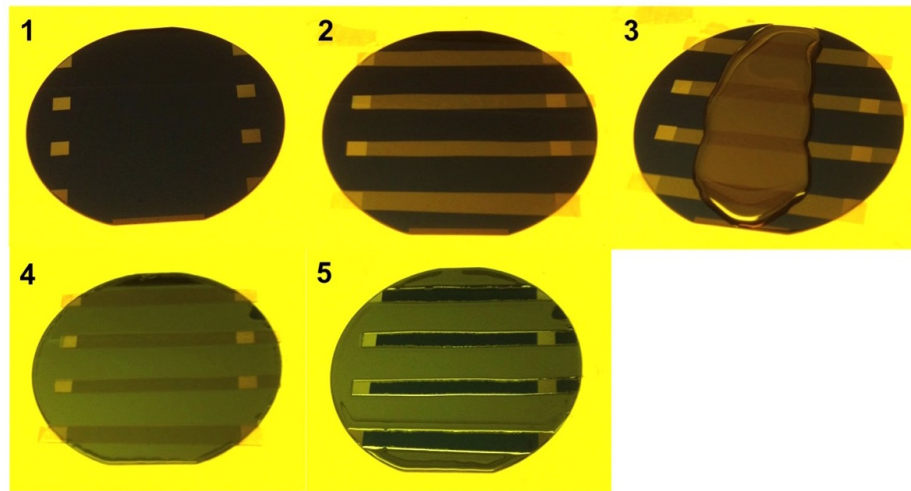


Figure 3.8: Adhesiveless shadow mask process for patterning PI-2611 precursor solution. Three pieces of the AdvACT flex shown in Fig. 3.7 will be fabricated on this wafer, with the traces running up and down in this figure. The flex bond pads will be placed in the areas of the wafer that remain uncoated with polyimide after this process. Step 1: The Al_2O_3 layer is patterned to mark where the Kapton[®] shadow mask should be placed. Step 2: Strips of 1 mil thick Kapton[®] are placed on markers. Step 3: The wafer and Kapton[®] are covered with PI-2611 solution. Step 4: The wafer is spun with the usual recipe, described in Sec. 3.3.2. Step 5: The Kapton[®] strips are removed and the PI-2611 solution relaxes at the boundary to create a shallow-sloped sidewall.

To pattern the base layer of polyimide with shallow-sloped sidewalls that the aluminum wiring layer can fully coat, we use an adhesiveless shadow mask to pattern the polyimide precursor solution during spinning. The shadow mask prevents polyimide from ever touching the protected areas, and stays on with no adhesive by electrostatic forces, so there is no residue left behind from this process. It is also faster than coating the whole wafer with polyimide and etching parts away, taking almost as little time as fabricating an unpatterned polyimide layer.

The steps for this process are outlined in Fig. 3.8. First, we pattern the dielectric layer used to passivate the silicon with markers that indicate where the shadow mask should be placed. (Step 1) Next, the shadow mask is placed on top of the wafer. (Step 2) For the Advanced ACTPol flex, we use 6.5 mm wide strips of 1 mil thick Kapton as the shadow mask. To ensure a good electrostatic seal between the shadow mask and the wafer, it is important to clean the wafer and shadow mask with solvents and an oxygen plasma etch and/or UV treatment before placing the shadow mask. The Kapton mask should also be flat and have smooth, flat edges for best results. Cutting the Kapton into strips with a razor blade or scissors can deform the Kapton film near the cut, producing ripples at the edges of the strips that prevent a good seal between the Kapton and the wafer. We found that cutting the Kapton using heavy, sharp “dressmaking” shears, designed for cutting fabric, produced smooth edges that sealed well.

After application of the shadow mask, the PI-2611 polyimide precursor solution is poured onto the wafer and shadow mask. (Step 3) To ensure the Kapton strips stay on the wafer during spinning, each of them should be at least partially covered in PI-2611. We spin the wafer at a slow rate, as discussed in Sec. 3.3.2, to form a thick polyimide film. (Step 4) The slow spin speed and ramp rate also ensures the Kapton strips will not shift or fly off during spinning. We find 1 mil thick Kapton films consistently stay in place very well at this spin speed, while thicker Kapton films

can be more challenging, presumably due to the higher mass to van der Waals force ratio.

After spinning the wafer, the Kapton strips are removed with tweezers. (Step 5) The polyimide solution relaxes at the edges, creating shallow-sloped sidewalls. Finally, the polyimide film is soft-baked on a hotplate and cured in the furnace according to the usual recipe (Sec. 3.3.2).

Dry etching of polyimide

We use a dry oxygen plasma etch to pattern the top layer of polyimide to expose the bond pads. The plasma can be excited by an inductor (inductively coupled plasma, or ICP) for an isotropic etch, or between two charged parallel plates, for a highly directional etch. It is also possible to have an inductor and parallel plates in one machine. In this case, the number of ions and directionality of the etch can be controlled separately, by changing the ICP and the bias power, respectively. However, at time of writing polyimide etching is only permitted in two plasma etching tools at the MNFL, the PlasmaTherm 790 (PT790), a purely parallel plate system and the PVA TePla M4L, a purely ICP etcher.

A photoresist mask may be used for etching thin layers of polyimide. However, because photoresists are organic films, they are also etched at a high rate by oxygen plasma. We find our photoresists etch about twice as fast as the polyimide. This means a 30 μm photoresist layer would be necessary to etch 15 μm of polyimide, which is not realistic for the photoresists we use.

An aluminum etch mask is recommended for etching thick layers of polyimide with oxygen plasma because the etch rate of aluminum in oxygen plasma is almost zero [93] [70]. Chrome and gold are also highly resistant to oxygen plasma etching and make good oxygen plasma etch masks [93]. To form a metal etch mask, we deposit a thin metal film on the polyimide then etch it into the desired pattern. It is necessary

to ensure very good adhesion between the polyimide and the metal etch mask, or the etch mask may bubble and peel off during etching. The proper procedures for ensuring good adhesion will be discussed in Sec. 3.3.3 below.

While aluminum is a very effective etch mask, it is difficult to remove after etching the polyimide without damaging the aluminum bond pads.³ We use chrome as the etch mask for the AdvAct flex because aluminum is only very slowly etched by the chromium wet etchant we use, Cyantek Cr-7 [93]. Therefore after the polyimide is etched, the chrome mask can be stripped in chrome etchant without damaging the aluminum bond pads.

The oxygen plasma recipes we use for etching polyimide in the PlasmaTherm 790 and the PVA TePla M4L are shown in Tables B.4 and B.5. The PT790 etches polyimide at a much faster rate than the TePla because the ion velocity is directed towards the sample. However, the PT790 etch leaves behind a grassy residue, shown in Fig 3.9, that is difficult to remove. It has been suggested that the residue may be due to the presence of two different phases in the polyimide film, one which is etched more easily than the other, or the orientation of the polymers with respect to the substrate [77] [23]. In our case, the grassy residue is most likely due to micromasking, as it is not a problem during isotropic etching of the polyimide [35].

Micromasking occurs during highly directional etches when particles from the chamber walls are sputtered and re-deposited on the sample surface where they act as a mask, preventing the etching of the tall pillars of material underneath. This problem does not occur with an isotropic etch because the polyimide can be etched from the sides then underneath the contaminate particle, and the contaminate is eventually removed. However, a purely isotropic etch is too slow to be practical- it

³It is best to remove all of the aluminum etch mask (or all outside of a small area around each bond pad) so that wire bonds will not short to each other if they touch the top flex surface. If the flex is simply placed in aluminum etchant the bond pads will of course be removed along with the etch mask. Because of the large height differences between the bond pads and the surrounding, polyimide-coated areas after the polyimide etch, patterning photoresist so it only covers each bond pad cannot be performed accurately.

would take over 4 hours to remove the top layer of polyimide. The ideal solution to this problem may be a tool capable of a combination parallel plate and ICP etch.⁴

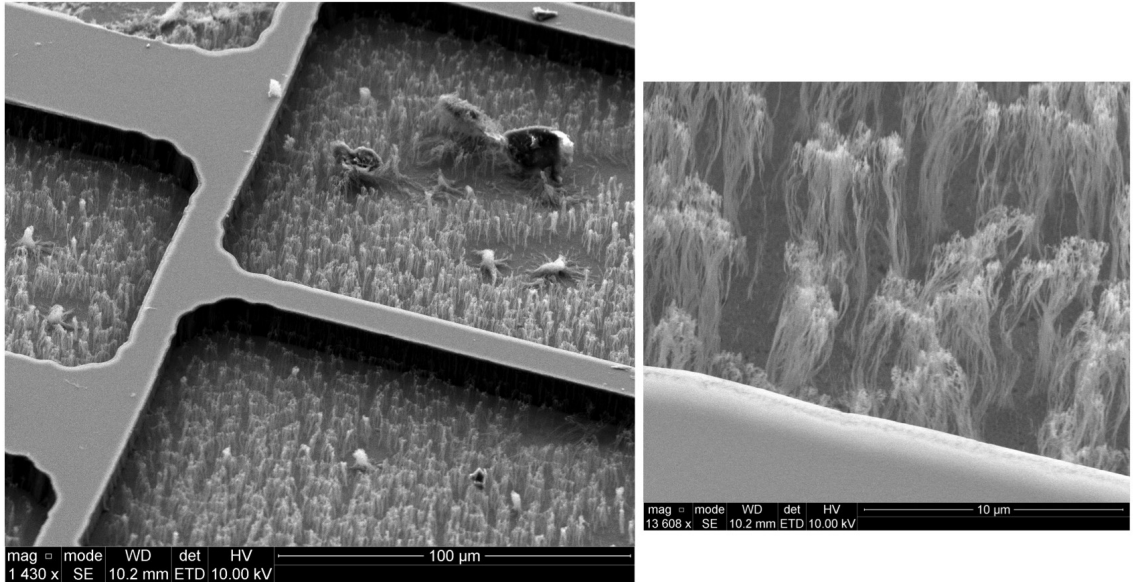


Figure 3.9: SEM images, taken at a 45° angle, of grassy residue left over after a 15 μm polyimide film was etched in the 790 with the recipe in Table B.4. The width of each grass piece is on the nanoscale. Images courtesy Pat Watson, Princeton University MNFL.

The grassy residue cannot be removed with an isotropic oxygen plasma etch. However, it can be removed by very slight mechanical force, for example by gently wiping the sample with a swab. One cleaning process that worked well, for the first batch of AdvAct flex, was soaking the wafer in warm 1165 (NMP-based photoresist stripper) overnight, then rinsing with a high pressure DI water hose. For the second batch of AdvAct flex, we removed the majority of the polyimide with the PT790, but left a layer about 2 μm thick. Then, we etched the flex in the TePla for 60

⁴In the literature, adding a small amount of CF₄ gas to the oxygen during etching is recommended to remove the grass because CF₄ etches silicon [95]. However, we did not notice an improvement when we added CF₄, indicating that our micromasking particles are not silicon-based. It is most likely the micromasking is due to partial sputtering and re-deposition of the reactor walls, which are aluminum. If this is the case, the problem cannot be solved by adding a chemical that would etch aluminum, as it would also attack our bond pads.

minutes. Because the TePla is an isotropic etch, the oxygen plasma was able to etch the polyimide underneath the grass and remove the grass with it.

3.3.3 Depositing and patterning metal on polyimide

We deposit metal on polyimide twice during the flex fabrication process: first to form the aluminum wiring layer and second to fabricate the chrome etch mask for etching the top polyimide layer. To ensure good adhesion, before depositing the metal we prep the polyimide film. First, we perform a dehydration bake on the polyimide film in a nitrogen atmosphere furnace to remove any water absorbed from the air. Then, we treat the polyimide film with an isotropic oxygen plasma etch for 5 minutes in the TePla, using the recipe in Table B.5. The oxygen plasma treatment enhances adhesion between polyimide and metal by introducing surface roughness as well as modifying the surface chemistry [54] [31] [29].⁵

We sputter a 400 nm aluminum film for the wiring layer with the Angstrom Engineering Metals Sputterer in the MNFL cleanroom. We choose sputtering over E-beam or thermal evaporation because it is well known to be the least directional of these deposition processes and therefore best for conformally coating sidewalls like our polyimide step. It is important to keep the chamber cool during the long aluminum deposition to prevent oxidation of the aluminum film. We first sputter 200 nm of aluminum, remove the wafers from the chamber and wait for the chamber and wafers to cool, then deposit another 200 nm.

We also use the MNFL's Angstrom Engineering Metals Sputterer to sputter 50 nm of chromium for the top polyimide etch mask. We pattern the aluminum wiring layer and the chrome etch mask by wet etching with Cyantek Al-11 aluminum etchant

⁵In fact, the effect of surface roughness on adhesion is so strong that a very strong mechanical adhesive polyimide tape has been created by etching the surface of a polyimide film into nano-scale pillars, mimicking the structures on geckos' feet that allow them to stick so well to surfaces [33].

and Cyantek CR-7 chrome etchant, respectively. Both etchants are weak acids and do not attack the polyimide film [70].

3.3.4 Release of polyimide from silicon substrate

Method 1: Gold release layer

To remove the silicon in the center of the cable, where we want it to be flexible, we developed a novel gold release layer procedure for the ACTPol flex [75]. The adhesion of PI-2611 to a gold surface is very poor if the VM-651 adhesion promoter is not applied before coating with the polyimide precursor [37] [67] [8]. We find that if we coat a gold-covered silicon wafer with polyimide, the polyimide film quickly delaminates from the wafer when placed in gold etchant. Due to the poor adhesion between gold and polyimide, the gold etchant is able to work its way between the gold layer and the polyimide film and quickly remove the gold layer, releasing the polyimide film.

Before fabricating the polyimide base layer, a gold film with a chrome adhesion layer is sputtered on the silicon wafer in the area that will become the center of the cable, where the polyimide will be released from the hard substrate. The first layer of the polyimide base is deposited without using the VM-651 adhesion promoter so that it will not stick to the gold. It is patterned during spinning with the shadow mask process in Sec. 3.3.2 to leave what will be the ends of the cable bare. This first layer is fully cured in the furnace instead of on a 170°C hotplate before subsequent layers are added, to prevent stress in the polyimide film (see Sec. 3.3.2). Then, a layer of the VM-651 adhesion promoter is applied. The next polyimide layer is patterned with the shadow mask process such that it covers a few millimeters more of the substrate than the first layer, so that the polyimide is securely attached to the hard substrate with the adhesion promoter.

The de-lamination is performed after the wafer is fully processed (base polyimide layer, wiring layer, and top polyimide layer all fabricated and patterned) because performing lithography on the flex after it is released from the silicon wafer is very difficult. The first step in the release is to backside dice the silicon wafer in the region where we would like the polyimide to be released. We use a 300 μm thick blade like a mill to cut the silicon down to a layer 20-50 μm thick. The dicing saw cuts naturally cleave the silicon that is left into slivers.

The wafer is then placed in chrome etchant to remove the portions of the chrome adhesion layer exposed by the dicing saw cuts. Finally, it is placed in warm gold etchant. Because the adhesion between the gold and polyimide is poor, the gold etchant comes up through the dicing saw cuts in the silicon and underneath the polyimide, quickly removing the gold and releasing what the dicing saw left of the silicon substrate.

Method 2: DRIE silicon etch

Another way to remove the silicon in the center of the cable is by etching away the 525 μm thick silicon wafer in the regions that will become the center of the cables. Deep etches in silicon are most often performed in a deep reactive ion etch (DRIE) tool using the Bosch process. To produce deep trenches with vertical sidewalls, the Bosch process uses a repeating cycle of short steps. In the first step of the cycle, the sample is coated with C4F8 gas, which forms a Teflon-like coating over the sample. Next, the C4F8 coating is removed from the bottom of the trench by a highly directional (high bias power) SF6 etch. Finally, an isotropic SF6 etch removes silicon from the bottom of the trench, but not the sidewalls, which are still protected by the C4F8 layer. The cycle is repeated until the desired etch depth is reached. We use the Samco 800 tool in the MNFL for this process. For our Samco 800 recipe, shown in Table B.6, one cycle takes 9 seconds and removes about 1.2 μm of silicon.

It is necessary to mount the flex wafer onto a carrier wafer before etching. In the Samco 800, the wafer is held on an electrostatic chuck that makes contact with the outer ring of the wafer. Helium gas is blown on the back of the wafer to keep it cool, and the front of the wafer is in the reactant chamber. So, the wafer itself forms a wall between the helium gas region and the reactant chamber. If the wafer is etched completely through, there will be a leak. Similarly, we would not want to etch through the silicon wafer in some areas and leave only the polyimide film to provide the seal. The polyimide film could be damaged by the pressure difference and the machine could be damaged as well.

To enable alignment to the flex wiring layer when patterning the backside of the wafer, we dice the wafer into a rectangle with fixed distances between the cuts and the edges of the flex bond pads before mounting to the carrier wafer. Then, we mount the wafer face down onto the carrier wafer with Crystalbond™ 509. It is important to make sure the Crystalbond™ layer is even in thickness and free of air bubbles so that there are not pressure points on the polyimide film after the silicon is etched away. First, we place the carrier wafer and flex wafer on a hotplate above 150°C and coat each with a thin layer of crystal bond. Then, we place one wafer on top of the other and apply pressure with a spring-loaded press, also heated to above 150°C on the hotplate. We leave the wafer in the press for a few minutes, until all air bubbles and excess Crystalbond™ have oozed out. Next, we remove the press from the hotplate and let the wafer cool to room temperature. Finally, we remove the wafer assembly from the press and clean both sides well with acetone, methanol, and isopropanol to remove any Crystalbond™.

Next, we fabricate a thick photoresist AZ4330 mask on the back of the flex wafer, using the diced edges of the wafer to align the mask.⁶ Then, we perform the silicon

⁶Note that we mount the wafer on the carrier before spinning and patterning the photoresist mask. This is because some Crystalbond inevitably ends up on the front and back surfaces of the wafer assembly during mounting and both surfaces need to be free of Crystalbond before placing in

etch in the Samco 800 using about 450 cycles of recipe 3, shown in Table B.6. To reduce stress in the flex and prevent curling, we remove what is left of the Al_2O_3 etch stop layer under the polyimide by placing the wafer assembly in aluminum wet etchant, heated to about 50°C . Unlike strong acids that could be used to remove the Al_2O_3 , such as hydrofluoric (HF) acid, the aluminum etchant will not attack the polyimide [70]. The CrystalbondTM layer between the carrier wafer and the top surface of the flex wafer protects the aluminum bond pads from the aluminum etchant. Next, we dice the flex while it is still mounted to the carrier wafer, again using the flex wafer's diced edges as alignment marks. The carrier wafer supports the fragile polyimide film during dicing. Finally, we remove the flex from the carrier wafer by soaking in acetone, rinse with methanol and isopropanol, and dry with nitrogen.

Summary: Release of polyimide from silicon substrate

We find the DRIE process is an improvement over the gold release process in terms of both process time and the quality of flex produced and are currently using this process for the AdvACT flex [76]. Initially, we had trouble removing the silicon by the DRIE process without damaging the polyimide layer and developed the gold release process described above. The DRIE process partially etched and created bubbles in the polyimide film. We find we are able to prevent etching of the polyimide layer with a thin (110 nm) Al_2O_3 etch stop layer. We grow the Al_2O_3 by ALD before application of the base polyimide layer and it also acts as the silicon passivation layer. The SF_6 plasma only very slowly etches polyimide, but because the silicon etch is uneven (the edges of the exposed area are etched before the center), some areas of the polyimide film are exposed to the etch for 10 minutes or more before all the silicon is completely removed. We have been able to eliminate the formation of bubbles in the polyimide film during the DRIE process by applying the VM-651 adhesion promoter

the Samco 800. The same solvents that dissolve Crystalbond dissolve photoresist, so the photoresist needs to be applied after mounting the wafer on the carrier and cleaning off the Crystalbond.

before spinning the polyimide film, ensuring even application of Crystallbond when mounting the flex wafer to the carrier, and performing a dehydration bake of the flex wafer before mounting it on the carrier, which removes any water absorbed by the polyimide film that may cause bubbles later [34].

3.3.5 AdvACT flex fabrication process summary

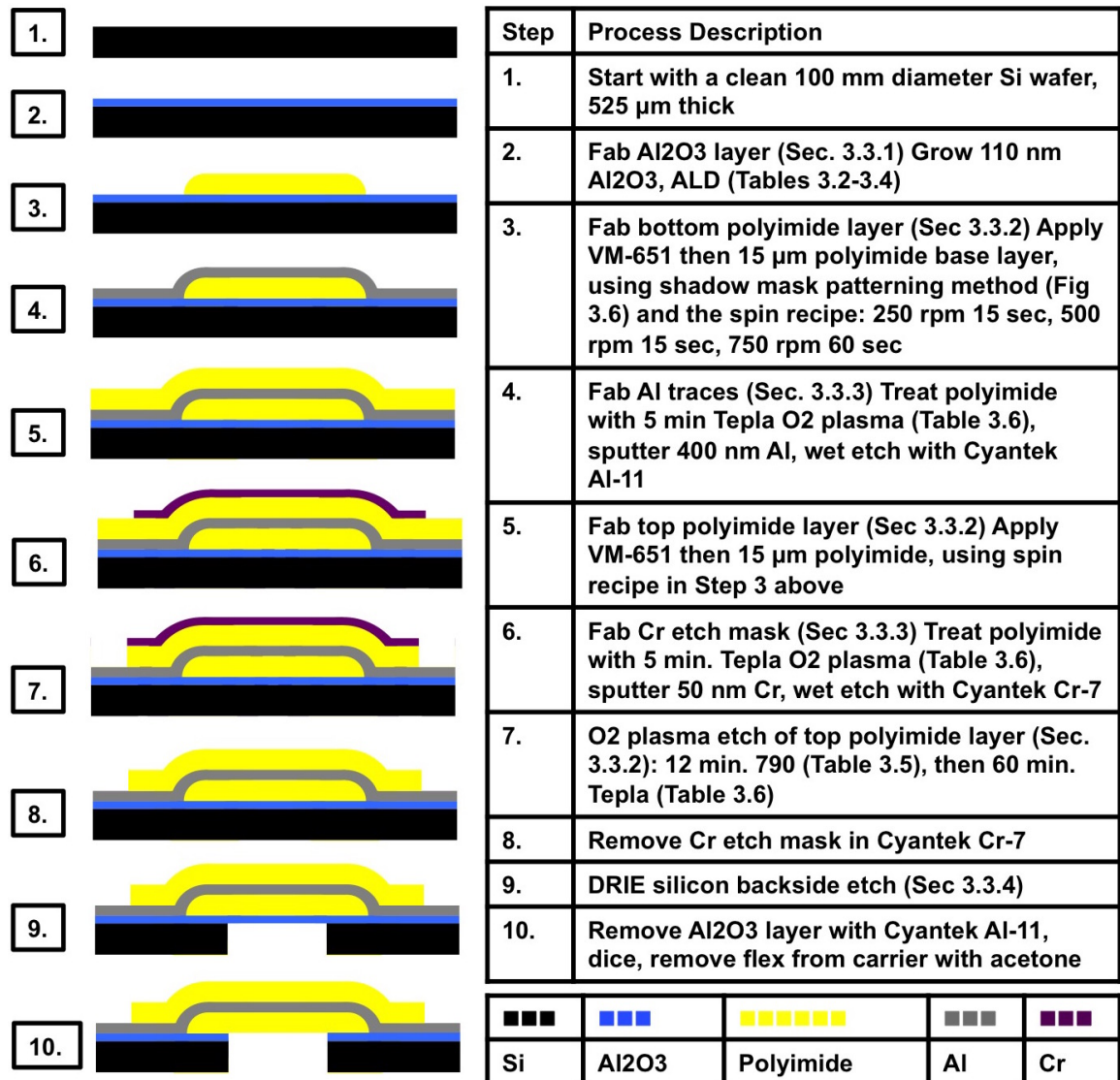


Figure 3.10: An overview of our current best flex fabrication process. Diagrams not drawn to scale.

The current best version of the process, used for fabricating the AdvACT HF array flex, is outlined in Fig. 3.10. Details of each step are discussed in the referenced previous sections of this chapter. The top and bottom polyimide films are $15\ \mu\text{m}$ thick and we fabricate each as one layer using the slow speed recipe in Sec. 3.3.2 To etch the top layer of polyimide, we use the PT790 recipe (Table B.4) to remove the bulk of the polyimide, then remove the last $2\ \mu\text{m}$ with the TePla (Table B.5) to remove the grassy residue. We remove the silicon in the center of the cable using the DRIE process discussed in Sec. 3.3.4.

3.4 Flex Performance

The flex is currently being used successfully on ACT in the ACTPol PA3 semi-hex assemblies, as described in the previous chapter. We have also performed experiments in the lab to test the flex performance. For ACTPol and AdvACT, the most important properties of the flex are the superconducting critical current of the traces, electrical yield, ease of assembly, wire bond strength, and resilience to mechanical stress and cryogenic cycling.

3.4.1 Superconducting properties

As discussed at the beginning of the chapter, we would like the flex traces to carry a high enough critical current that they remain superconducting when the TES is biased for CMB observations and throughout an IV curve acquisition. The TES current has two local maxima in an IV curve as shown in Fig. 2.6. On the low resistance side the maximum TES current is equal to or less than the TES critical current at the operating bath temperature.⁷ Typically, ACTPol TES critical currents at 100 mK are about 1 mA. On the high resistance side, the maximum TES current

⁷Because we take the IV curve from high to low I_{bias} at a non-zero speed, there is some heating so the maximum TES current here is slightly less than the TES critical current.

is $I_{bmax}/(R_n/r_{sh} + 1)$, where I_{bmax} is the maximum bias current applied during the IV curve. The maximum bias current that can be applied with the MCE bias DAC is about 7 mA with typical ACTPol cable resistance values. Using the lowest observed R_n s in the ACTPol detectors, about 4 m Ω , the maximum possible TES current on the high side of the IV curve is 300 μ A. Therefore, we would like the flex traces to have an I_c of at least 1 mA at 100 mK.

The ACTPol flex has performed well in PA3 without any critical current issues. Tests in the lab showed the critical current of the ACTPol flex was above about 6 mA, the highest current we could apply with the MCE, at temperatures 1 K and below. As the critical current increases with decreasing temperature, this along with their in-field performance indicates the critical current of the flex traces exceeds the requirement of about 1 mA at our nominal operating temperature of 80 mK. The critical temperature of the aluminum traces matched the nominal value of 1.2 K within the +/- 50 mK error bounds, indicating that the aluminum produced by our process did not have quality issues that would affect the critical temperature and current, such as magnetic impurities or stress.

We have also made preliminary measurements of the AdvACT flex I_c . The thickness and width of the aluminum traces in the AdvACT flex is identical to the ACTPol flex, so we expect this flex to carry the same I_c . We measured the I_c of 36 AdvACT flex traces at 500 mK. Three groups of 12 traces were wire bonded in series, and a 4-lead resistance measurement of each group was performed. Currents of 1 mA, 3.16 mA, and 10 mA were passed through the traces and the resistance was measured to see if the traces were still superconducting. The I_c at 500 mK exceeded 1 mA for all 36 traces and at least 24 traces held above 10 mA of superconducting current. Because I_c increases with decreasing temperature [88], this indicates that I_c at our operating temperature of 80 mK will well exceed the AdvACT requirement of about 1 mA.

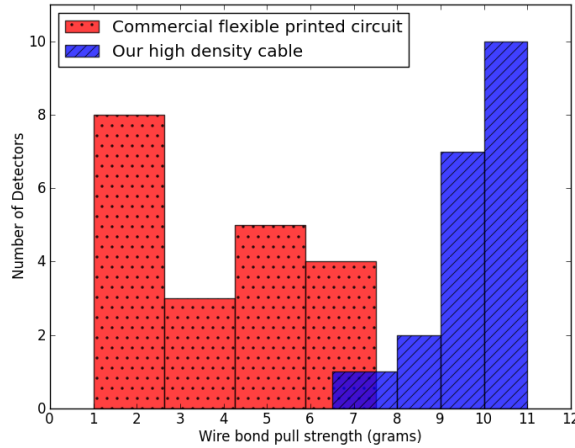


Figure 3.11: This histogram shows results of strength measurements of wire bonds on a piece of Tech-Etch flex mounted with Stycast 1266 to a silicon stiffener and on one of the high-density superconducting cables described in this paper. After thermal cycling of the two assemblies down to 25 mK, the bond strengths of 25 wires from each assembly were measured by a destructive pull test. Data courtesy Bert Harrop.

3.4.2 Electrical yield

As discussed in Sec. 3.3.2, the electrical yield of the flex is most affected by lithography errors during the wiring layer patterning and contaminants in the base polyimide layer. By paying attention to these issues, we can now consistently produce high yield flex. The three ACTPol PA3 semihexes assembled with this flex had an average 92% yield at 100 mK. The first three pieces of AdvACT flex produced for the HF array have an average room temperature yield of 97%.

3.4.3 Ease of assembly and wire bond strength

As described earlier in this chapter, the flex bond pads sit on a hard silicon substrate for a robust wire-bonding interface. This makes wire bonds to the flex consistently strong for a high electrical yield assembly, as shown in Fig. 3.11. It also ensures the assembly will be completed on time because the wire bonding will go very smoothly, even allowing the use of the bonder’s automatic mode.

3.4.4 Robustness under mechanical and cryogenic stress

We have also tested the AdvACT flex response to cryogenic cycling and mechanical stress. This is important because the flex needs to withstand handling during assembly and the many cryogenic cycles during observations on ACT and detector tests in the lab. The flex was examined under the microscope and 260 traces were probed for continuity before and after the tests to detect any changes in the flex due to the tests. First, the flex was cryogenically cycled between room and liquid nitrogen temperature 10 times. Next, the flex was bent 180° at a 1.3 mm radius of curvature 10 times in one direction and 10 times in the other. All 260 traces were continuous and no cracks in the traces were observed under the microscope before and after both tests.

3.5 Conclusion

We have developed a novel microfabrication process to produce high-density superconducting cables with a robust wedge wire-bonding interface. The cables have been successfully fielded in the ACTPol PA3 array, and meet the AdvACT and ACTPol critical current, mechanical robustness, and cryogenic robustness requirements. We have produced flex with a $100\ \mu\text{m}$ pitch for ACTPol and a $70\ \mu\text{m}$ pitch for AdvACT. Assuming the ACTPol/AdvACT performance requirements, superconducting flex with a $40\ \mu\text{m}$ pitch should be possible using this recipe.

3.6 Acknowledgements

In additions to the acknowledgements at the beginning of this thesis, I would like to acknowledge the following people for their contributions to the research in this chapter. Kevin Mizes helped develop the DRIE process for removing the silicon in the center of the cable. Prajwal Niraula performed mechanical and cryogenic tests

on the flex and the room temperature probing. Sara Simon helped with the ACTPol flex fabrication. Patty Ho helped with making the first AdvACT flex pieces and will now continue production on her own. Preliminary tests of the critical current of the ACTPol and AdvACT flex were performed at Cornell University by Azar Eyvazov, Dr. Shawn Henderson, Brian Koopman, and Prof. Michael Niemack. Patricio Gallardo, also at Cornell, performed gold film depositions for the ACTPol flex.

Chapter 4

PA3 Detector Array

The third ACTPol array, PA3, features 90/150 GHz dichroic, polarization-sensitive detectors. The PA3 detectors are the first multichroic polarimeters installed on ACT. By measuring a 90 GHz and a 150 GHz band and both polarizations on each pixel, PA3 was projected to be over 30% more sensitive than an array measuring 90 GHz alone [26]. The measured sensitivity of the PA3 array is $\leq 10 \mu K \sqrt{s}$, the highest yet installed on ACT [44].

In this chapter, we describe some of the PA3 detectors' properties, how these properties affect detector performance, and methods for measuring them. First, we characterize some of the detectors' important dark properties, the TES critical temperature and the thermal conductivity between the TES island and the bath. Then, we discuss the optical efficiency of the detectors.

4.1 PA3 array overview

The PA3 pixels are shown in Fig. 2.1. Light is split into orthogonal polarization components and coupled to on-chip signal lines by the OMT, then split again by on-chip filters into 90 GHz and 150 GHz bands. Each polarization and frequency

combination is measured by its own TES bolometer, of which there are four per pixel.

There are three “hex” wafers, FH2, FH3, and FH4, and three “semihex” detector wafers, SH8B, SH1A, and SH1B in the PA3 array, as shown in Fig. 2.8. As discussed in Chapter 2, the hexes are each fabricated on one 76 mm silicon wafer, and two semihexes are fabricated on one 76 mm silicon wafer. Semihexes with the same number, such as SH1A and SH1B, were fabricated on the same 76 mm silicon wafer.

There are 255 pixels, 15 Johnson noise resistors, 1020 optically sensitive TESes, and 18 dark TESes (not connected to any signal lines) in the PA3 array. With our 32 column by 32 row time-division multiplexing system, we read out 247 pixels with 988 optically sensitive TESes, 9 Johnson noise resistors, and 12 dark TESes. Because it is the last array assembled, our most advanced assembly techniques were used for PA3 and it has the highest assembled TES electrical yield of the three ACTPol arrays, 86%.

4.2 Dark measurements

In this section, we discuss the PA3 detectors’ TES T_c and the thermal conductivity between the TES island and the bath. As discussed in Chapter 2, in thermal equilibrium, the power on the TES island is equal to the power conducted from the TES island to the bath:

$$P_\gamma + P_{bias} = \kappa(T^n - T_{bath}^n). \quad (4.1)$$

We define P_{sat} as the amount of power needed on the TES island to drive its temperature to T_c when the bath temperature is T_{bath} :

$$P_{sat} = \kappa(T_c^n - T_{bath}^n), \quad (4.2)$$

where we define T_c as the temperature at which the TES resistance is 90% of the normal resistance, R_n .

We can tune P_{sat} by changing κ , which is proportional to the detector leg width, and by changing the TES T_c . The value of the exponent, n , depends on the material and thickness of the detector legs and the operating temperature. It is about 3-3.5 for the ACTPol detectors and we do not attempt to tune this value.

The P_{sat} needs to be larger than the optical loading on the detector, so that the detectors do not saturate. We do not want to make P_{sat} too large because we also want to minimize the thermal noise of the detector, which is given by:

$$NEP = \sqrt{4k_B T_c^2 G f_{link}}, \quad (4.3)$$

where G is the thermal conductivity between the TES island and the bath and f_{link} is a constant given by the dominant type of phonon scattering in the legs. The optimal T_c minimizes the thermal noise of the bolometers at the given n value and operating bath temperature, T_{bath} . For the PA3 detectors, we chose a T_c target of 150 mK.

After T_c is chosen, assuming n is fixed, P_{sat} is set by κ . We adjust κ by changing the width of the legs that connected the TES island to the bath. Because the thermal noise increases with increasing κ , we want to select a κ such that the P_{sat} is as close to the predicted loading as we can justify. For PA3, we target P_{sat} values between 10 and 14 pW at a T_{bath} of 100 mK to meet these goals and to ensure the detector time constants will be small enough to keep up with our scan speed.

In addition to meeting the requirements discussed above, it is also important for the P_{sat} s to be uniform within each detector wafer. To reduce the number of wires routed from room temperature to cold stages of the cryostat, each TES bias line biases 32-96 TESes on a detector wafer in series. If all TESes on each bias line cannot be

biased onto their transition regions with one I_{bias} value, we will lose detectors during observations.

4.2.1 Dark measurement methods

We measure the TES critical temperature and the thermal conductivity between the TES island and the bath by taking data under dark conditions at a series of different bath temperatures.

Typical method

During dark tests, P_γ is zero and Eq. 4.1 becomes:

$$P_{bias} = \kappa(T^n - T_{bath}^n). \quad (4.4)$$

We would like to take detector data at known bath temperatures and solve for κ and n in this equation. However, while we can measure P_{bias} and T_{bath} , we can't directly measure the TES temperature, T . We can only directly measure the TES resistance and current.

In general, the TES resistance is a complicated function of T and I , and its exact form is unique to each TES. In order to determine T from R and I , we would need to measure the $R(T, I)$ function.¹ However, when the TES resistance is close to R_n , the dependence of the TES resistance on current at constant temperature is very small and the TES resistance is very nearly only a function of temperature.

So, we expect that anytime the TES resistance is 90% R_n , the TES temperature is a constant value independent of bias current. This means we can measure $P_{bias}(0.9R_n)$ at each T_{bath} and fit for the constants n , κ , and $T(0.9R_n)$:

¹It is a good assumption that the partial derivatives of R with respect to I and T are always positive, so that R is monotonically increasing as a function of I or T , and $T(I, R)$ is well defined.

$$P_{bias}(0.9R_n) = \kappa(T(0.9R_n)^n - T_{bath}^n). \quad (4.5)$$

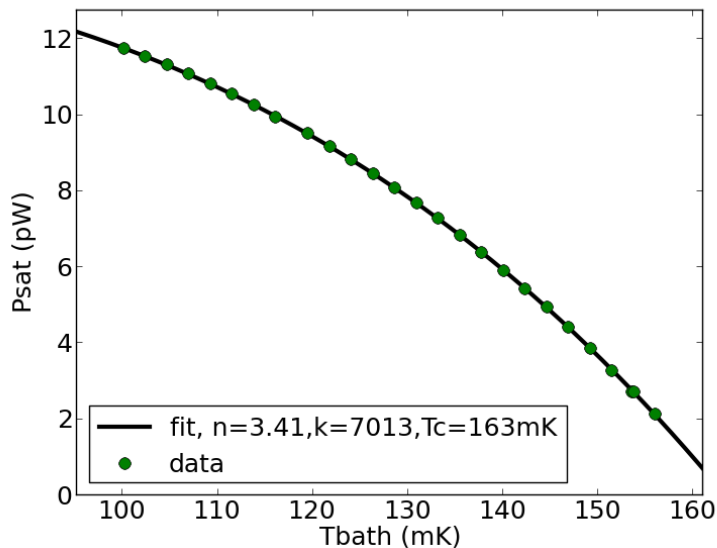


Figure 4.1: Example of G fit to $P_{sat}(0.9R_n)$ vs. T_{bath} data from the FH4 individual wafer cool down. The data shown for PA3 detector col5, row30, ID 965.

We choose $90\%R_n$ and not $95\%R_n$ or $100\%R_n$ because $P_{bias}(xR_n)$ can be difficult to calculate from an IV curve when x is greater than 0.9.

Effect of T_{bath} measurement errors

We measure T_{bath} with a thermometer clamped to the copper hardware to which the detector wafers are heat sunk. (We do not attach a thermometer to the detector wafer itself because we do not want to risk breaking it.) When the thermometer temperature is different from the detector's actual bath temperature due to thermal gradients, the measured T_{bath} is not equal to the actual detector T_{bath} value.

We made measurements of κ , n , and T_c as described above when PA3 was on the telescope. When the array is installed on the telescope, we do not have the tools for good control of the array T_{bath} because we do not actively servo the T_{bath} during

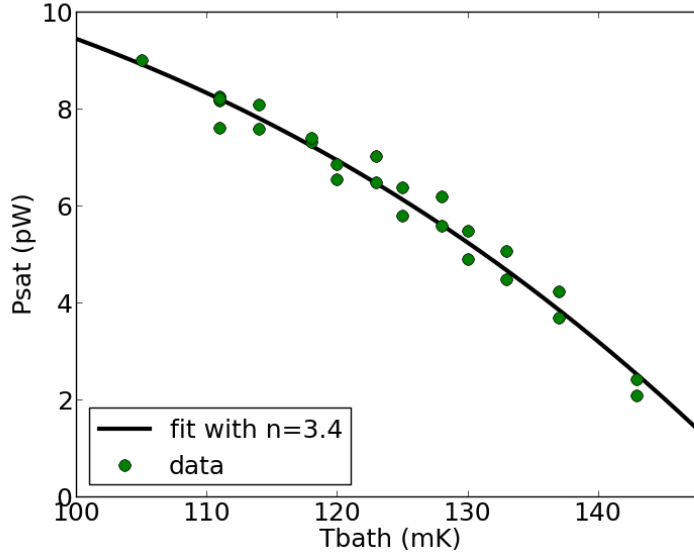


Figure 4.2: Example of G fit to $P_{sat}(0.9R_n)$ vs. T_{bath} data using the telescope data. The data shown for PA3 detector col5, row30, ID 965.

CMB observations. The T_{bath} measurement for this data set is therefore only accurate within about 5 mK or so. As shown in Fig. 4.2, there is quite a bit of scatter in the data points about the fit line due to the scatter in the T_{bath} measurement.

PA3 dark measurement method

Without knowing the T_{bath} values at which a set of IVs were taken, we can still calculate the relative κ and T_c between two detectors from their sets of $P_{bias}(0.9R_n)$ values at those T_{bath} values. Assuming all detectors had the same T_{bath} temperature when each IV was taken (and note this would not be true if there were thermal gradients across the array), there is a linear relationship between any two detectors' sets of $P_{bias}(0.9R_n)$ values:

$$\begin{aligned}
m * P_{bias}(0.9R_n)_1 + b &= P_{bias}(0.9R_n)_2, \\
m &= \kappa_2/\kappa_1, \\
b &= \kappa_2(T_{c2}^n - T_{c1}^n).
\end{aligned}
\tag{4.6}$$

By plotting one detector's $P_{bias}(0.9R_n)$ set vs. the other and fitting a line, we can find the relative κ and T_c between the two detectors.

We measured the T_c , κ , and n of some detector wafers in individual detector wafer cool downs in the Princeton University dilution refrigerator before assembling the PA3 detector array. During these measurements, we had good T_{bath} measurements (see Fig. 4.1) and therefore calculated accurate T_c , κ , and n values. The wafers chosen for the PA3 array for which we had made successful dark measurements at Princeton are hex wafer FH4 and semihex SH1a.

We use the T_c and κ values from the dark measurements of the FH4 wafer at Princeton to normalize the relative κ and T_c calculated on the telescope. We also assume that all detectors have the same n value of 3.4, the median value measured for FH4 detectors during the Princeton tests. This is a good assumption because n depends on the leg geometry and material, which remain relatively constant throughout the array.

4.2.2 TES critical temperature

The ACTPol TESes are molybdenum (Mo) and copper (Cu) bilayer thin films. The T_c of molybdenum is about 915 mK [32] and copper does not superconduct. By the proximity effect, a Mo/Cu bilayer film (provided each layer is thin) acts as one superconducting film with a lower T_c than molybdenum. Increasing the thickness of the copper film will lower the T_c , and increasing the thickness of the molybdenum film

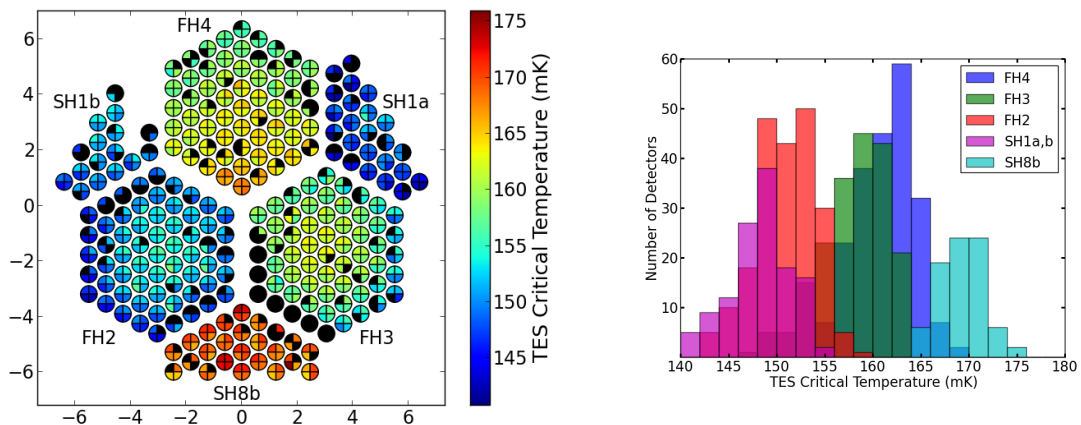


Figure 4.3: T_c data for PA3. *Left*: Array plot of detector T_c , where the x,y position of the circles represents the x,y position of the pixels in the array and the colors indicate the T_c s of the four TESes in the pixel. TESes detecting radiation in the 90 GHz band are shown in the upper quadrants, and TESes detecting radiation in the 150 GHz band are shown in the lower quadrants. Note that we do not expect any difference in T_c between 90 GHz band and 150 GHz band TESes. *Right*: Histogram of PA3 T_c values.

will raise the T_c [21] [63]. By changing the relative thicknesses of the molybdenum and copper films, we are able to tune the T_c of the TES to the desired value.

The target T_c for all PA3 detector wafers was 150 mK. As shown in Fig. 4.3, the T_c s of the PA3 Mo/Cu bilayer TESes vary from about 140 mK to about 175 mK. The median T_c across the array is 157 mK and the standard deviation is 7 mK. The variation in T_c is caused by slight variations in the Mo and Cu layer thicknesses as well as differences in film stress and heating during processing.

4.2.3 Thermal conductivity between TES island and bath

After the target T_c is selected, we tune the target P_{sat} by changing the design width of the SiN legs by which the TES island is suspended. There is in general a linear relationship between κ and the leg width. To meet our P_{sat} target of 10-14 pW at a T_{bath} of 100 mK, we chose a leg width of 22.5 μm for the 90 GHz detectors and 24.5 μm for the 150 GHz detectors.

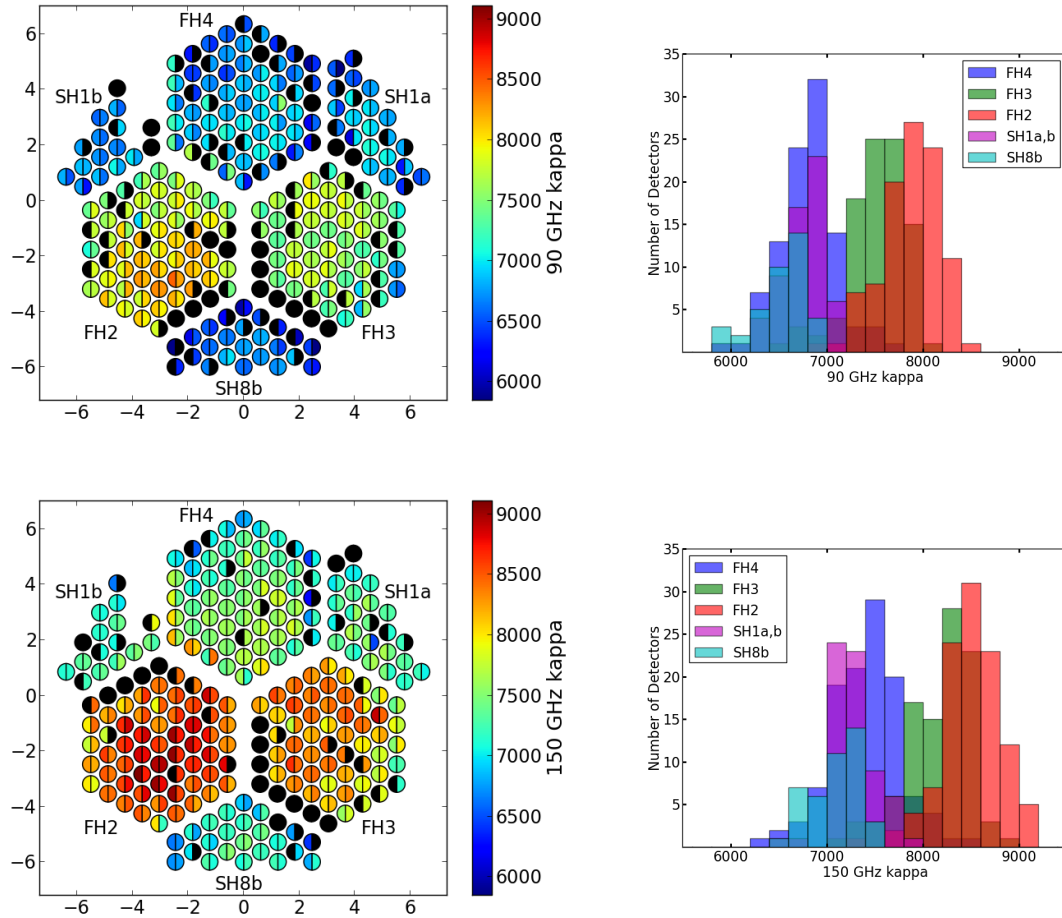


Figure 4.4: PA3 κ data. Values for 90 GHz detectors, which have a target leg width of $22.5 \mu m$, are shown in the top plots, and values for the 150 GHz detectors, which have a target leg width of $24.5 \mu m$, are shown in the lower plots. *Left, top (bottom)*: Array plot of detector κ , where the x,y position of the circles represents the x,y position of the pixels in the array and the colors indicate the κ values of the two 90 (150) GHz TES bolometers in the pixel. *Right top (bottom)*: Histogram of the PA3 array 90 (150) GHz κ values.

In Fig. 4.4, the measured κ values are shown. The median κ values for the 90 GHz and 150 GHz detectors on the hex wafers FH2 and FH3 are about 13-14% higher than the median 90 GHz and 150 GHz κ values on the other wafers. The FH2 and FH3 wafers were processed at the same time, so it is likely the same problem occurred for both during fabrication. The difference in κ is larger than we would expect from variations in over or under etching of the legs. It is possible that some residue, such as photoresist, may not have been thoroughly cleaned off the legs after the etch, increasing their thermal conductance.

4.2.4 P_{sat} at operating bath temperature

Our main concern with how well we met our κ and T_c targets is how it affects P_{sat} . (We also want to make sure they are not so far off from our targets that the thermal noise of the detectors is high.) The P_{sat} s need to be high enough that the detectors will not saturate under normal operating conditions. It is also important for P_{sat} s not to vary too much amongst TES bolometers on one bias line, so that they can all be biased onto the transition with the same I_{bias} value.

The operating T_{bath} of PA3 on the telescope is the highest of the three arrays (for reasons we have not yet determined). As shown in Fig. 4.6, T_{bath} also fluctuates over the Season 3 observations due to some problems with the cooling system. The P_{sat} s shown in Fig. 4.5 are calculated at the median Season 3 PA3 T_{bath} , 123.5 mK, using the κ and T_c values shown in Figures 4.4 and 4.3.

In Fig. 4.6, the biasability of the PA3 detectors is shown. As T_{bath} and atmosphere loading increase, the detectors are more likely to saturate. We use the atmosphere partial water vapor, measured at the APEX site, divided by the sine of the elevation of the telescope ($PWV/\sin(\text{el})$) as a measure of the atmosphere loading on the detectors. The P_{sat} s are high enough that almost all of the detectors are operational under normal conditions.

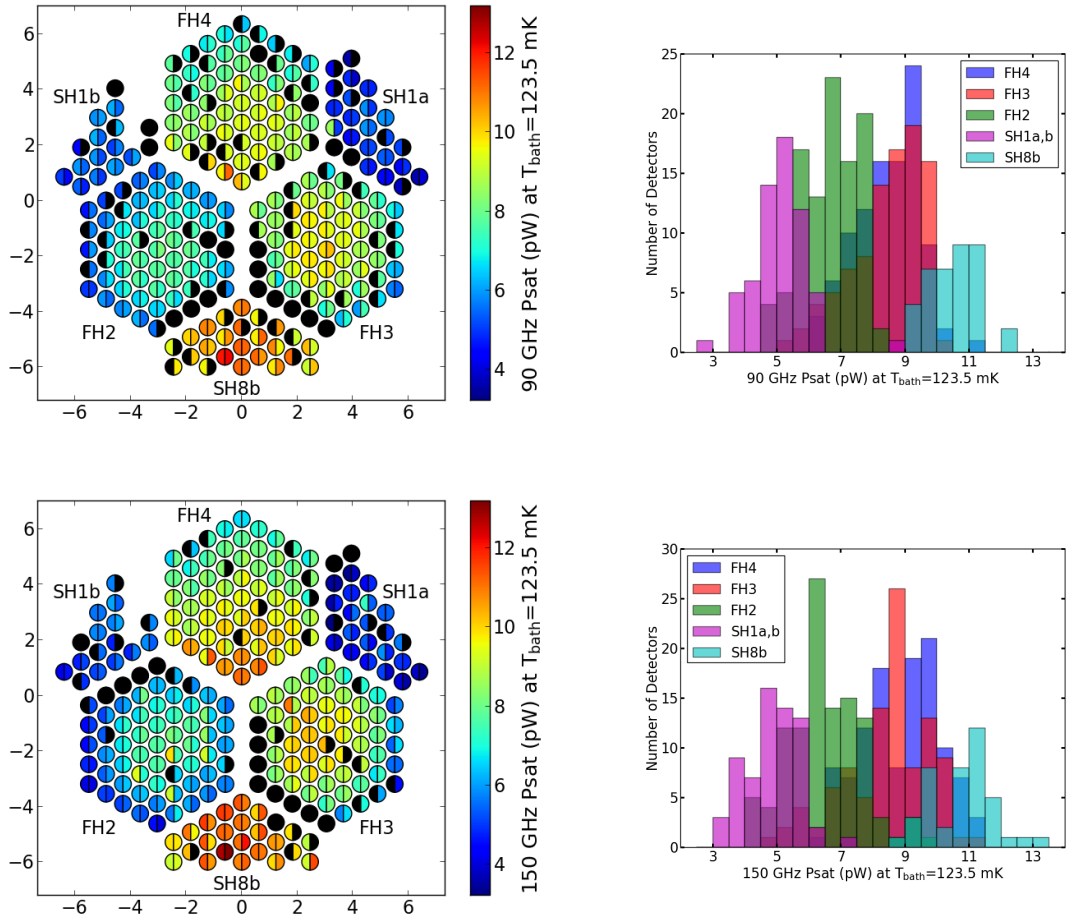


Figure 4.5: PA3 P_{sat} values at the median operating T_{bath} , 123.5 mK. The P_{sat} s are calculated from the T_c and κ values shown in Figures 4.3 and 4.4. The 90 GHz P_{sat} values are shown in the top plots, and the 150 GHz P_{sat} values are shown in the bottom plots. *Left, top (bottom)*: Array plot of detector P_{sat} , where the x,y position of the circles represents the x,y position of the pixels in the array and the colors indicate the P_{sat} values of the two 90 (150) GHz TES bolometers in the pixel. *Right top (bottom)*: Histogram of the PA3 array 90 (150) GHz P_{sat} values.

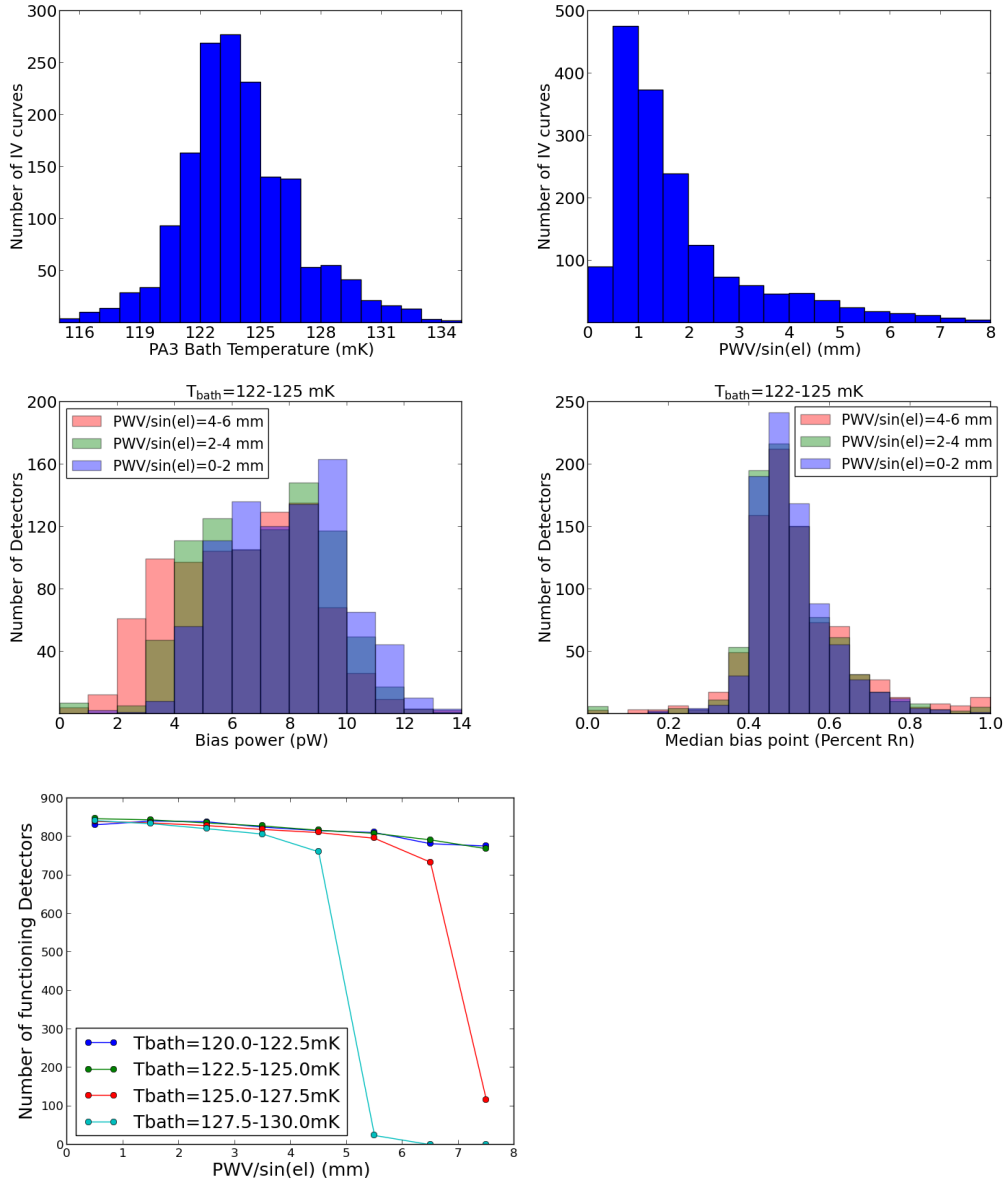


Figure 4.6: These plots refer to Season 3 PA3 data from Feb 15 2015 to August 4 2015. *Upper left:* Histogram of the PA3 Bath temperature when an IV curve is taken. The T_{bath} is the median result calculated from the PA3 dark detectors as described in the text. *Upper right:* A measure of the amount of optical loading at the time an IV curve was taken. The PWV in mm is based on data from the APEX site. *Middle Left:* Median bias power applied to each TES when the target bias point is 50% R_n , for the indicated range of loading.. *Middle right:* Median bias point (defined as the % R_n of the TES resistance) of each TES when the target bias point is 50% R_n , for the indicated range of loading. *Lower left:* The number of functional detectors, defined as those biased between 20% and 80% R_n and with 1 pW or more of bias power, as a function of loading conditions. The highest possible number is 850, the number of electrically connected TESes in the PA3 array.

When the bath temperature of the array is between 120 mK and 130 mK, which it is 95% of the time, the number of operational detectors does not start to significantly decrease until $\text{PWV}/\sin(\text{el})$ is above 5 mm. The P_{sat} s are uniform enough that the detectors are mostly biased onto their transition near 50% R_n under normal T_{bath} and atmosphere loading conditions. At the median bath temperature and when the atmosphere loading $\text{PWV}/\sin(\text{el})$ is less than 2 mm, 99% of the live detectors are biased between 20% and 80%, 95% are biased between 30% and 70% R_n , and 81% are biased between 40% and 60% R_n .

It should be noted that the spread in the % R_n bias point for detectors on one bias line depends not only on the spread in the detectors' P_{sat} s but on the width of the resistive transition as a function of I_{bias} current as well. If the transitions are narrow, there will be a larger spread in % R_n for a given spread in P_{sat} than if the transitions are wide.

4.3 Detector optical efficiency

To maximize the signal to noise ratio of the detectors, we would like their optical efficiency to be as high as possible. The PA3 detectors lose some sensitivity (which is gained back by the detectors being dichroic) due to optical signal loss in the on-chip filters defining the 90 GHz and 150 GHz bands. Additional optical efficiency loss occurs due to signal absorption by the SiO_x dielectric on which the signal lines are fabricated and some reflections in the signal lines. The loss tangent of the SiO_x is highly dependent on fabrication parameters, and may vary [59].

It is also possible for signal absorption to occur in the signal lines themselves. Although superconducting wires can carry a dissipationless DC current, there is always some loss (at non-zero temperatures) when AC signals are transmitted due to the normal electrons, or quasiparticle excitations, in the wire [88]. We expect the amount

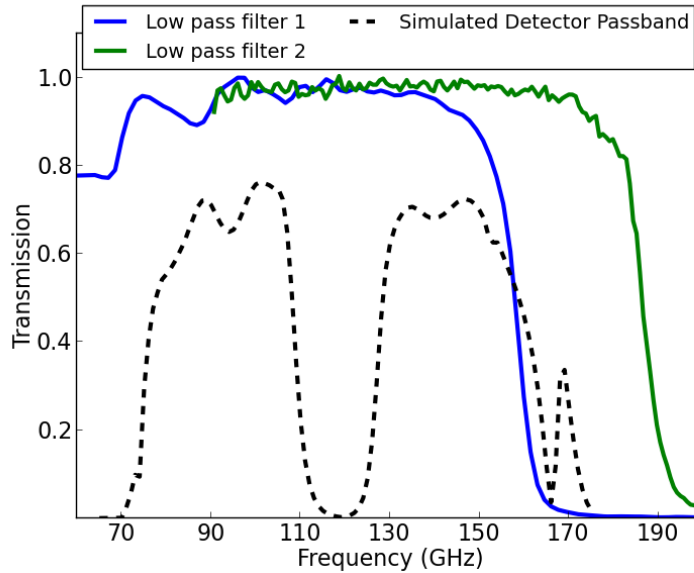


Figure 4.7: The PA3 simulated band pass and transmission of filters used during lab measurements. The band pass simulation is calculated by Rahul Datta. It includes predicted reflection and absorption of the signal in the OMT, signal lines and on-chip filters. The SiO_x dielectric on which the signal lines are fabricated is assumed to have a 0.005 loss tangent for the simulation.

of loss at our operating temperatures and signal frequencies to be very low. If the number of superconducting carriers in the niobium lines is lower than expected, for example due to magnetic impurities or stress in the niobium, the amount of loss may contribute a significant amount.

4.3.1 Lab measurements of FH4 optical efficiency

We measured the optical efficiency of the PA3 hex wafer FH4 in the lab using a cold load blackbody radiation source and copper machined feedhorns before deploying the PA3 array to Chile. We use a piece of aluminum with a pyramid texture cut into the surface to act as an anit-reflective coating, then coated with Eccosorb 110, as the cold load blackbody radiation source. It sits inside of the cryostat, loosely thermally coupled to the second pulse tube stage ($\sim 3.5\text{K}$), and two free-space low pass filters are placed between it (one on the second pulse tube stage and one on the $\sim 1\text{K}$ still

stage) and the detector wafer to minimize heating of the colder dilution refrigerator stages by high frequency, out-of-band radiation. The transmission functions of the filters are shown in Fig. 4.7.

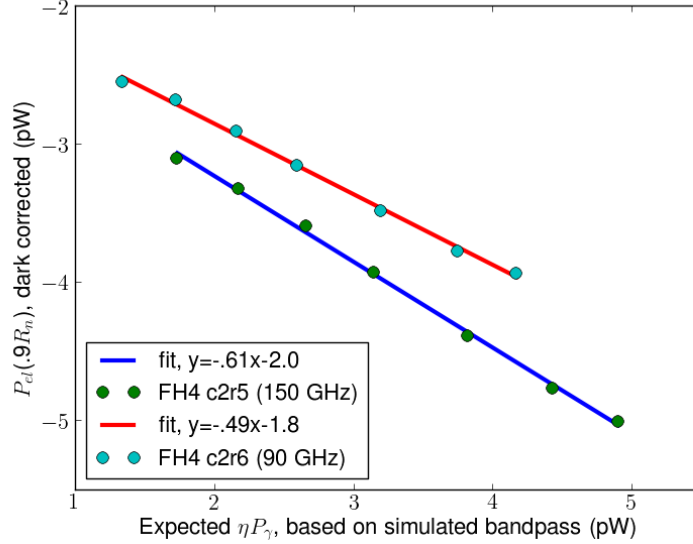


Figure 4.8: The dark-corrected $P_{bias}(0.9R_n)$ is plotted vs. the predicted detected power based on the simulated bandpass in Fig. 4.7.

We are able to heat the cold load to temperatures between 8 K and 20 K without overloading our cooling system. The cold load is an almost perfectly emissive blackbody, according to room temperature Vector Network Analyzer (VNA) measurements performed by Prof. Jeff McMahon, so we can know the exact radiation spectrum it emits when we heat it to a certain temperature. We define the optical efficiency, η , assuming the simulated 90 GHz and 150 GHz band passes shown in Fig. 4.7. (So if the detectors do have exactly the simulated 90 GHz and 150 GHz bandpass shown in Fig. 4.7, we would describe the measured optical efficiency as 100%.) To measure the optical efficiency, we set the cold load to a series of temperatures and measure $P_{bias}(0.9R_n)$ (by taking an IV curve) at each temperature, generating a data set following:

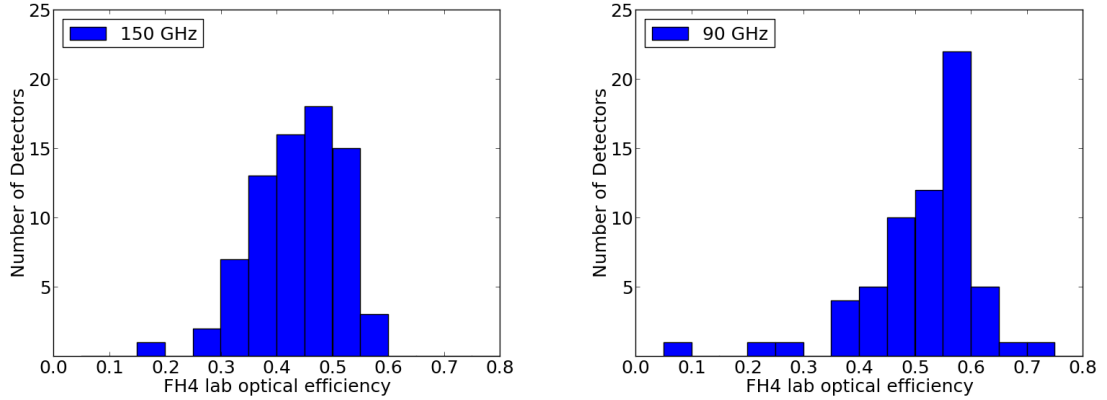


Figure 4.9: Histogram of FH4 detector optical efficiency values from lab measurements. *Left:* Results for FH4 150 GHz detectors. *Right:* Results for FH4 90 GHz detectors.

$$\eta P_\gamma + P_{bias}(0.9R_n) = \kappa(T(0.9R_n)^n - T_{bath}^n), \quad (4.7)$$

where P_γ is the expected amount of radiation detected based on the simulated bandpass. We calculate P_γ from the cold load temperature, the transmission functions of the low-pass filters used, and the simulated bandpass (shown in Fig. 4.7). As described earlier, $T(0.9R_n)$ is very close to constant, independent of bias current. If T_{bath} is held constant as the P_γ is varied by changing the cold load temperature, we can plot P_γ vs. $P_{bias}(0.9R_n)$ to fit for η :

$$\Delta(P_{bias}(0.9R_n)) = -\eta \Delta(P_\gamma)|_{T_{bath}}. \quad (4.8)$$

We keep the temperature of the copper hardware to which the wafer is heat sunk constant with a PID servo loop. However, the detector wafer T_{bath} still increases slightly with increasing cold load temperature. To measure changes in T_{bath} , we measure changes in $P_{bias}(0.9R_n)$ of the dark detector(s):

$$\Delta(T_{bath}^n) = -\Delta P_{bias,dark}(0.9R_n)/\kappa_{dark}. \quad (4.9)$$

Combining the above equations gives an expression for η when T_{bath} is changing:

$$-\eta\Delta(P_\gamma) = \Delta(P_{bias}(0.9R_n) - \kappa/\kappa_{dark}P_{bias,dark}(0.9R_n)). \quad (4.10)$$

As shown in Fig. 4.8, we plot $P_{bias}(0.9R_n) - \kappa/\kappa_{dark}P_{bias,dark}(0.9R_n)$, which we call the “dark-corrected” $P_{bias}(0.9R_n)$ vs. P_γ at a series of cold load temperatures. Then, we fit a line to find η , the negative of the line’s slope. The optical efficiency results are shown in Fig. 4.9.

4.3.2 Optical efficiencies on telescope, from atmosphere

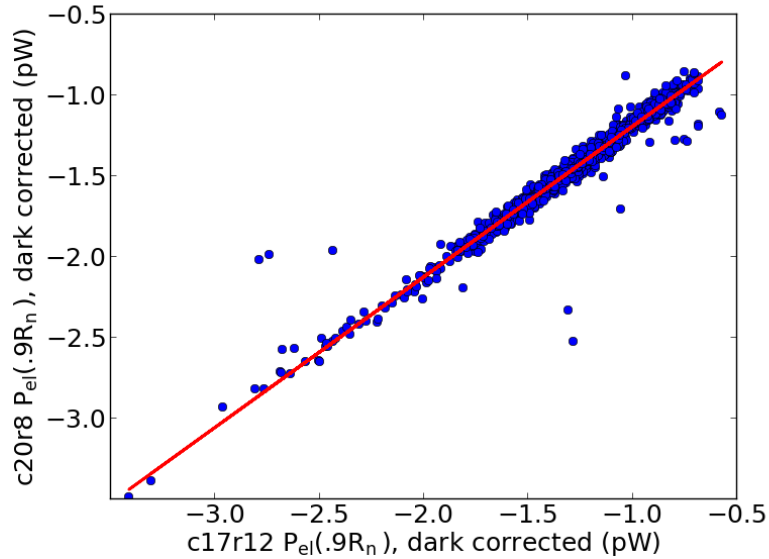


Figure 4.10: Example of relative optical efficiency calculation. The set of dark-corrected $P_{bias}(0.9R_n)$ from the Season 3 IVs for one detector is plotted vs. another. The slope of line fit to the data gives the ratio between the optical efficiencies of the two detectors.

Most of the photon power incident on the ACTPol detectors is due to emissions from oxygen and water molecules in the atmosphere. The loading conditions change with the weather, as the amount of precipitable water vapor (PWV) in the atmosphere changes, and with the telescope elevation. Therefore, we can calculate the

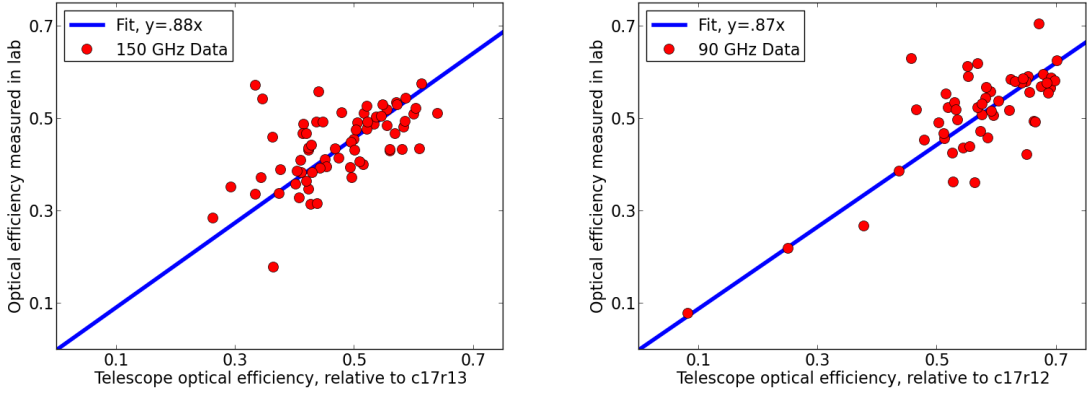


Figure 4.11: The lab optical efficiency measurement is plotted vs. the relative telescope optical efficiency for the FH4 detectors. *Left*: 150 GHz detectors. *Right*: 90 GHz detectors. A line is fit to the data with the intercept forced to zero. The slope of the line gives the conversion from the telescope relative optical efficiencies to absolute optical efficiencies.

optical efficiency on the telescope by measuring $P_{bias}(0.9R_n)$ at different elevations and weather conditions, like we did in the lab for different cold load temperatures.

To find the radiated power from the atmosphere, P_γ , at a given PWV and elevation, we need to know the spectrum of atmosphere emission at that PWV and the passband of each detector. The PWV is also difficult to determine exactly- our best estimate is data from the APEX site, about 10 km away. However, we can easily find the relative optical efficiencies of a pair of detectors from IVs at different atmosphere conditions without calculating P_γ .

Relative optical efficiencies

We take IV curves about once every hour in between CMB observations to re-bias the detectors. Because the PA3 array covers a small sky solid angle, it is a good assumption that each pixel in the array sees the same loading conditions when an IV curve is taken. After correcting for any changes in bath temperature with each wafer's dark detector(s), there is a linear relationship between one detector's set of $P_{bias}(0.9R_n)$ and another's, with the slope equal to the ratio of their optical efficiencies:

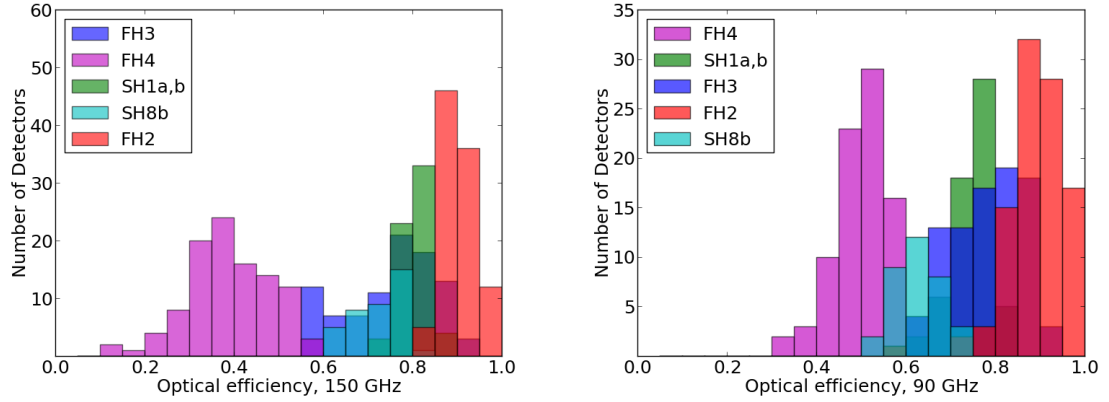


Figure 4.12: Telescope optical efficiency results from atmosphere loading, normalized with FH4 lab data. The optical efficiency is defined relative to the bandpass in Fig. 4.7.

$$\begin{aligned} \Delta(P_{bias1}(0.9R_n) - \kappa_1/\kappa_{dark1}P_{bias,dark1}(0.9R_n)) = \\ \eta_1/\eta_2\Delta(P_{bias2}(0.9R_n) - \kappa_2/\kappa_{dark2}P_{bias,dark2}(0.9R_n)) \end{aligned} \quad (4.11)$$

An example of the data fit to find the relative optical efficiencies between two detectors is shown in Fig. 4.10.

Normalization with FH4 lab data

To turn the relative optical efficiencies into absolute optical efficiencies, we use the FH4 lab data discussed in Sec. 4.3.1 as a normalization. We plot the optical efficiency values found in the lab vs. the relative optical efficiency found on the telescope for the detectors on FH4, as shown in Fig. 4.11, and fit a line with an intercept of zero to find the normalization scaling factor.

The normalized optical efficiency values for PA3 are shown in Fig. 4.12. The highest optical efficiencies are on the FH2 wafer, which almost match the optical efficiency predicted by the simulated bandpass. The optical efficiencies of detectors on FH4 are significantly lower than the optical efficiencies of detectors on other wafers.

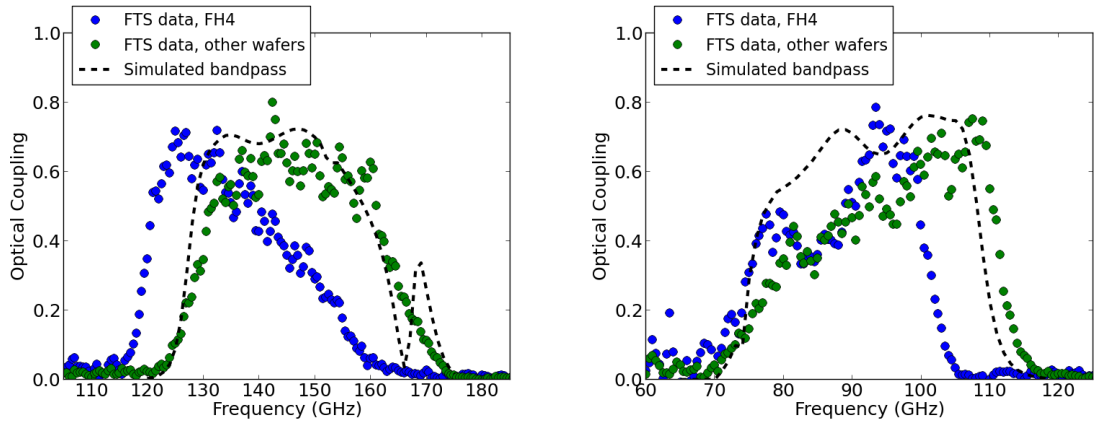


Figure 4.13: A comparison of the average FTS spectra for detectors on the FH4 wafer and detectors on other wafers in PA3. The normalization of the FTS data is arbitrary. Individual detector FTS spectra were measured by Rahul Datta.

The bandpass of the FH4 detectors is also shifted to lower frequencies relative to the other wafers, as shown in the FTS data taken by Rahul Datta in Fig. 4.13. The shift of the FH4 bandpass to lower frequency suggests the SiO_x index of refraction is higher on this wafer. (The lower edge of the 90 GHz band is not shifted because it is defined by the bandpass of the OMT.) The difference in the optical efficiency between detectors on the FH4 wafer and detectors on the rest of the wafers in the array is too large to be accounted for the bandpass shift alone. It is possible that there is some difference in the SiO_x dielectric on this wafer that makes both the index of refraction and the loss tangent higher, accounting for both the shift in the bandpass and the lower optical efficiency.

4.4 Conclusion

The PA3 detectors have P_{sat} values that work well for the ACT loading conditions. The detectors do not saturate at the normal operating bath temperature and atmosphere loading conditions. The P_{sat} s are uniform enough that groups of detectors on one bias line can also almost all be biased onto their transitions with one I_{bias} value.

The optical efficiency of the PA3 detectors is lower than expected on some wafers. However, the best PA3 detectors match the optical efficiency prediction.

Chapter 5

ACTPol TES $R(T, I)$ transitions

5.1 Introduction

The sharp transition in a TES's resistance as a function of temperature allows its use as a very sensitive resistive thermometer in the ACTPol TES bolometers. Although it would be simplest for detector use if the TES resistance were only a function of its temperature, the resistance of a superconducting film depends on the bias current and magnetic field as well. In this thesis, we consider only the effects of the temperature, the bias current, and the self-induced magnetic fields from the bias current on the TES resistance [87]. We consider outside magnetic fields to have a negligible effect due to magnetic field screening in the ACTPol cryostat.

Each TES has a unique $R(T, I)$ function. In general, the resistance always increases as the current or temperature is increased. To calculate the effect of the $R(T, I)$ transition shape on detector performance, it is most convenient to consider the dimensionless logarithmic partial derivatives of the function with respect to temperature and current, α and β :

$$\alpha \equiv \left. \frac{T}{R} \frac{\partial R}{\partial T} \right|_I, \beta \equiv \left. \frac{I}{R} \frac{\partial R}{\partial I} \right|_T. \quad (5.1)$$

In this chapter, we first describe physical models of the transition and measurements of the ACTPol $R(T, I)$ functions. Then, we discuss methods for improving the detector operation and calibration by taking into account the effects of the $R(T, I)$ transition shape.

5.2 Physical models of the TES $R(T, I)$ transition

In recent years, two models have been developed to successfully describe the TES $R(T, I)$ transition function: the two-fluid model and the RCSJ model [89]. In the RCSJ model, the TES is treated as a capacitively and resistively shunted weak link (Josephson junction) between its higher T_c electrodes. Detectors well-described by the RCSJ model have a critical current that depends exponentially on temperature and exhibit the Josephson junction signature oscillations in critical current as a function of magnetic field [78][79][55].

The RCSJ model generally applies to smaller TESes with electrodes with a T_c that is higher than the T_c of the TES, while the two-fluid model applies to larger TESes [13]. The ACTPol TESes and similar TESes made at NIST (similar in geometry and T_c of the TES and electrodes) have been shown to follow the two-fluid model and do not show weak link effects [74][89].

The two-fluid model is based on the Skocpol-Beasley-Tinkham (SBT) model, which describes the transition of Type-I superconducting films [50][13][85]. In the two-fluid model description of the TES transition, the TES current, I , is carried partly by normal electrons (I_n) and partly by superconducting electrons (I_{sc}):

$$I = I_n + I_{sc} = I_n + c_I I_{co} (1 - T/T_c)^{3/2}, \quad (5.2)$$

where the superconducting current is some fraction, c_I , of the Ginzburg-Landau (GL) critical current, $I_c(T) = I_{co}(1 - T/T_c)^{3/2}$. Because the superconducting current

is dissipationless, the voltage measured in the transition region is due only to the normal current. The resistance on the normal electrons is some fraction, c_R , of R_n , giving:

$$V = I_n c_R R_n, \quad (5.3)$$

$$R(T, I) = c_R R_n (1 - c_I I_{co} (1 - T/T_c)^{3/2} / I). \quad (5.4)$$

5.2.1 Comparison with Data

One way we have measured the $R(T, I)$ transitions of ACTPol TESes is by using our usual readout setup with the MCE and a low I_{bias} . At low I_{bias} , the TES temperature is approximately equal to the bath temperature, which can be measured with a nearby thermometer. We measured the $R(T, I)$ functions of a few detectors in this way, as shown in Fig. 5.1 for detector col B, row 26 on semihex 3A (a PA2 wafer not selected for final array). Here, $R(T, I)$ was measured under constant DC I_{bias} values of 2.8, 5.3, 9.1, 15.4, and 21.7 μA as a function of increasing and decreasing temperature sweeps of 0.04 mK/min. No hysteresis was observed in the three TESes measured; $R(T, I)$ curves from increasing and decreasing temperature sweeps match within the measurement error.

In the most general treatment of the two-fluid model, $c_I(T, I)$ and $c_R(T, I)$ are functions that may depend weakly on temperature and current. Here, we will follow Irwin et al [50] and, in a slight simplification to the SBT model, take c_R and c_I to be constants: $c_R = 1$ and $c_I = 1/2$. In this case, we only need to measure I_{co} , T_c , and R_n to make the two-fluid model prediction of $R(T, I)$.

We find the $I_c(T)$ function for the three PA2 detectors measured follows the GL prediction near T_c . This is consistent with the two-Fluid model, and not the RCSJ

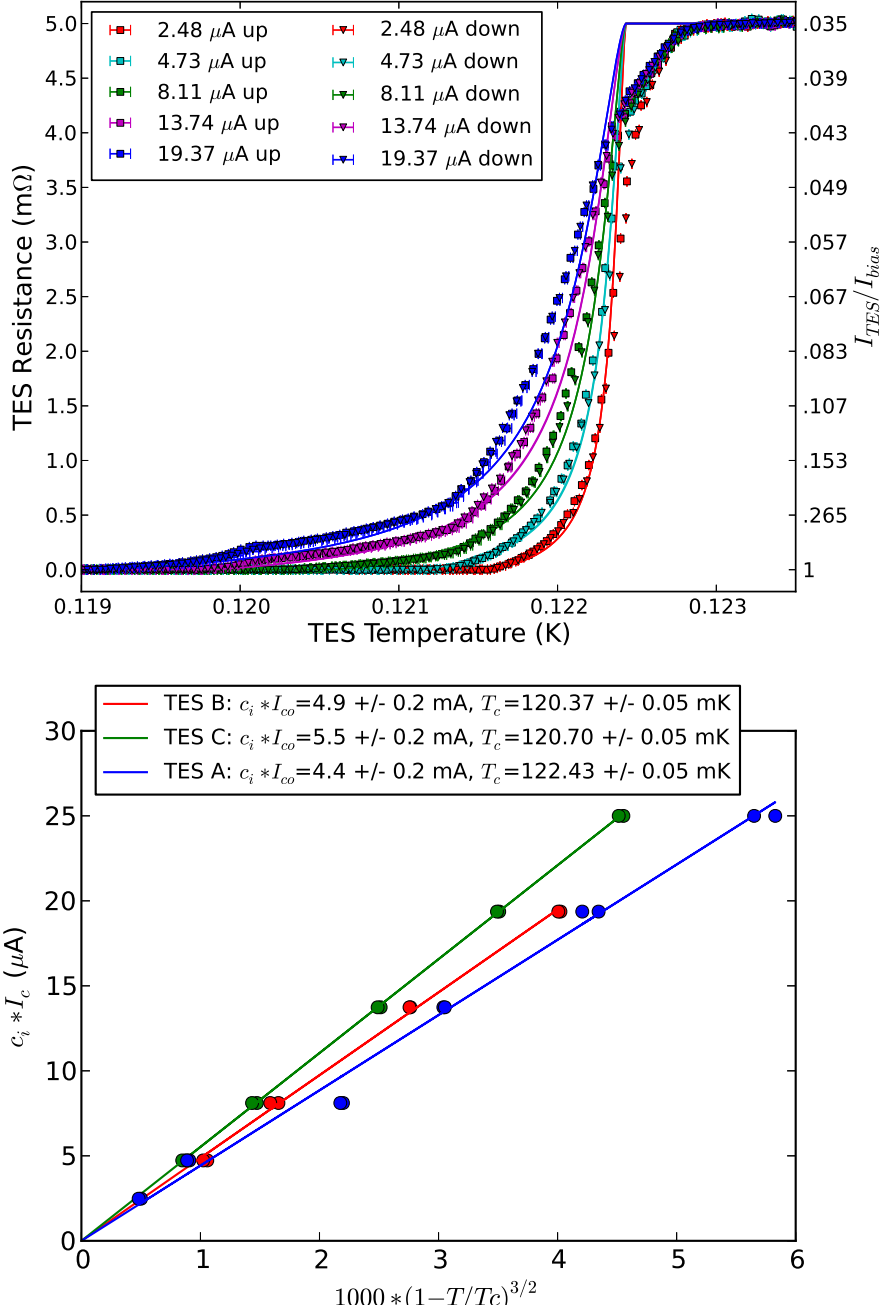


Figure 5.1: *Top*: $R(T, I)$ data for detector col B, row 26 on semihex 3A (a PA2 wafer not selected for final array) is taken at the constant DC I_{bias} values indicated in the legend. The TES resistance is measured as the temperature is swept either up or down (indicated in the legend) at a rate of 0.04 mK/min. Solid lines are the two-fluid model prediction using the measured R_n and the I_{co} and T_c from the GL fit to the $I_c(T)$ data on the right. *Bottom*: $I_c(T)$ data for three TESes on semihex 3A. The data follow the GL prediction, with the I_{co} and T_c fit values indicated in the legend.

model, which predicts an exponential dependence of the I_c on temperature. Using R_n measured from IV curves and I_{co} and T_c from the GL fit to the $I_c(T)$ data, we calculate the predicted $R(T, I)$ shape and over-plot with the $R(T, I)$ data in Fig. 5.1. There is qualitative agreement between the data and the curves from the two-fluid model up to about $80\%R_n$. The agreement is especially good for the curves at the lowest I_{bias} values, and starts to deviate at higher I_{bias} as the transition widens and slight anomalies in the $R(T)$ curve emerge.

Measuring the $R(T, I)$ function in this way, by assuming the TES temperature is equal to the bath temperature measured by a thermometer, is limited to dark measurements with very small bias currents, where heating of the TES island is minimal. We are of course most interested in the $R(T, I)$ transition function under typical TES operating conditions, when the bias current is large. In this case, the $R(T, I)$ function can still be measured if the thermal conductivity between the TES island and the bath is known.

In the section below, we describe a method for measuring the $R(T, I)$ function at typical operating bias currents using the set of IV curves taken during telescope observations.

5.3 Measurement of the $R(T, I)$ function from IV curves

We start by explicitly including the optical efficiency in Eq. 4.1:

$$P_{bias} + \eta P_\gamma = \kappa(T^n - T_{bath}^n). \quad (5.5)$$

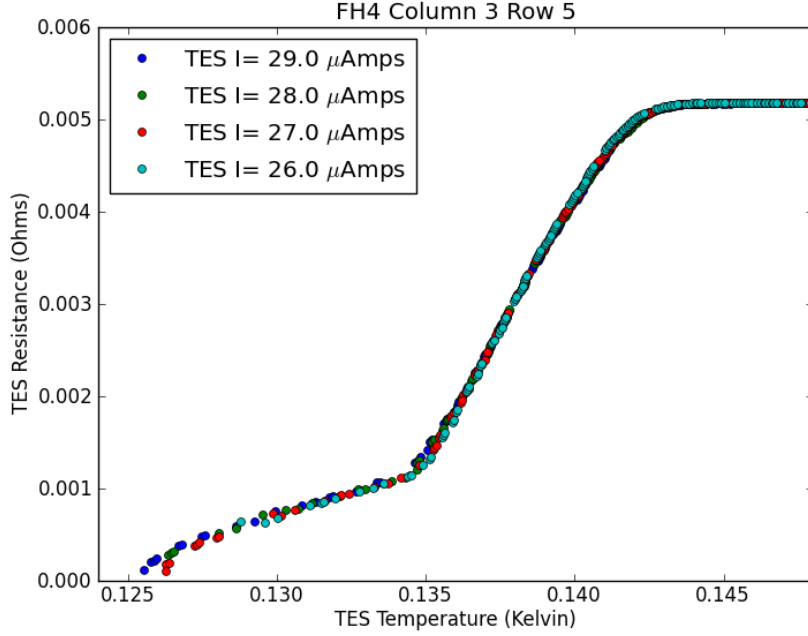


Figure 5.2: $R(T, I)$ function for an FH4 PA3 detector (col3 row4 ID131 in the PA3 array) measured in the lab by taking IV curves at different bath temperatures.

We can re-arrange this equation so that terms that do not depend on the TES state are on the left side, the sum of which we call $P_{loading}$, or P_l . The terms that depend on the TES state in response to P_l and I_{bias} are on the right side:

$$P_l \equiv \eta P_\gamma + \kappa T_{bath}^n = \kappa T^n - P_{bias}. \quad (5.6)$$

We can calculate P_l if κ , n , and T_c , which we define as the temperature at $.9R_n$, have been previously measured:

$$P_l = \kappa T_c^n - P_{bias}(0.9R_n). \quad (5.7)$$

The TES resistance, current, and P_{bias} can be calculated directly from the IV curve (see Chapter 2). For each point in each IV curve, we calculate the TES temperature using equations 5.6 and 5.7:

$$T = \left(\frac{P_l + P_{bias}}{\kappa} \right)^{1/n}. \quad (5.8)$$

For each detector, we collect the $R(T, I)$ points from all IV curves taken during 1-3 seasons of telescope observations (an IV curve is taken about once an hour during observations) into one large data set. This gives us the part of the detector's $R(T, I)$ surface accessible during telescope observing conditions. The $R(T, I)$ functions of two PA2 detectors are shown in Figures 5.4 and 5.5. Detector col 7 row 17, in Fig. 5.4 represent the group of ACTPol detectors with well-behaved $R(T, I)$ transitions. Detector col 11 row 0 is representative of the ACTPol detectors with what we call double transitions, or strong kinks in their $R(T, I)$ curves. We will use these two example detectors to show the role of the $R(T, I)$ transition in detector operation and calibration both in the case when non-linearities in the $R(T, I)$ transition are present and when they are not.

5.4 Detector Responsivity

During CMB observations, we effectively voltage-bias the TES by applying a constant bias current, I_{bias} , to the TES in parallel with a shunt resistor (see Chapter 2). As we scan the telescope across the sky, the amount of external loading on the TES island, which we will call P_l , fluctuates:

$$P_l = \kappa T_{bath}^n + \eta P_\gamma = \kappa T^n - P_{bias} = \kappa T^n - R_{sh} I (I_{bias} - I). \quad (5.9)$$

By measuring changes in the current through the TES at a given I_{bias} , we can determine changes in the amount of P_l on the TES island. The responsivity, $Resp$, gives us a transformation function from changes in TES current to changes in P_l :

$$Resp(I_{bias}, R) = \left. \frac{\Delta P_l}{\Delta I} \right|_{I_{bias}} \quad (5.10)$$

Note that by measuring changes in P_l , we measure a contribution from fluctuations in P_γ (which we would like to measure) but we also measure a contribution from fluctuations in T_{bath} (which create a spurious signal). In Chapter 6 of this thesis, we discuss how the signal due to bath temperature fluctuations can be isolated using dark detectors, which are TES bolometers that are not coupled to the sky signal, in the ACTPol detector arrays.

Note also that we can only determine P_l by measuring I at constant I_{bias} if the function $P_l(I)|_{I_{bias}}$ is single-valued. This is true if the (reciprocal of the) responsivity is either always positive or always negative, which we will see later is the case.

In the sections below, we describe methods for measuring the responsivity and how the $R(T, I)$ function affects the responsivity. First, we will describe measurements of the responsivity function as a function of I_{bias} and TES resistance. Then, we will discuss how to measure the TES resistance in order to calculate the responsivity for some data set.

5.4.1 Responsivity as a function of I_{bias} and TES resistance

To derive an expression for the responsivity, we start with Eq. 5.7, and write it in the differential form:

$$\Delta P_l|_{I_{bias}} = \kappa n T^{n-1} \Delta T|_{I_{bias}} - \Delta P_{bias}|_{I_{bias}}. \quad (5.11)$$

This gives the following expression for the responsivity:

$$Resp = \left. \frac{\Delta P_l}{\Delta I} \right|_{I_{bias}} = \kappa n T^{n-1} \left. \frac{\Delta T}{\Delta I} \right|_{I_{bias}} - \left. \frac{\Delta P_{bias}}{\Delta I} \right|_{I_{bias}}. \quad (5.12)$$

If the first term, $\kappa n T^{n-1} \frac{\Delta T}{\Delta I} \Big|_{I_{bias}}$, is small enough compared to the second term, $-\frac{\Delta P_{bias}}{\Delta I} \Big|_{I_{bias}}$, that it can be neglected, then we have:

$$(Resp)_{approx} = -\frac{\Delta P_{bias}}{\Delta I} \Big|_{I_{bias}} \quad (5.13)$$

In this case, the responsivity only depends on I_{bias} and the bias point, or $\%R_n$ of the TES:

$$(Resp)_{approx} = -r_{sh} I_{bias} \left(\frac{R/r_{sh} - 1}{R/r_{sh} + 1} \right) \quad (5.14)$$

Now, we will quantify the first term, $\kappa n T^{n-1} \frac{\Delta T}{\Delta I} \Big|_{I_{bias}}$, to calculate the responsivity exactly and see when the expression above is a good approximation. In our bias configuration, if the applied I_{bias} is known (which it always should be), the TES current, voltage, and resistance are all known if the TES current is measured:

$$V = r_{sh}(I_{bias} - I), \quad (5.15)$$

$$R = r_{sh}(I_{bias}/I - 1). \quad (5.16)$$

Because we cannot measure ΔT directly, we write it in terms of quantities we can measure: ΔI , ΔR , α , and β :

$$\Delta R = \beta \frac{R}{I} \Delta I + \alpha \frac{R}{T} \Delta T, \quad (5.17)$$

$$\Delta T = \frac{T}{R\alpha} \left(\Delta R - \beta \frac{R}{I} \Delta I \right). \quad (5.18)$$

Eq. 5.16 in its differential form is:

$$\Delta R = r_{sh} \left(\frac{\Delta I_{bias}}{I} - \frac{I_{bias} \Delta I}{I^2} \right). \quad (5.19)$$

Combining the above equations gives an expression for ΔT in terms of ΔI and ΔI_{bias} :

$$\Delta T = \frac{T}{I\alpha(I_{bias}/I - 1)} (\Delta I_{bias} - \Delta I(I_{bias}/I(\beta + 1) - \beta)), \quad (5.20)$$

Under constant I_{bias} , as is the case during CMB observations, we restrict the TES state to a one-dimensional curve on the two-dimensional $R(T, I)$ surface. We have the following relationship between ΔT and ΔI :

$$\Delta T|_{I_{bias}} = -\frac{T}{\alpha} \left(\frac{r_{sh} I_{bias}}{P_{bias}} + \frac{\beta}{I} \right) \Delta I|_{I_{bias}}. \quad (5.21)$$

Combining the above equations we have the following expression for the responsivity:

$$\left. \frac{\Delta P_l}{\Delta I} \right|_{I_{bias}} = -r_{sh} I_{bias} \left(\frac{1}{L} \left(1 + \beta \left(\frac{R/r_{sh}}{1 + R/r_{sh}} \right) \right) + \frac{R/r_{sh} - 1}{R/r_{sh} + 1} \right), \quad (5.22)$$

where the L is the loop gain defined by Irwin and Hilton [51]:

$$L = \frac{P_{bias}\alpha}{GT} = \frac{P_{bias}\alpha}{n\kappa T^{n-1}} = \frac{P_{bias}\alpha}{n(P_l + P_{bias})}. \quad (5.23)$$

Note that the responsivity is always negative because α and β are both always positive and we always bias the detector such that $R > r_{sh}$. This ensures that the function $P_l(I)|_{I_{bias}}$ is single-valued. In the expression for the responsivity above, the term on the left is the contribution for a non-zero ΔT . We see that this term can be neglected when:

$$\frac{R/r_{sh} - 1}{R/r_{sh} + 1} \gg \frac{1}{L} \left(1 + \beta \left(\frac{R/r_{sh}}{1 + R/r_{sh}} \right) \right) \quad (5.24)$$

In the ACTPol analysis, we currently use the approximate function, Eq. 5.14, to calculate the responsivity. This is a convenient approach because to calculate the responsivity from this equation, we only need to know the I_{bias} applied to the TES and measure the TES resistance.

However, the magnitude of the responsivity calculated from Eq. 5.14 will always be smaller than the actual value (if α and β are always positive.). If one operates the TES under conditions when the loop gain is not very high, the above condition may not be met and Eq. 5.14 may not be accurate.

We will see later that as P_l increases and the loop gain decreases, the responsivity deviates more and more from the simple expression we currently use. There are also some ACTPol TESes with large non-linearities in some transition regions. Near these kinks in the transition, the responsivity function becomes quite complex.

Measuring the responsivity function

In this section, we describe a method for measuring each detector's exact responsivity function. As shown in Eq. 5.7, P_l can be calculated from P_{bias} if the detector properties κ , n , and T_c have been previously measured. However, we can measure changes in P_l without needing to know κ , n , and T_c :

$$\Delta P_l = -\Delta P_{bias}(0.9R_n). \quad (5.25)$$

In the above equation, we are assuming, as in Chapter 4, that β is negligible at $90\%R_n$ and $T(0.9R_n)$ can be taken as constant. To calculate the responsivity, we are interested in how much the TES current changes under constant I_{bias} when P_l changes. Using the set of IV curves taken over the ACTPol observations, we can plot

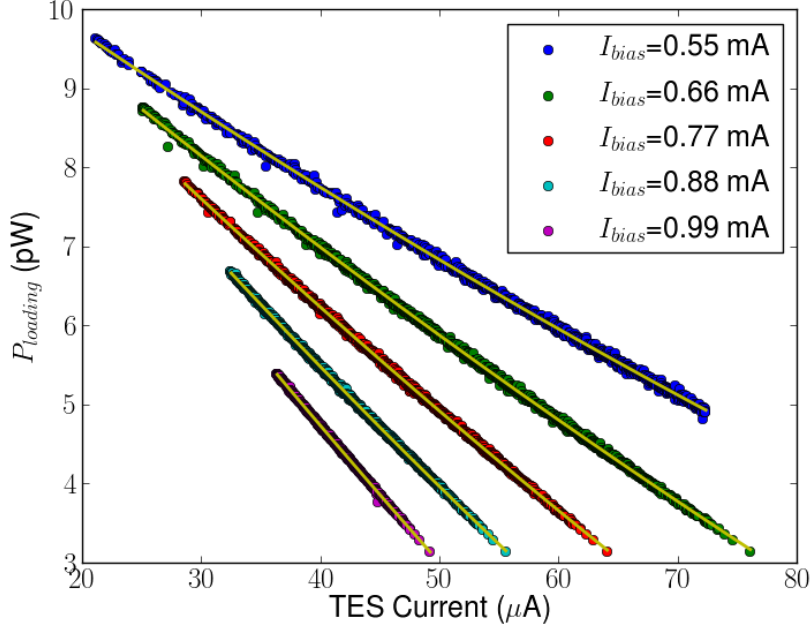


Figure 5.3: An example of P_l vs. I data used to calculate the responsivity function. This data is for detector col7row17. Quadratic fits to the data at constant I_{bias} are shown in yellow.

$-P_{bias}(0.9R_n)$ vs. I at constant I_{bias} as shown in Figures 5.4 and 5.5. The slope of a line fit to this data gives the responsivity:

$$Resp = \left. \frac{\Delta P_l}{\Delta I} \right|_{I_{bias}} = - \left. \frac{\Delta P_{bias}(0.9R_n)}{\Delta I} \right|_{I_{bias}} \quad (5.26)$$

For the set of PA2 detectors that have smooth $R(T, I)$ functions, which we will from now on call the fiducial detectors, we plot $-P_{bias}(0.9R_n)$ vs. I at constant I_{bias} , as shown in Fig. 5.9, and fit a quadratic function to the data. The slope of this function gives us the responsivity as a function of I_{bias} and I . Because the TES resistance is completely defined by I_{bias} and I , we can easily convert this into the responsivity as a function of I_{bias} and R . For the fiducial detectors, we will now only need to compute the TES resistance, as described below, to calculate the responsivity for each data set.

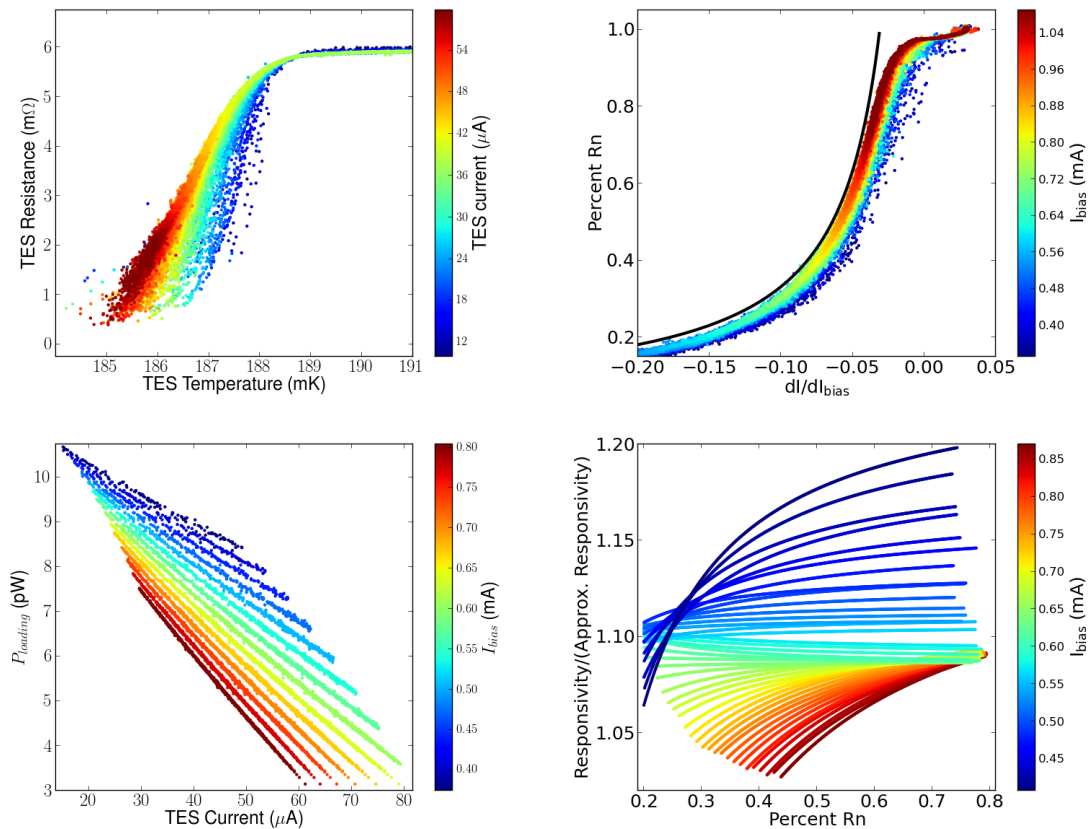


Figure 5.4: Various data for PA2 detector col7 row17 ID551 (on hex wafer FHC3) from analysis of the set of Season 2 IV curves. *Upper Left*: $R(T, I)$ curve *Upper Right*: $\%R_n$ vs. bias step slope at various I_{bias} values *Lower Left*: P_l vs. TES current at various I_{bias} values *Lower Right*: Ratio of Actual responsivity: Approximate Responsivity vs. $\%R_n$ at various I_{bias} values

For the detectors with kinks in the $R(T, I)$ function, the $-P_{bias}(0.9R_n)$ vs. I data is more complicated. In Fig. 5.5, we compute the responsivity pointwise by fitting a line to the local $-P_{bias}(0.9R_n)$ vs. I data. The result is shown in the lower right plot in Fig. 5.5.

ACTPol detector responsivity functions

Plots of the ratio of the actual responsivity the approximate responsivity as a function of $\%R_n$ and I_{bias} are shown for our PA2 detector representative of well-behaved $R(T, I)$ transitions in Figure 5.4 and for our representative of a detector with strong

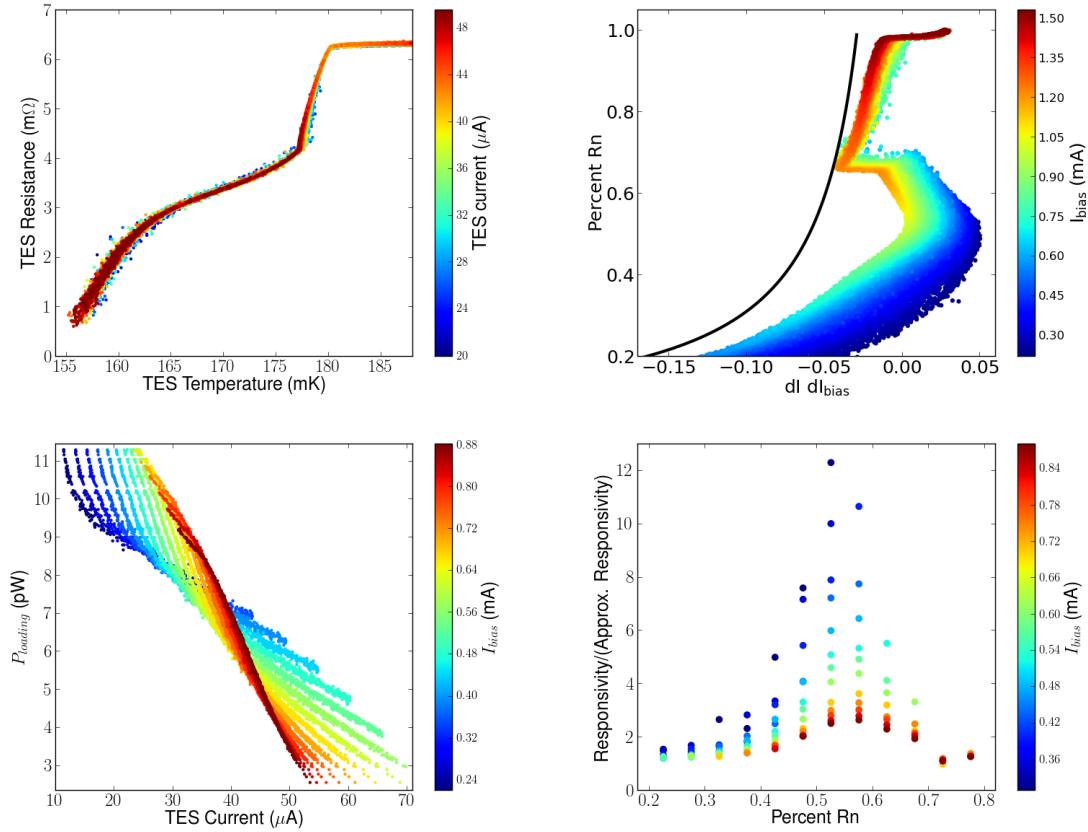


Figure 5.5: Various data for PA2 detector col11 row0 ID11 (on hex wafer FHC1) from analysis of the set of Season 2 IV curves. *Upper Left*: $R(T, I)$ curve *Upper Right*: $\%R_n$ vs. bias step slope at various I_{bias} values *Lower Left*: P_l vs. TES current at various I_{bias} values *Lower Right*: Ratio of Actual responsivity: Approximate Responsivity vs. $\%R_n$ at various I_{bias} values

non-linearities in the $R(T, I)$ transition in Figure 5.5. The actual responsivity deviates more from the approximation with increasing P_l (with decreasing I_{bias} at constant $\%R_n$) because the loop gain is decreasing. For the well-behaved detector, the deviation is 0-20% depending on I_{bias} and $\%R_n$.

For the double-transition detector, the deviation of the responsivity from the approximation depends strongly on $\%R_n$. This is due to the strong dependence of α (which the loop gain is proportional to) on $\%R_n$. We would need to measure the $\%R_n$ for these detectors very accurately to determine their responsivity from this function.

5.4.2 Measuring $\%R_n$ with bias steps

To measure the $\%R_n$ to which each detector is biased, we take what we call a bias step [73]. Taking an IV curve would be the most straightforward way to measure the $\%R_n$. However, IV curves take about 1-2 minutes to measure. The IV curve also heats the detector array, and it takes about 5 minutes to cool back to its usual operating bath temperature afterwards. The bias steps only take a few seconds.

To take a bias step, we step I_{bias} by a small amount, 50 DAC counts (about 11 μA) from its current value, and the amplitude of the corresponding step in TES current is measured. Because we do not have a way of measuring the I_{fb} offset for bias steps, as we do for IV curves by fitting the normal branch, we can only measure changes in the TES current during a bias step and not the absolute TES current value. Therefore, we cannot directly measure the TES resistance with a bias step. We need an expression for the resistance as a function of the I vs. I_{bias} slope and the I_{bias} value: $R(dI/dI_{bias}|_{P_l}, I_{bias})$.

To derive an expression for $R(dI/dI_{bias}|_{P_l}, I_{bias})$ in terms of our usual detector parameters, we start again with the differential form of Eq. 5.7. During a bias step or IV curve, we assume the P_l conditions are constant, so we have:

$$\Delta(P_{bias})|_{P_l} = \kappa \Delta(T^n)|_{P_l} \quad (5.27)$$

$$r_{sh}(I \Delta I_{bias}|_{P_l} + \Delta I|_{P_l} (I_{bias} - 2I)) = \kappa n T^{n-1} \Delta T|_{P_l} \quad (5.28)$$

If $\kappa n T^{n-1} \Delta T$ is small enough compared to the other terms to be neglected, the above equation reduces to:

$$\left(\frac{\Delta I}{\Delta I_{bias}} \Big|_{P_l} \right)_{approx} = \frac{1}{2 - I_{bias}/I} = \frac{1}{1 - R/r_{sh}}. \quad (5.29)$$

To find the exact expression for $dI/dI_{bias}|_{P_l}$, we can write ΔT in Eq. 5.28 in terms of ΔI and ΔI_{bias} using Eq. 5.20, giving us:

$$\left. \frac{\Delta I}{\Delta I_{bias}} \right|_{P_l} = \frac{1 - 1/L}{1 - R/r_{sh} - 1/L(1 + R/r_{sh}(1 + \beta))}. \quad (5.30)$$

If we solve for the TES resistance in Eq. 5.29, we have the following approximation for the TES resistance in terms of I_{bias} and the measured $\Delta I/\Delta I_{bias}$ value:

$$R_{approx} = r_{sh} \left(1 - \left(\left. \frac{\Delta I}{\Delta I_{bias}} \right|_{P_l} \right)^{-1} \right) \quad (5.31)$$

While Eq. 5.30 gives the exact expression for the TES resistance:

$$R_{exact} = r_{sh} \left(1 - \left(\left. \frac{\Delta I}{\Delta I_{bias}} \right|_{P_l} \right)^{-1} \right) \frac{L - 1}{1 + \beta + L} \quad (5.32)$$

So, the approximate expression, Eq. 5.31, always gives a TES resistance higher than the actual value, Eq. 5.32. (This is true as long as $\beta > -2$, and we assume β is always positive.) In the limit of infinite loop gain, assuming finite β , the approximation and the exact function give the same value for R .

Currently, in the ACTPol analysis, as in the case of the responsivity, we assume the ΔT term in Eq. 5.28 is small enough to be neglected and use Eq. 5.31 to calculate the TES resistance from the bias step amplitude. In the sections below, we discuss measurements of the ACTPol detector $R(dI/dI_{bias}|_{P_l}, I_{bias})$ functions. For some detectors, at some parts of their transitions, the $R(dI/dI_{bias}|_{P_l}, I_{bias})$ function is close to Eq. 5.31. At other parts of the transition, the approximation may deviate strongly from the exact expression. For other detectors, the function not only doesn't follow a simple approximation but is not well defined- there are multiple resistance values at a given I_{bias} with the same I vs. I_{bias} slope.

Measuring $R(dI/dI_{bias}|_{P_l}, I_{bias})$

To measure the $R(dI/dI_{bias}|_{P_l}, I_{bias})$ function, we again use the set of IV curves taken during telescope observations. For each IV curve, we measure $dI/dI_{bias}|_{P_l}$ and R at each I_{bias} value. Then, we combine the data from all the IV curves into one data set, as shown in Figures 5.4 and 5.5.

As shown in Fig. 5.6, we then fit a quadratic function to the data set of R vs. $1/(dI/dI_{bias}|_{P_l})$ at each I_{bias} value. (If the function $R(dI/dI_{bias}|_{P_l}, I_{bias})$ followed the Eq. 5.29 exactly, there would be a linear relationship between R and $1/(dI/dI_{bias}|_{P_l})$ at constant I_{bias} .) This function can be used to calculate R from a bias step measurement of $dI/dI_{bias}|_{P_l}$.

ACTPol detector $R(dI/dI_{bias}|_{P_l}, I_{bias})$ functions

For the well-behaved detector in Fig. 5.4, the function $R(dI/dI_{bias}|_{P_l}, I_{bias})$ mostly follows the approximation function, with a slight offset. The actual function deviates strongly from the approximation at high $\%R_n$, where α and therefore the loop gain is low. The agreement in the range of 20%-80% R_n , where we will usually bias the detectors, is better at higher I_{bias} , when P_l is smaller and P_{bias} is larger.

In the case of the double-transition detector in Fig. 5.5, the function $R(dI/dI_{bias})|_{I_{bias}}$ is not single-valued, so the TES resistance cannot be determined from a bias step at one I_{bias} value alone. It may be possible to determine the resistance if bias steps are taken at multiple I_{bias} values. Or, if we for example take bias steps often enough to measure the drift, we may know the general $\%R_n$ vicinity in which the detector should be and be able to discern between the different options.

5.5 Responsivity measurement accuracy

In this section, we discuss the accuracy of the responsivity calculated from the bias step amplitude both in the case when the approximate $R(dI/dI_{bias}|_{P_l}, I_{bias})$ and $Resp(I_{bias}, R)$ functions, Eq. 5.29 and Eq. 5.14, are used and when the exact versions calculated from the IV curve set are used.

To calculate the responsivity, we first calculate the TES resistance from the $R(dI/dI_{bias}|_{P_l}, I_{bias})$ function and the bias step amplitude, then plug it into the $Resp(I_{bias}, R)$ function to calculate the responsivity. In the sections below, we will first discuss how accurately we can determine the TES resistance from the bias step amplitude and both the measured and approximate $R(dI/dI_{bias}|_{P_l}, I_{bias})$ functions. Then, we will discuss how well the approximate and measured $Resp(I_{bias}, R)$ functions agree. We will also quantify how error in the TES resistance calculation propagates to error in the responsivity calculation.

5.5.1 Bias step resistance measurement accuracy

In this section, we explore how well we can calculate a detector's TES resistance using the bias step amplitude and both the measured and approximate $R(dI/dI_{bias}|_{P_l}, I_{bias})$ function. For the fiducial detectors, because the $R(T, I)$ curve is smooth, the measured $R(dI/dI_{bias}|_{P_l}, I_{bias})$ function is single-valued everywhere.

To estimate the precision with which we can determine R from the $R(dI/dI_{bias}|_{P_l}, I_{bias})$ function and the bias step amplitude, we use the set of IV curves from Season 2 observations. With an IV curve, we can measure at any point R and the slope $dI/dI_{bias}|_{P_l}$. We can then take the slope, $dI/dI_{bias}|_{P_l}$, and measured $R(dI/dI_{bias}|_{P_l}, I_{bias})$ function and calculate R . By comparing the R value calculated directly from the IV curve

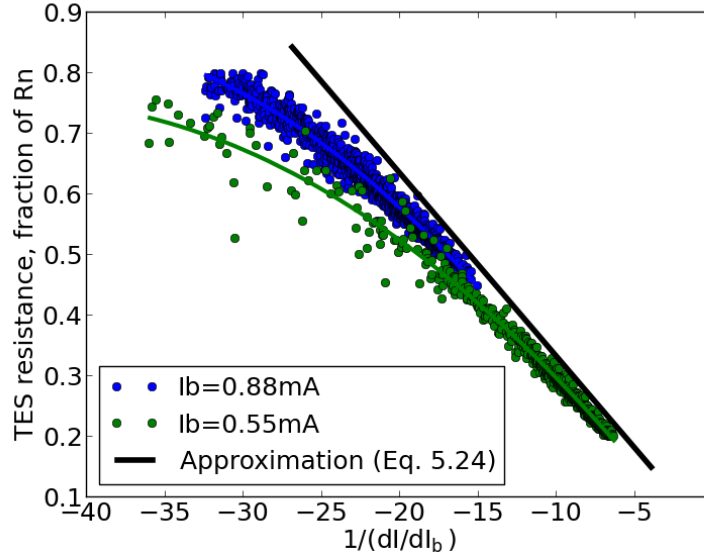


Figure 5.6: An example of the data from the set of Season 2 IV curves fit to find the $R(dI/dI_{bias}|_{P_1}, I_{bias})$ function. For PA2 detector col 7 row 17, TES resistance (in units of fraction of R_n) is plotted vs. $1/(dI/dI_{bias})$. For each I_{bias} , we fit a quadratic function to the data and store this as the $R(dI/dI_{bias})$ function at that I_{bias} value. When the approximate bias step function, Eq. 5.29 applies, there is a linear relationship between the resistance and the reciprocal of the I vs. I_{bias} slope, shown by the black line in this figure. The data deviates most from the approximation at higher $\%R_n$.

and the R value calculated from the $dI/dI_{bias}|_{P_1}$ slope, we can see how precisely the resistance can be calculated from the bias step.¹

In Fig. 5.7, the precision with which we can determine R from the bias step amplitude is shown for this set of fiducial detectors. The median error in the R calculation over the set of Season 2 IV curves is shown for each detector at 25%, 50%, and 75% R_n . In the histograms on the left, the measured $R(dI/dI_{bias}|_{P_1}, I_{bias})$ function is used to calculate R . In the histograms on the right, the approximation

¹One could argue that this isn't much of a test of how well the $R(dI/dI_{bias}|_{P_1}, I_{bias})$ function works because we calculated this function from the IV curves. While this is true, we do not have other data for testing the measured $R(dI/dI_{bias}|_{P_1}, I_{bias})$ function because the IV curve is the only way to measure both the TES R and $dI/dI_{bias}|_{P_1}$. The test is essentially a measure of how much scatter/error there is in the measured $dI/dI_{bias}|_{P_1}$ at a given R and I_{bias} value. It is also a test of how good our assumption is that a quadratic function can be fit to the R vs. dI_{bias}/dI at constant I_{bias} data.

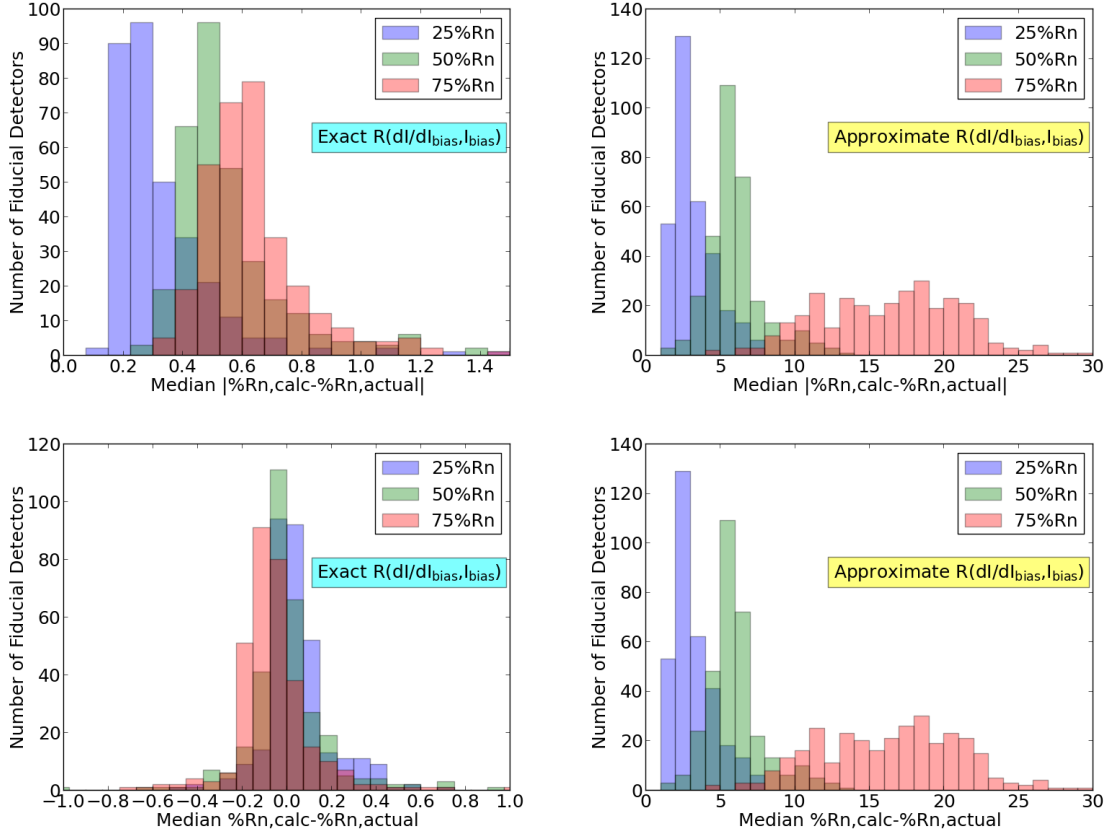


Figure 5.7: Here, we use the set of Season 2 IV curves to simulate how well the TES resistance can be calculated from the bias step amplitude using the $R(dI/dI_{bias}|P_l, I_{bias})$ function. For each IV curve, the slope $dI/dI_{bias}|_{P_l}$ at 25%, 50%, and 75% R_n is calculated. Then, we use the function $R(dI/dI_{bias}|P_l, I_{bias})$ to calculate $\%R_n$ from the IV curve slope, and compare to actual value. For each fiducial detector in PA2, the median $\%R_n$ error in this calculation over the Season 2 IVs is shown in the histograms above. In the *upper* histograms, the absolute value of the median is taken before the median to show the amplitude of the error. In the *lower* histograms, we do not take the absolute value before averaging, to show any tendency to calculate $\%R_n$ values higher or lower than the actual value. For the histograms on the *left* side, the $\%R_n$ is calculated using the exact $R(dI/dI_{bias}|P_l, I_{bias})$ functions calculated from the IV curve data, as in Fig. 5.6. The data shown in the histograms on the *right* side is calculated using the approximation of $R(dI/dI_{bias}|P_l, I_{bias})$ function, Eq. 5.29. There are 10 points higher than 30% not shown in the *upper right* and *lower right* plots, 7 data points larger than 1.5% not shown in the *upper left* plot, and 6 data points below -1.% and 8 data points above 1.% not shown in the *lower left* plot.

Eq. 5.29 is used. In the top histograms, the absolute value of the $\%R_n$ is taken before taking the median over the set of IVs. In the bottom histograms, we do not take the absolute value before averaging, to see if there is a tendency to predict a higher or lower $\%R_n$ than the actual value.

Using the measured $R(dI/dI_{bias}|P_l, I_{bias})$ function, the median $|\%R_{n,actual} - \%R_{n,calc}|$ is less than 1.5 $\%R_n$ at 25%, 50%, and 75% R_n for 98% of the fiducial detectors. The error in the R calculation is mainly due to scatter in the IV curve slope measurement at a given value of R , as shown in Fig. 5.6. It is about as likely that we will measure a $\%R_n$ higher than the actual value as it is to measure a $\%R_n$ lower than the actual value, as shown in the lower left plot of Fig. 5.6.

When the approximation Eq. 5.29 is used, the error is dominated by deviations of the actual $R(dI/dI_{bias}|P_l, I_{bias})$ function from the approximation. The TES resistance is universally overestimated when Eq. 5.29 is used, as shown in Eq. 5.29 and Eq. 5.29. For this reason, the median $\%R_n$ error is about the same as the median of the absolute value of the $\%R_n$ error. As shown in Fig. 5.6, the deviation of the $R(dI/dI_{bias}|P_l, I_{bias})$ function from the approximation is larger at higher $\%R_n$ and lower I_{bias} values. The deviation is so large at 75% R_n that the median error in R calculated from Eq. 5.29 over the fiducial detectors is about 15-20%.

5.5.2 Responsivity function accuracy

The responsivity is a function of the TES resistance and the I_{bias} value. To calculate the responsivity, we first measure the TES resistance from the bias step amplitude as discussed above. Then, we put this value into the responsivity function. We can use either the exact (measured) function or the approximate function for both calculations, which gives us four different responsivity calculation methods listed in the table below.

Table 5.1: Responsivity calculation method definitions

Resp. calc. method	$R(dI/dI_{bias} _{P_i}, I_{bias})$ func. used	$Resp(R, I_{bias})$ func. used
Exact	Exact/measured	Exact/measured
Approximation A	Exact/measured	Approximate (Eq. 5.14)
Approximation B	Approximate (Eq. 5.31)	Exact/measured
Approximation C	Approximate (Eq. 5.31)	Approximate (Eq. 5.14)

As discussed in Sec. 5.4.1, for a given R and I_{bias} , the approximate responsivity function always gives a responsivity smaller in magnitude than the exact function, Eq. 5.22, does. To see how large this effect is, we can compare the responsivity calculated by Approximation A to the responsivity calculated by the Exact method under typical operating conditions.

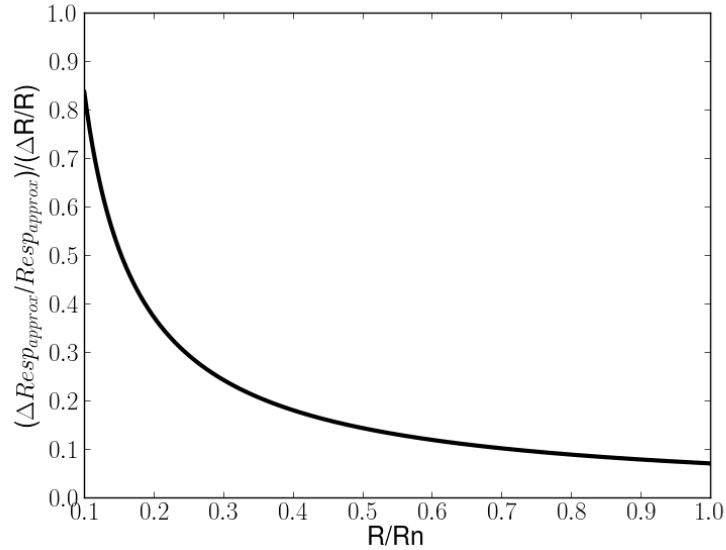


Figure 5.8: A plot of Eq. 5.33. This shows the propagation of error in the TES resistance measurement to error in the approximate responsivity.

We measure the detector response to a passing planet, usually Uranus, to calibrate the detectors. The peak height of the detector signal pulse in DAC counts due to the passing planet is converted to pW with the responsivity. In Fig. 5.9, the

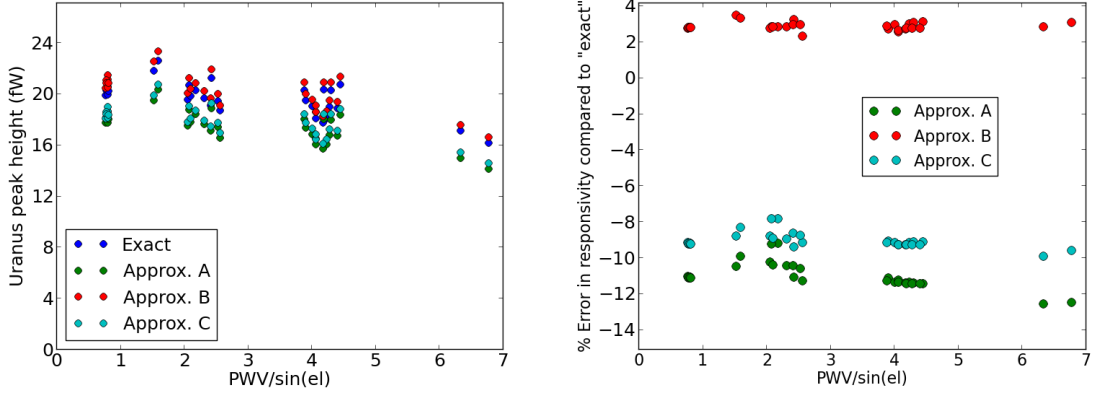


Figure 5.9: *Left*: Uranus peak heights vs. loading for an example PA2 detector, col 19 row 3. The responsivity used to convert the Uranus peak height in FB DAC counts to pW is calculated from the bias step amplitude and I_{bias} by four different methods defined in Table 5.1.

Uranus peak height calculated with each of the four different responsivity methods is shown for an example PA2 fiducial detector. For this detector, Approximation A predicts a responsivity 8%-10% smaller in magnitude than the Exact method. In the Fig. 5.10 histogram, the median difference between the responsivity calculated from Approximation A and the Exact method over the Season 2 Uranus observations is shown for each detector. The median value over the fiducial detectors is -8%.

In the ACTPol analysis, we currently use the Approximation C method to calculate the responsivity: we use both the approximate responsivity function, Eq. 5.14 and the approximate $R(dI/dI_{bias}|_{P_l}, I_{bias})$ function (Eq. 5.31). Although it uses a less accurate measure of the TES resistance, this method actually gives a responsivity closer to the exact value than Approximation A does. This is because the approximate $R(dI/dI_{bias}|_{P_l}, I_{bias})$ function always overestimates the TES resistance (see above), and the approximate responsivity function monotonically increases with increasing resistance:

$$\left. \frac{d|Resp_{approx}|}{dR} \right|_{I_{bias}} = \frac{2I_{bias}}{(R/r_{sh} + 1)^2} > 0. \quad (5.33)$$

Thus, Approximation C predicts a responsivity larger in magnitude and closer to the actual value than Approximation A. The approximate responsivity is actually not very sensitive to the TES resistance value. So, even though the approximate $R(dI/dI_{bias}|P_i, I_{bias})$ function gives a TES resistance much larger than the actual value, this has a relatively small effect on the approximate responsivity value: the median difference between the Approximation A and Approximation C values shown in Fig. 5.10 over the fiducial detectors is only about 2%. In other words, error in the TES resistance propagates to a smaller error in the approximate responsivity:

$$\frac{\Delta Reponsivity_{approx}}{Reponsivity_{approx}} \frac{R}{\Delta R} = \frac{2R}{r_{sh} * ((R/r_{sh})^2 - 1)} \quad (5.34)$$

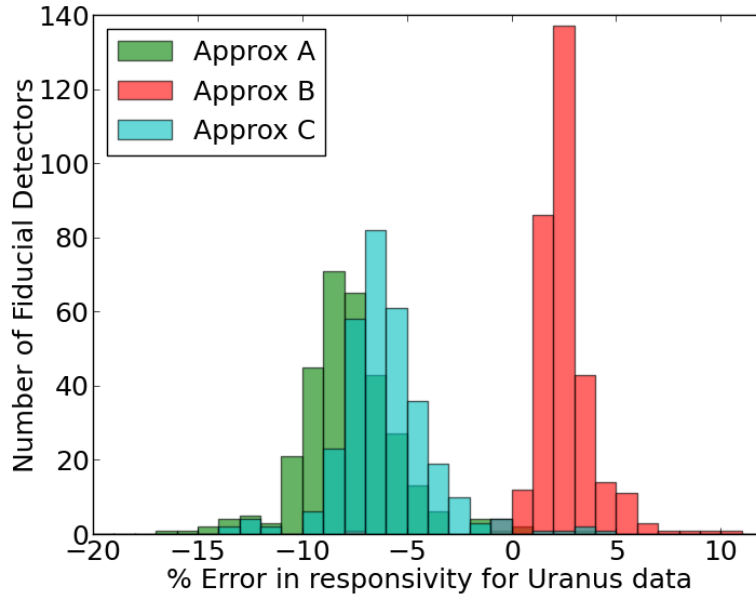


Figure 5.10: For the fiducial detectors in PA2, the median error in the responsivity approximation over the 2014 Uranus TODs when PWV/sin(ϵ) is less than 3 mm is shown. The median errors in the approximate responsivity over the fiducial detectors are 2% when Approximation A is used, -8% for Approximation B, and -6% for Approximation C. There are 2 data points above 12% and 1 points below -20% not shown.

This equation is plotted in Fig. 5.8. At all resistances larger than $10\%R_n$, a given % error in the TES resistance propagates to a smaller % error in the approximate responsivity. The amount of propagation of TES resistance error to the responsivity decreases with increasing TES resistance. At $50\%R_n$, the % error in TES responsivity is less than 20% of the % error in TES resistance.

In conclusion, the responsivity calculated by the current ACTPol method, Approximation C, is on average 6% smaller in magnitude than the actual value for the fiducial detectors. This means that we are underestimating the total optical efficiency of our system by a small amount.

5.5.3 Improvements to ACTPol responsivity calculation procedure

The ACTPol data is taken in sets of 15-minute files. A bias step is taken before each data file and an IV curve is taken every hour. We call the raw 15-minute data files time-ordered data sets (TODs). At the end of an observing season, the TODs are mapped out on their sky coordinates. To provide a high signal-to-noise map of the CMB temperature and polarization anisotropies, each patch of the sky is scanned many times.

The overall calibration of the data is provided by WMAP. However, it is necessary to calibrate the TODs relative to one another because they are summed together to make a map. Because the data from all the different detectors is added together, it is also necessary within one TOD to calibrate each detector's data relative to the other detectors' data.

To calibrate detectors relative to one another in one TOD, we calculate their relative coupling to the large amplitude atmosphere fluctuations. We assume that all detectors in the array see the same atmosphere loading at any instant, so there is a common mode atmosphere signal that all detectors see for the TOD.

To calculate the relative calibration between TODs, we need to calculate differences in the responsivity. Changes in the loading conditions from TOD to TOD can also result in different amounts of CMB signal being absorbed by the atmosphere. To account for both of these affects, we currently use planet observations. For a set of well-behaved or fiducial detectors, we measure their Uranus peak heights in pW as a function of atmosphere loading to provide a relative calibration between TODs. The fiducial detectors are chosen as the set of detectors that have relatively stable Uranus peak heights, calculated with the approximate responsivity and bias step functions, as a function of atmosphere loading, when the $PWV/\sin(\text{el})$ is less than 3 mm. There may be a slight slope in the Uranus peak height as a function of loading due to absorption of the signal by the atmosphere, but it is relatively flat for the fiducial detectors.

Using the exact responsivity and bias step functions instead of the approximate ones in this calculation process can help in a few ways. First, the measured responsivity and bias step functions help explain why a detector is in the fiducial set or not. If there are strong non-linearities in a detector's $R(T, I)$ transition, the exact bias step and responsivity functions will deviate strongly from the approximations, as shown in Fig. 5.4. The amount of deviation from the approximation also varies strongly as a function of loading and TES resistance, so the Uranus peak heights as calculated with the approximate functions will vary strongly depending on the bias point and loading.

In this chapter, I described a set of fiducial detectors defined as the detectors that had smooth $R(T, I)$ functions. About 82% of this set overlaps with the set of fiducial detectors defined as those with stable Uranus peak heights. This indicates that identifying detectors with smooth $R(T, I)$ functions is a promising method for finding fiducial detector candidates. (Other reasons why a detector may not have stable Uranus peak heights include detector instabilities, a tendency for the detector

to be biased high or low on the transition, and poor optical efficiency.) The exact responsivity and bias step functions will also help us determine when a detector should be used as part of the fiducial set- there are many detectors with slight non-linearities in a small section of the $R(T, I)$ curve that could be used as fiducial detectors if they are biased away from this region.

In the above discussion, we have been assuming that the detectors' responsivities remain constant over one TOD. That is, the changes in TES resistance are small enough over one TOD that we can apply one responsivity to the data set. For detectors with non-linearities in their $R(T, I)$ transition, as in Fig. 5.4, the responsivity is strongly dependent on the TES resistance when it is biased near the non-linearity. Detectors that do not follow the atmosphere common mode are currently cut from each TOD, and this should catch detectors with this problem. However, the measured responsivity and bias step functions again give us an understanding of why this occurs and a more intelligent method for determining when a detector will have this problem.

5.6 Detector biasing with bias step measurements

In the ACTPol detector arrays, there are 32-96 TESes biased in series on each bias line. Before taking data, it is necessary to calculate the I_{bias} that should be applied to each bias line to optimally bias its group of detectors. The optimal I_{bias} value changes throughout the day as the atmosphere loading and bath temperature fluctuate.

Currently, we take an IV curve once every hour and use the data to re-bias the detectors. The IV curve data is converted into the quantities R vs. I_{bias} , telling us what the resistance of each TES will be if a given I_{bias} is applied. From now on, we will refer to these data as R vs. I_{bias} curves. As discussed earlier, each IV curve takes about 5-7 minutes out of our observation time, including time to take the IV curve

and time for the array to cool off afterwards. We currently use bias steps to measure the $\%R_n$ of the detectors before data is taken, but not to re-bias the detectors. If we could re-bias the detectors using data from a bias step, which only take a few seconds, we could increase our observing time by 2-10%.

Compared to an IV curve, the disadvantage of the bias step is that it gives us the TES resistance value at one I_{bias} value, and we would like to know the TES resistance at all I_{bias} values for re-biasing. However, as discussed in Section 5.4.1, the function $P_l(R)|_{I_{bias}}$ is single-valued, so measuring R at the applied I_{bias} is enough to determine the P_l on each detector. We will always measure the same R vs. I_{bias} curve under the same P_l conditions. So, for each detector we could find the previously measured IV curve with a resistance at I_{bias} closest to the calculated value, and use this set of IV curves to re-bias the detectors.

Another way to re-bias the detectors using bias steps would be to measure the $\%R_n$ of each detector with a bias step, adjust I_{bias} if the $\%R_n$ is too high or too low, take another bias step to measure the $\%R_n$, and continue until the right I_{bias} value is found.

Both of these methods will only always work for detectors with single-valued $R(dI/dI_{bias})$ functions at the operating I_{bias} . One could get around this issue by taking a few bias steps at multiple I_{bias} values. Or, if the detectors are re-biased often enough, they would not drift far from the initial operating $\%R_n$ and it could always be known which of the multiple $\%R_n$ values is correct.

5.7 Conclusions and future work

In this chapter, we have demonstrated methods for measuring each detector's exact responsivity function and bias step function using only a set of IV curves. These mea-

measurements improve upon the approximations we currently using for the responsivity and bias step function by taking into account the effect of the TES $R(T, I)$ transition.

To calculate a detector's responsivity for a given data set, we need to know the TES resistance during the data set and the detector's responsivity function, $Resp(R, I_{bias})$. We calculate the TES resistance using the detector's bias step function, $R(dI/dI_{bias}|_{P_t}, I_{bias})$, and the $dI/dI_{bias}|_{P_t}$ value measured with the bias step taken before the data set. Currently, we use both the approximate bias step function and the approximate responsivity function for this calculation.

For detectors with smooth $R(T, I)$ transitions, using the exact bias step function instead of the approximation reduces the error in the resistance calculated from the bias step from up to 30% to less than 1.5%. This improved accuracy could allow us to use bias steps instead of IV curves for TES re-biasing, which could increase our observing time by 2-10%. The responsivity calculated using the approximate responsivity and bias step functions is close to the value calculated using the exact/measured responsivity and bias step functions for detectors with smooth $R(T, I)$ transitions, so we are doing a good job with our current method. It is on average only 6% lower than the actual value for these detectors, which means we are currently only underestimating the optical throughput of our system by about 6%..

For a detector with non-linearities in the $R(T, I)$ transition, the responsivity deviates strongly from the approximation and also depends strongly on the $\%R_n$ bias point. So, the exact responsivity function and the TES resistance during each data set will need to be measured very accurately to calculate the responsivity directly. The strong dependence of the responsivity on $\%R_n$ also may cause the responsivity to change significantly enough over one 15-minute data set that it will be unusable for that detector. These non-linearities also give rise to bias step functions that are not single-valued, so the TES resistance cannot be measured from one bias step measurement alone.

We currently get around these problems of detectors with non-linearities in their $R(T, I)$ transitions by the following methods. Instead of calculating the responsivities of these detectors directly, we calculate their responsivities relative to the detectors with smooth $R(T, I)$ transitions by comparing their response to the atmosphere common mode. We do not need to know the TES resistance from the bias step for re-biasing, because we currently re-bias detectors using IV curves. In the future, it would be best to reject detectors with these non-linearities during detector testing and selection if possible so that re-biasing with bias steps and directly measuring responsivities will be a simple process for all detectors.

Chapter 6

Conclusions and Future Work

At the time of writing, November 2015, all detector arrays are now deployed in the ACTPol receiver. The latest detector array, PA3, was installed before the 2015 observing season. We discussed some aspects of the performance of the PA3 array in Chapter 3. Under normal operating conditions, the PA3 detector P_{sat} values are high enough that the detectors do not saturate, and uniform enough that 99% of the detectors are biased onto their transitions. Although the optical efficiency is lower for some detectors than expected, the array is still the most sensitive ever installed on ACT, with a sensitivity $\leq 10 \mu K \sqrt{s}$ [44][25]. The PA3 array also has the highest electrical yield of the three ACTPol arrays, 86%, due to advanced assembly techniques described in Chapter 2.

The semihex detectors in PA3 were assembled with flex fabricated at Princeton University by a novel process presented in Chapter 3 [75]. The flex has performed well during observations, meeting the cryogenic and mechanical robustness and critical current requirements of the experiment. We are currently finishing the 2015 season observations, after which the ACTPol detector arrays will begin to be removed and upgraded with AdvACT arrays. The AdvACT arrays will also be assembled with the flex described in Chapter 3. The flex design easily accommodates the AdvACT

70 μm trace pitch requirement. This, along with the new 32 column by 64 row TDM readout scheme, allows us to read out up to 2048 TESes in each AdvACT array, double the number we had in the ACTPol arrays [42] [76].

In Chapter 5 of this thesis, we showed that for the ACTPol TESes, the R(T,I) transition significantly affects the responsivity function and the map from bias step amplitude to detector resistance. This is especially true for TESes with non-linearities in their R(T,I) curves. We demonstrated methods for calculating the exact responsivity function and the map from bias step amplitude to detector resistance. These can be used instead of the approximate functions we are currently using to calculate the responsivities more accurately.

The more accurate responsivities may help us subtract thermal pickup signals from the CMB data. As shown in Fig. 6.1, the bath temperature of the ACTPol detector arrays fluctuates as we scan the telescope, presumably due to disturbances of the cooling system by the motion. This creates a scan-synchronous spurious signal that causes striping in the maps. By calculating the responsivities accurately as laid out in Chapter 5, and using the relative κ measurement procedure discussed in Chapter 4, we can calculate each detector's thermal signal from the dark detectors. This is a promising avenue for removing these thermal pickup stripes from the maps without risking subtracting some CMB signal.

As a reminder, the responsivity, $Resp$, gives us a conversion from changes in TES current, which we directly measure, to changes in $P_{loading}$:

$$\Delta P_{loading} = Resp \Delta I, \tag{6.1}$$

where $P_{loading}$ is defined as:

$$P_{loading} = \eta P_{\gamma} + \kappa T_b^n. \tag{6.2}$$

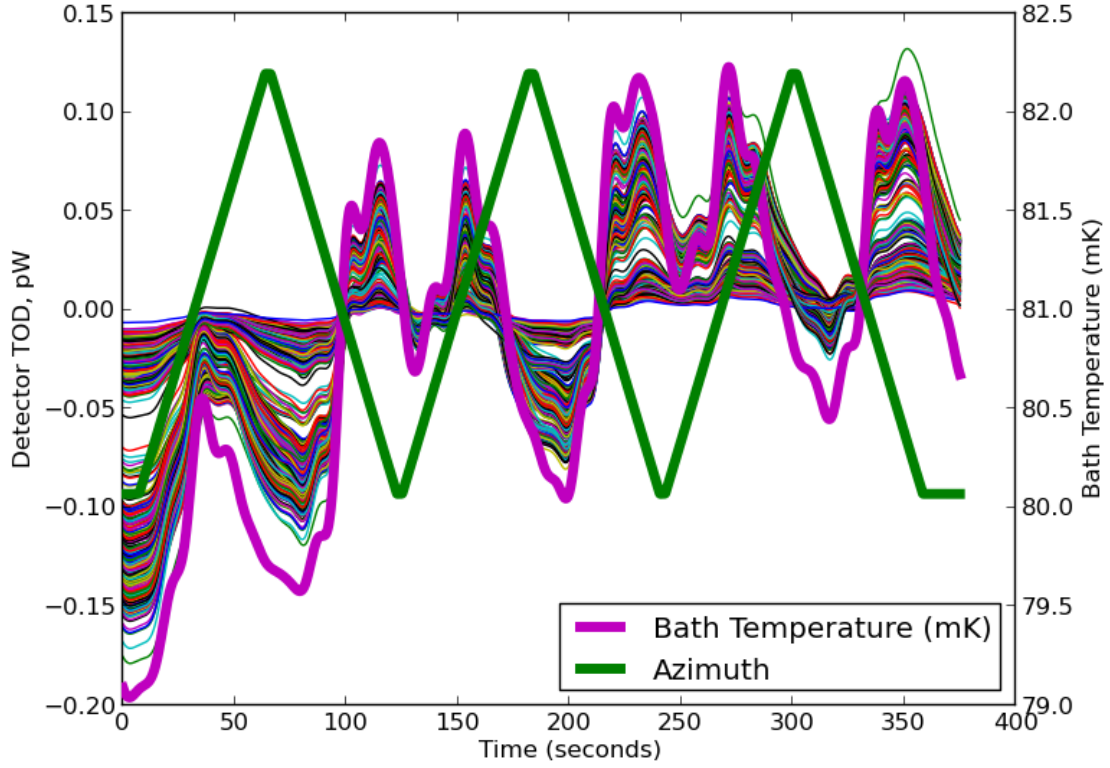


Figure 6.1: PA2 data taken with cover on the receiver window, to study only the thermal pickup signal induced by telescope scanning. The telescope was swept in azimuth back and forth across a 90° range. All detector TODs are plotted in pW. The approximate responsivity and bias step functions were used to calculate the responsivity.

So, when we measure a change in the detector current we do not know how much of the signal is due to a change in bath temperature and how much is due to a change in sky signal:

$$\Delta I = (\eta \Delta P_\gamma + \kappa \Delta(T_b^n)) / Resp. \quad (6.3)$$

To separate the bath temperature fluctuations from the sky signal that we would like to measure, we use dark detectors. These detectors do not have any optical lines bringing optical signal to the TES, so they only measure changes in bath temperature:

$$\Delta I_{dark} = (\kappa_{dark} \Delta(T_b^n)) / Resp_{dark}. \quad (6.4)$$

Assuming detectors all have very similar n values, which we have found for the detectors measured in the lab, if we have an accurate measure of responsivity and relative κ values, we can calculate the signal a detector sees due to bath temperature fluctuations, $\Delta I_{thermal}$:

$$\Delta I_{thermal} = \Delta I_{dark} \frac{\kappa}{\kappa_{dark}} \frac{Resp_{dark}}{Resp}. \quad (6.5)$$

Thus, by calculating the responsivities more accurately, we can accurately determine the thermal signal and subtract it from the maps. Using the measured bias step function instead of the approximation also provides accurate enough estimates of TES resistance that re-biasing detectors with bias steps instead of IV curves may be possible with more development. This could save 2-10% of our observation time and allow more frequent re-biasing.

With the data collected by ACTPol, our collaboration has already published CMB temperature and anisotropy spectra [71], evidence for lensing [90][61], and kSZ signals [80]. As more data are processed, the sensitivity of the maps will improve, leading to more precise primordial anisotropy spectra and secondary CMB signal detections.

Appendix A

Detector and readout diagnostic techniques

In this appendix, we discuss methods for diagnosing non-functional TESes and readout components. As described in Chapter 2, the ACTPol TES arrays are read out with a 32 column by 32 row SQUID time-division multiplexing system. We divide failures into two categories: non-functional multiplexing lines and non-functioning individual TESes. If one of the multiplexing lines is not functioning, we will be unable to readout an entire column or row of TESes.

Each column has five SQUID multiplexing lines that must all be continuous, as shown in Fig. A.1: the SQ1 FB, SQ2 FB, SQ2 bias, SA FB, and SA bias lines. There is also a closed transformer loop that couples all the SQ1 signals in a column to the SQ2, which we will call the SQ1 signal line. This line is a closed loop within the chip that is not connected to the MC PCB, so it cannot be checked for continuity from the MC PCB probe points or the connectors soldered to the MC PCB like the other lines. However, there are pads on the mux chip that can be probed to diagnose this line at room temperature.

There are 33 row select lines that each bias a row of SQ1s. There are 32 rows for biasing SQUIDS connected to TESes, and the extra row biases a row of dark SQUIDS that are not connected to a TES signal. They are used to isolate the spurious signal due to magnetic field pickup by the SQUIDS during observations. The SQ1s on each row select line are biased in series as shown in Fig. A.2. If a wire bond between a mux chip and the PCB is broken anywhere along the line, the row select line will not be continuous. None of the SQ1s in the row will be biased, and it will not be possible to read out any of the TESes in the row.

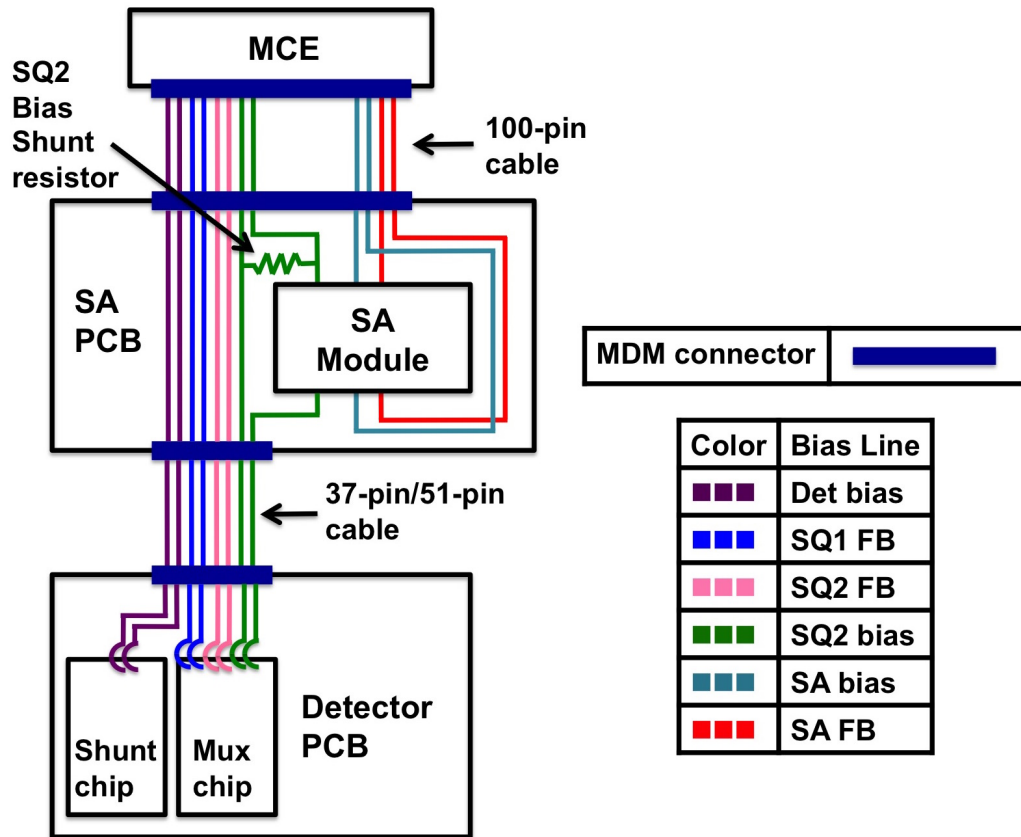


Figure A.1: Column critical lines wiring from MCE to detector PCB

To further reduce the number of wires routed from room temperature, 32-96 TESes are biased on one TES bias line. In each individual TES readout circuit, shown in Fig. 2.3, the TES is biased in parallel with a shunt resistor. Also as shown in Fig. 2.3,

the shunt resistor resides on the shunt chip. The shunt resistors on one shunt chip are biased in series on one line. On the semihex MC PCBs, three columns are biased by one bias line. On the hex MC PCBs, two columns are biased by one bias line.¹

If there is a discontinuity in any of the shunt resistors or bias line wiring on the shunt chip, the whole column of TESes will be lost. However, if there is a discontinuity for one TES readout circuitry in any of the circuitry biased in parallel with the shunt resistor in Fig. 2.3, such as the TES, the input inductor on the mux chip, or the Nyquist inductor on the shunt chip, we will be unable to read out only that TES, and the rest of the TESes on the bias line will be unaffected.

A.1 Warm diagnostics and pre-screening

The critical lines described above are wire-bonded to the MC PCB, and those PCB lines are soldered to a 37/51 pin MDM connector (in case of column lines) or ZIF connector (in case of row selects). So we can check for continuity of the multiplexing lines and shorts between them by measuring the connector pins or PCB probe points with a multimeter. We can also make a connection between the PCB and a special continuity checking electronics board with a cable to check these lines with an autoamted program.

However, if an individual TES circuit is open, it won't affect the continuity of critical lines. The individual TES bias/readout circuits are also only wire bonded to the chips on the board and not to the PCB itself. (All wiring in the individual TES circuits needs to be superconducting, and the PCB wiring is copper.) So, the only way to diagnose individual TES circuit issues warm is with on-chip probing.

¹In PA3, the 90 GHz detectors are read out with the even rows and the 150 GHz detectors are read out with the odd rows. Because the 150 GHz and 90 GHz detectors see different amount of loading, we put them on two different bias lines. So, for PA3 there are two bias lines- one for even rows and one for odd rows- for every two hex columns and every three semihex columns. We re-purposed lines previously used for heaters in PA1 and PA2 that did not end up working well as additional TES bias lines for PA3.

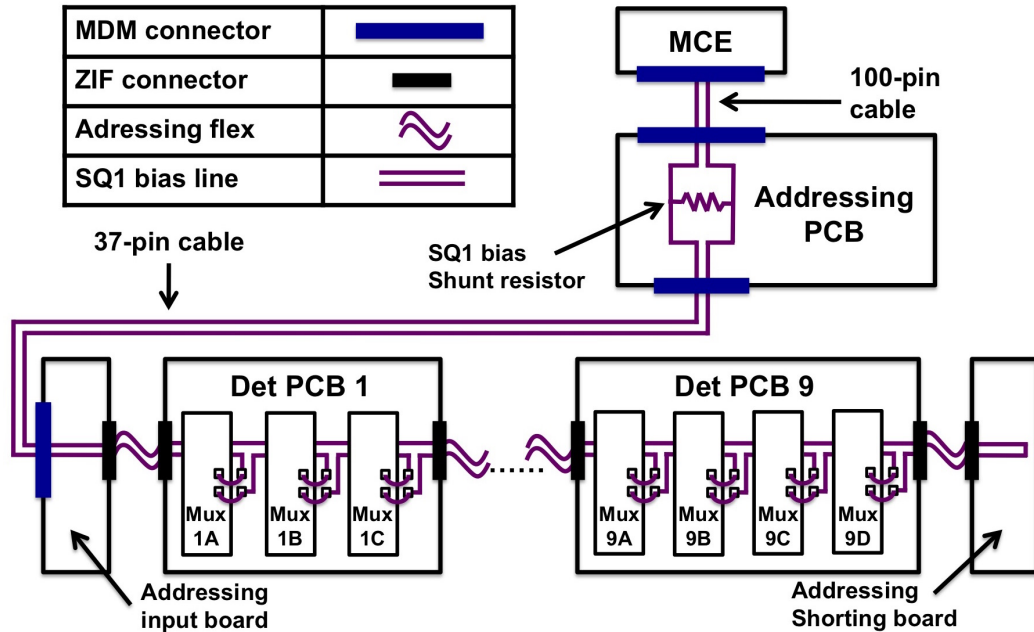


Figure A.2: Row select wiring from MCE to detector PCB

Most of the components of the detector/readout array are screened before assembly. The mux chips are tested at cryogenic temperatures at NIST. The shunt and wiring chips were probed at room temperature before assembly for PA2 and PA3. The TechEtch flex was electrically screened to ensure traces were continuous and not shorted to one another by the manufacturer before delivery. The flex fabricated at Princeton was probed at room temperature. The detector wafers were probed at room temperature at NIST and at Princeton.

The TES bias circuits were sometimes probed after wire bonding to ensure that good wire bonds were made. If the chips are clean and mounted well, the instance of wire bonding failures should be well below 1%. In this case, probing after wire bonding should be unnecessary. As discussed in Chapter 2, we did at times have quite a bit of difficulty wire bonding to the TechEtch flex and often probed after wire bonding to this flex.

A.2 Cold diagnostics

When the detectors are cold, all diagnostics are made through the MCE. First, we check for any problems with multiplexing lines. Then, individual TES problems are diagnosed.

A.2.1 Cold diagnostics: Critical lines

Table A.1: The effect of non-functioning critical lines, listed in the leftmost column, on the SA ramp, SQ2 servo, SQ1 servo, and continuity check data is shown. The “-” symbol indicates the non-functioning critical line has no effect on the data. The markers “Col ×” and “Row ×” indicate the SQUID data will show no response in the column, or row, respectively, of the non-functioning critical line. In the case of a non-functioning SA FB line, the effect on the SQ1 servo data is marked as “?” because it depends on if there is enough gain in the part of the SA signal vs. SQ2 signal curve where the SA state naturally resides without applying a SA FB current.

Open or shorted Critical line:	SA Ramp	SQ2 Servo	SQ1 Servo	Shows up in Continuity check?
SQ1 FB	-	-	Col ×	yes
SQ1 bias	-	-	Row ×	not if problem is below addressing board shunt resistor
SQ1 sig	-	-	Col ×	no
SQ2 FB	-	Col ×	Col ×	yes
SQ2 bias	-	Col ×	Col ×	not if problem is below SA board shunt resistor
SA FB	Col ×	Col ×	?	yes
SA bias	Col ×	Col ×	Col ×	yes

Cold continuity check

We can check for continuity of the multiplexing lines and shorts between the multiplexing lines from the MCE with a special “continuity check” electronics card. We are able to check for continuity of all the lines in this manner, but are only able to check for shorts between lines that are connected to the same electronics card slot of the MCE. (If a short between two lines connected to different slots is suspected, the lines can be hand-probed with a multimeter.)

As shown in Figures A.2 and A.1, there are shunt resistors in the addressing and SA boards for the row select and SQ2 bias lines. Thus, we cannot know if a SQ2 bias line or row select line is open below the SA board or addressing board by measuring the continuity of these lines from the MCE. It is also possible for readout lines to look ok in the continuity check but not be operational (for example if there is a superconducting short across the SQUID). For this reason, we also use the SQUID autoseup data, described below, to diagnose multiplexing line problems when the detectors are cold.

SQUID autoseup data

We run a SQUID autoseup script, as described in Battistelli 2008 [10], to set up the SQUIDs before taking detector data. The script selects the optimal SQUID biases as well as the SA and SQ2 FB values and the SQ1 lock points. We can also use the data taken to find these values to diagnose any SQUID or SQUID readout line failures that are not found with the continuity check. Each critical line can be diagnosed through a combination of the autoseup data and the continuity check data, as shown in Table A.1.

The SQUID data sets we use the most for readout diagnostics are the SQ1 servo, the SQ2 servo, and the SA ramp. In all of these data sets, the SQUID’s FB coil is ramped and the SQUID response to the constantly increasing FB flux is measured

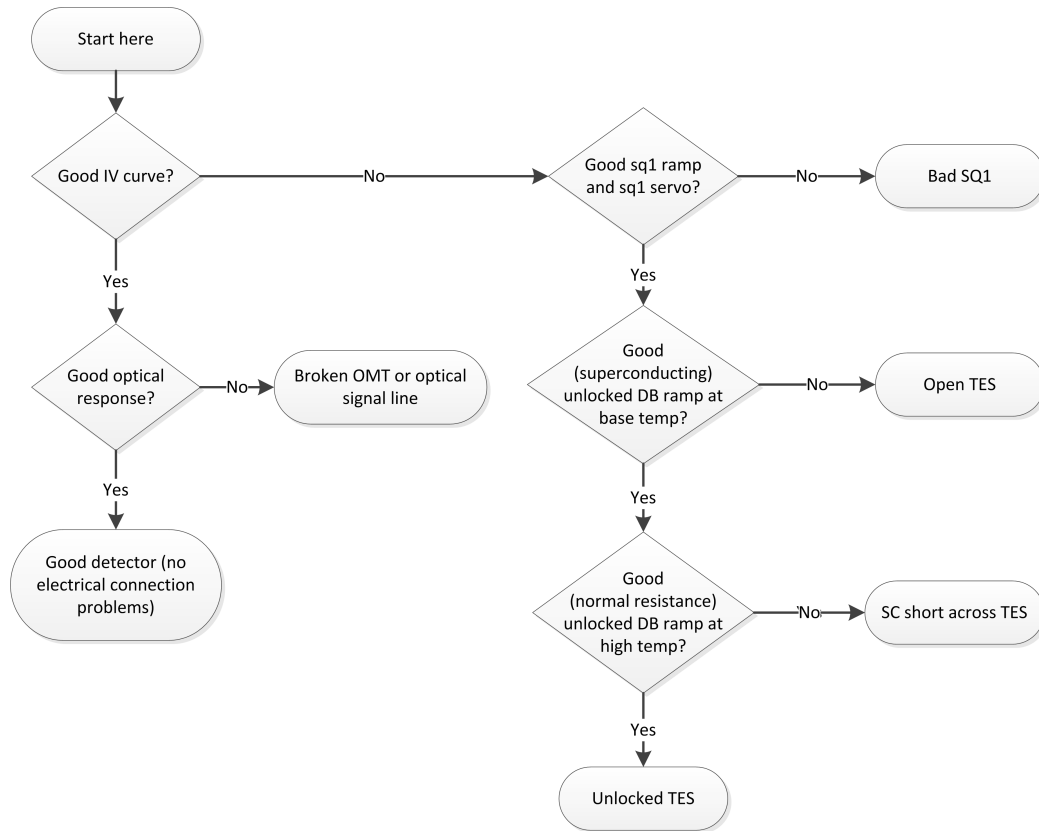


Figure A.3: Individual TES circuit cold diagnosis flow chart. The types of data referred to here are defined in the text.

in some way. If the SQUIDS are working correctly, this data should show a periodic pattern as shown in Fig.2.5. If a SQUID is not operating or a readout wire is open, this data will instead look flat.

To take the SQ1 servo data, the SQ1 FB coil is ramped and the SQ2 is held at its lockpoint in a feedback loop. We measure the SQ2 FB current necessary to keep the SQ2 at its lock point as a function of the SQ1 FB current. The SQ2 servo data is taken in the same way as the SQ1 servo data, except that the SQ2 FB current is ramped and the SA FB current necessary to keep the SA at its lockpoint is measured. For the SA ramp, the SA FB current is ramped and the SA signal is measured.

A.2.2 Cold diagnostics: Individual TES circuits

If a TES is non-operational and there are no problems with its multiplexing lines, there is a problem either with the detector itself or its individual readout circuit. If an individual TES fails, it may be due to an open line in the individual TES bias/readout circuit, a superconducting short across the TES, a non-operational SQ1, a broken signal line or OMT, or instabilities preventing the SQ1 from maintaining its lock point.

In Figure A.3, a flow chart describing the diagnosis process we go through for determining the failure mode is shown. The diagnostic data used are the detector's optical response, IV curve, SQ1 servo, and unlocked detector bias (DB) ramp. For the unlocked DB ramp, the DB is ramped while the SA signal is measured with the MCE operating in unlocked mode. This means that instead of locking onto the SQ1 and measuring the FB signal, no SQ1 FB is applied and the SA signal is measured. The unlocked DB ramp data is used to distinguish between SQUID locking issues and other detector problems.

Appendix B

Flex Fabrication Recipes

In this appendix, we give the recipes used with Princeton University MNFL equipment for the flex fabrication process in Chapter 3.

B.1 Aluminum oxide ALD

The recipe we use to grow 1000 atomic layers of Al_2O_3 using the Cambridge NanoTech Savannah 100 Atomic Layer Deposition System (ALD) is shown in the table below. During the growth, the wafer is heated to 300°C as read by the “inner” thermometer and 250°C as read by the “outer” thermometer.

To grow one atomic layer of Al_2O_3 , the ALD first exposes the wafer to water vapor, then pumps it away, leaving an atomic layer of water on the surface of the wafer. It then exposes the wafer to trimethylaluminum gas which reacts with the water to form one atomic layer of Al_2O_3 . Any residual trimethylaluminum is then pumped away and the cycle is repeated.

In the recipe below, the first step is to flood the wafer with only water vapor, to wet the surface. In the second step, 10 layers of Al_2O_3 are grown using a longer exposure time than in the main growth step (step 3), because the reactants do not

stick as well to the surface until some Al_2O_3 is deposited. Step three is the main growth step, in which 1000 atomic layers of Al_2O_3 are deposited.

Table B.1: ALD recipe for 1000 atomic layers of Al_2O_3 . Step 1: Water exposure. Heat: 300°C inner, 250°C outer.

Valve	Pulse (sec)	Expo (sec)	Pump (sec)	Flow (sccm)	Delay (sec)
0	.01	0	5	20	0
0	.01	0	5	20	0

Table B.2: ALD recipe for 1000 atomic layers of Al_2O_3 . Step 2: Build up the first few layers. Heat: 300°C inner, 250°C outer.

Valve	Pulse (sec)	Expo (sec)	Pump (sec)	Flow (sccm)	Delay (sec)
0	0.1	1	7	20	0
1	0.1	1	7	20	0

Table B.3: ALD recipe for 1000 atomic layers of Al_2O_3 . Step 3: Main growth step. Heat: 300°C inner, 250°C outer.

Valve	Pulse (sec)	Expo (sec)	Pump (sec)	Flow (sccm)	Delay (sec)
0	.01	0	5	20	0
1	.01	0	5	20	0

B.2 Oxygen plasma etch of polyimide

In the tables below, the oxygen plasma etch recipes we use for etching polyimide in the PT790 and TePla are shown. The etch rate of 3 $\mu\text{m}/60$ min in the table below applies for a 60 minute etch. It is not true that for example a 20 minute etch will etch 1 μm of polyimide because the TePla etch rate is highly non-linear. It is very sensitive to the temperature of the chamber, so over a long etch (> 10 minutes), the chamber will get progressively hotter and the etch rate progressively faster. In

contrast, if many short etches are performed that add up in time to the duration of the long etch, the chamber will cool off when it is vented in between etches.

Table B.4: PlasmaTherm 790 RIE oxygen plasma etch recipe, for etching polyimide

O2 flow	Pressure	Bias power	Etch rate
50 sccm	100 mTorr	400 Watts	1 $\mu\text{m}/\text{min}$

Table B.5: PVA TePla M4L ICP oxygen plasma etch recipe, for etching polyimide

O2 flow	Pressure	ICP power	Etch rate
150 sccm	500 mTorr	500 Watts	3 $\mu\text{m}/60 \text{ min}$

B.3 DRIE silicon etch

The steps for one cycle of the Samco 800 recipe 3 DRIE silicon etch process, used to remove the silicon from the flex in the areas where we want it to be flexible, are listed in the table below. The etch rate is slightly uneven across the wafer. About 450 cycles are needed to etch through a 525 μm wafer.

Table B.6: Steps for one cycle of the Samco 800 recipe 3.

Step	O2 flow	SF6 flow	C4F8 flow	Bias Power	ICP Power	time
1	10 sccm	100 sccm	300 sccm	10 Watts	2000 Watts	2 sec
2	10 sccm	100 sccm	0 sccm	120 Watts	500 Watts	2 sec
3	10 sccm	400 sccm	0 sccm	10 Watts	2000 Watts	4 sec
4	10 sccm	400 sccm	300 sccm	10 Watts	2000 Watts	1 sec

Appendix C

Lab optical efficiency measurement apparatus

In this appendix, we describe the apparatus used to measure the optical efficiency of the PA3 FH4 hex wafer in the lab. Each aspect of the apparatus is pictured in the figures in this appendix and described in detail in the captions. The results of the FH4 optical efficiency measurements are described in Chapter 4.

For the optical efficiency tests, an Eccosorb CR-110 coated aluminum cold load with a pyramid structure anti-reflective coating, shown in Fig. C.2, is used as the blackbody radiation source. Two free-space low-pass filters, shown in Fig. C.3, are installed in between the cold load radiation source and the detectors. An array of copper feedhorns, as shown in Fig. C.1, is used in lieu of the gold-plated silicon feedhorn array that is used with the full PA3 detector array.



Figure C.1: Detector assembly for optical efficiency measurements. The detector wafer sits on a gold-plated wafer base and is covered by a copper shield to prevent heating of the back of the wafer by the cold load radiation. A thermometer mounted to the inside of the copper shield is used to measure the detector wafer bath temperature. An array of copper smooth-walled feedhorns with a 10° angle edge-to-edge opening hang from the wafer base. Each feedhorn is positioned so that it will be exactly aligned with the detector pixel to which it couples radiation after the slightly larger low temperature contraction of the copper wafer base and feedhorns relative to the detector wafer.

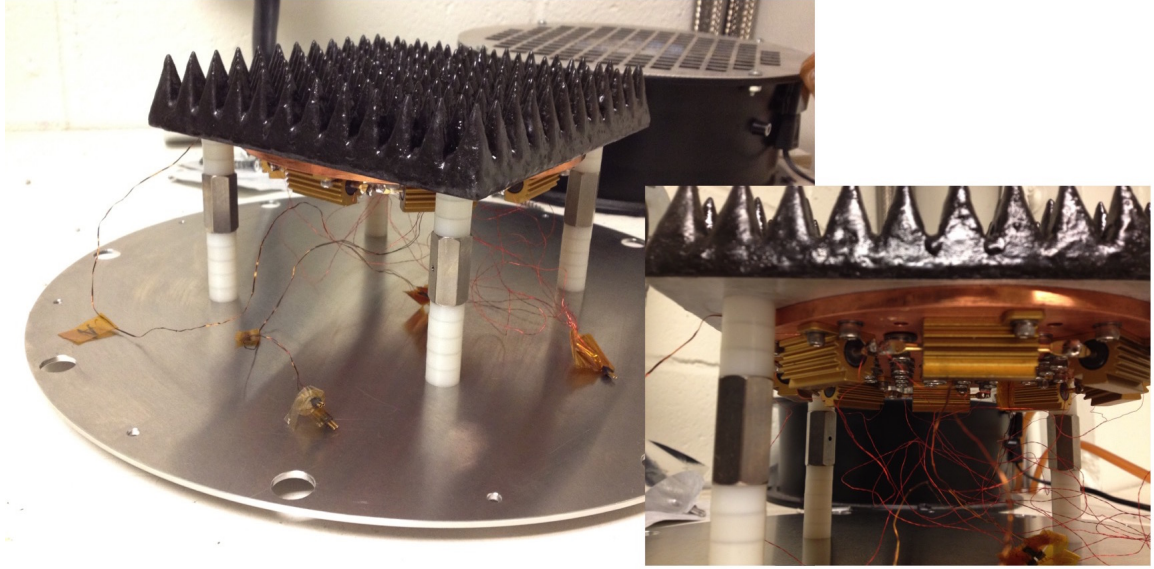


Figure C.2: Cold load used as the radiation source. The cold load is a 15.2 cm long by 15.2 cm wide piece of aluminum with pyramids 2.5 cm tall and 1.3 cm wide cut into its surface. It is coated with Eccosorb CR-110. On the bottom of the cold load, a ring of heaters connected to a copper plate provide even heating of the cold load. It is weakly thermally coupled to the second pulse tube/3K stage with 1/4-20 stainless steel rods at the corners of the cold load.

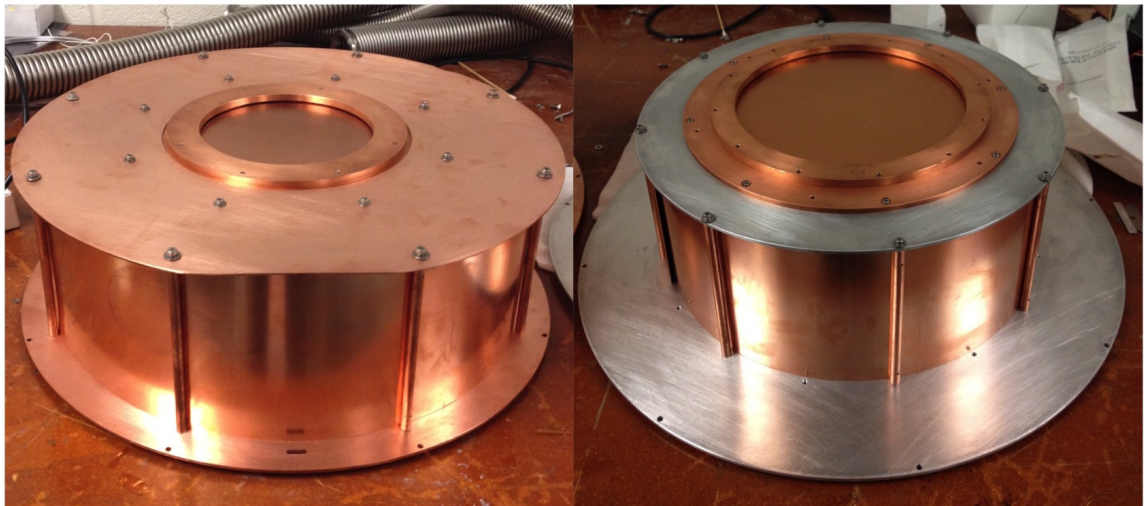


Figure C.3: Filters used during the optical efficiency measurements. The filter on the right is connected to the bottom of the 3K shell, with the cold load inside of the raised structure. The filter on the left is connected to the bottom of the 1K shell. The detector feedhorns hang just above the 1K filter. The 3K filter structure fits inside of the 1K filter structure (without touching, so as to not create a thermal short).

Bibliography

- [1] P. A. R. Ade, Y. Akiba, A. E. Anthony, K. Arnold, M. Atlas, D. Barron, D. Boettger, J. Borrill, S. Chapman, Y. Chinone, M. Dobbs, T. Elleflot, J. Errard, G. Fabbian, C. Feng, D. Flanigan, A. Gilbert, W. Grainger, N. W. Halverson, M. Hasegawa, K. Hattori, M. Hazumi, W. L. Holzapfel, Y. Hori, J. Howard, P. Hyland, Y. Inoue, G. C. Jaehnig, A. Jaffe, B. Keating, Z. Kermish, R. Keskitalo, T. Kisner, M. Le Jeune, A. T. Lee, E. Linder, E. M. Leitch, M. Lungu, F. Matsuda, T. Matsumura, X. Meng, N. J. Miller, H. Morii, S. Moyerman, M. J. Myers, M. Navaroli, H. Nishino, H. Paar, J. Peloton, E. Quealy, G. Rebeiz, C. L. Reichardt, P. L. Richards, C. Ross, I. Schanning, D. E. Schenck, B. Sherwin, A. Shimizu, C. Shimmin, M. Shimon, P. Siritanasak, G. Smecher, H. Spieler, N. Stebor, B. Steinbach, R. Stompor, A. Suzuki, S. Takakura, T. Tomaru, B. Wilson, A. Yadav, and O. Zahn. Measurement of the Cosmic Microwave Background polarization lensing power spectrum with the POLARBEAR experiment. *Phys. Rev. Lett.*, 113:021301, Jul 2014.
- [2] PAR Ade, N Aghanim, C Armitage-Caplan, M Arnaud, M Ashdown, F Atrio-Barandela, J Aumont, C Baccigalupi, Anthony J Banday, RB Barreiro, et al. Planck 2013 results. xv. CMB power spectra and likelihood. *Astronomy & Astrophysics*, 571:A15, 2014.
- [3] PAR Ade, N Aghanim, M Arnaud, M Ashdown, J Aumont, C Baccigalupi, AJ Banday, RB Barreiro, JG Bartlett, N Bartolo, et al. Planck 2015 results.

- XV. Gravitational lensing. *arXiv preprint arXiv:1502.01591*, 2015.
- [4] PAR Ade, Y Akiba, AE Anthony, K Arnold, M Atlas, D Barron, D Boettger, J Borrill, S Chapman, Y Chinone, et al. A measurement of the cosmic microwave background B-mode polarization power spectrum at sub-degree scales with POLARBEAR. *The Astrophysical Journal*, 794(2):171, 2014.
- [5] Peter AR Ade, N Aghanim, Z Ahmed, RW Aikin, KD Alexander, M Arnaud, J Aumont, C Baccigalupi, AJ Banday, D Barkats, et al. Joint analysis of BICEP2/Keck Array and Planck data. *Physical review letters*, 114(10):101301, 2015.
- [6] N Aghanim, M Arnaud, M Ashdown, J Aumont, C Baccigalupi, AJ Banday, RB Barreiro, JG Bartlett, N Bartolo, E Battaner, et al. Planck 2015 results. xi. CMB power spectra, likelihoods, and robustness of parameters. *arXiv preprint arXiv:1507.02704*, 2015.
- [7] Christopher P Ahn, Rachael Alexandroff, Carlos Allende Prieto, Scott F Anderson, Timothy Anderton, Brett H Andrews, Éric Aubourg, Stephen Bailey, Eduardo Balbinot, Rory Barnes, et al. The ninth data release of the Sloan Digital Sky Survey: first spectroscopic data from the SDSS-III Baryon Oscillation Spectroscopic Survey. *The Astrophysical Journal Supplement Series*, 203(2):21, 2012.
- [8] Reena Al-Dahleh. *Integrated MEMS-Based Phase Shifters*. Electrical and computer engineering PhD thesis, University of Waterloo, Waterloo, Ontario, Canada, 2008.
- [9] C. A. Allen, D. E. Franz, and S. H. Moseley. Compliant system of polyimide microwires for cryogenic detector applications. *Journal of Vacuum Science and Technology A*, 24(4):1552–1555, 2006.

- [10] ES Battistelli, M Amiri, B Burger, MJ Devlin, SR Dicker, WB Doriese, R Dünner, RP Fisher, JW Fowler, M Halpern, et al. Automated squid tuning procedure for kilo-pixel arrays of tes bolometers on the atacama cosmology telescope. In *SPIE Astronomical Telescopes+ Instrumentation*, pages 702028–702028. International Society for Optics and Photonics, 2008.
- [11] E.S. Battistelli, M. Amiri, B. Burger, M. Halpern, S. Knotek, M. Ellis, X. Gao, D. Kelly, M. MacIntosh, K. Irwin, and C. Reintsema. Functional description of read-out electronics for time-domain multiplexed bolometers for millimeter and sub-millimeter astronomy. *Journal of Low Temperature Physics*, 151(3-4):908–914, 2008.
- [12] Daniel Baumann, Mark G Jackson, Peter Adshead, Richard Easther, Alexandre Amblard, Asantha Cooray, Amjad Ashoorioon, Scott Watson, Nicola Bartolo, Sabino Matarrese, et al. Probing inflation with CMB polarization. In *AIP Conference Proceedings*, volume 1141, 2009.
- [13] Douglas A Bennett, Daniel S Swetz, Daniel R Schmidt, and Joel N Ullom. Resistance in transition-edge sensors: A comparison of the resistively shunted junction and two-fluid models. *Physical Review B*, 87(2):020508, 2013.
- [14] Mark Birkinshaw. The SunyaevZeldovich effect. *Physics Reports*, 310(23):97 – 195, 1999.
- [15] LE Bleem, JW Appel, JE Austermann, JA Beall, DT Becker, BA Benson, J Britton, JE Carlstrom, CL Chang, HM Cho, et al. Optical properties of feedhorn-coupled TES polarimeters for CMB polarimetry. In *Aip Conference Proceedings*, volume 31, page 479, 2009.
- [16] Joe W Britton, John P Nibarger, Ki Won Yoon, James A Beall, Dan Becker, Hsiao-Mei Cho, Gene C Hilton, Johannes Hubmayr, Michael D Niemack, and

- Kent D Irwin. Corrugated silicon platelet feed horn array for CMB polarimetry at 150 GHz. In *SPIE Astronomical Telescopes+ Instrumentation*, pages 77410T–77410T. International Society for Optics and Photonics, 2010.
- [17] Erminia Calabrese, Renée Hložek, Nick Battaglia, J Richard Bond, Francesco de Bernardis, Mark J Devlin, Amir Hajian, Shawn Henderson, J Colin Hil, Arthur Kosowsky, et al. Precision epoch of reionization studies with next-generation CMB experiments. *Journal of Cosmology and Astroparticle Physics*, 2014(08):010, 2014.
- [18] John E. Carlstrom, Gilbert P. Holder, and Erik D. Reese. Cosmology with the Sunyaev-Zeldovich effect. *Annual Review of Astronomy and Astrophysics*, 40:643, 2002.
- [19] JA Chervenak, Kent D Irwin, Erich N Grossman, John M Martinis, Carl D Reintsema, and ME Huber. Superconducting multiplexer for arrays of transition edge sensors. *Applied Physics Letters*, 74(26):4043–4045, 1999.
- [20] Wim Christiaens. *Active and Passive Component Integration in Polyimide Interconnection Substrates*. Electrical engineering PhD thesis, Ghent University, Ghent, Belgium, 2009.
- [21] Leon N Cooper. Superconductivity in the neighborhood of metallic contacts. *Physical Review Letters*, 6(12):689, 1961.
- [22] AT Crites, JW Henning, PAR Ade, KA Aird, JE Austermann, JA Beall, AN Bender, BA Benson, LE Bleem, JE Carlstrom, et al. Measurements of e-mode polarization and temperature-e-mode correlation in the Cosmic Microwave Background from 100 square degrees of SPTpol data. *The Astrophysical Journal*, 805(1):36, 2015.

- [23] G. Danev, E. Spassova, and K. Popova. Morphology of thin polyimide films. *Thin Solid Films*, 228(12):301 – 303, 1993.
- [24] Sudeep Das, Thibaut Louis, Michael R Nolta, Graeme E Addison, Elia S Battistelli, J Richard Bond, Erminia Calabrese, Devin Crichton, Mark J Devlin, Simon Dicker, et al. The Atacama Cosmology Telescope: Temperature and gravitational lensing power spectrum measurements from three seasons of data. *Journal of Cosmology and Astroparticle Physics*, 2014(04):014, 2014.
- [25] R. Datta, J. Austermann, J.A. Beall, D. Becker, K.P. Coughlin, S.M. Duff, P.A. Gallardo, E. Grace, M. Hasselfield, S.W. Henderson, G.C. Hilton, S.P. Ho, J. Hubmayr, B.J. Koopman, J.V. Lanen, D. Li, J. McMahon, C.D. Munson, F. Nati, M.D. Niemack, L. Page, C.G. Pappas, M. Salatino, B.L. Schmitt, A. Schillaci, S.M. Simon, S.T. Staggs, J.R. Stevens, E.M. Vavagiakis, J.T. Ward, and E.J. Wollack. Design and deployment of a multichroic polarimeter array on the Atacama Cosmology Telescope. *Journal of Low Temperature Physics*, 2016.
- [26] Rahul Datta, Johannes Hubmayr, Charles Munson, Jason Austermann, James Beall, Dan Becker, Hsiao-Mei Cho, Nils Halverson, Gene Hilton, Kent Irwin, et al. Horn coupled multichroic polarimeters for the Atacama Cosmology Telescope polarization experiment. *Journal of Low Temperature Physics*, 176(5-6):670–676, 2014.
- [27] S Dunn. HD 4000 profile optimization through process enhancement through process enhancement. 2004 Symposium on Polymers, 2004.
- [28] Rolando Dünner, Matthew Hasselfield, Tobias A Marriage, Jon Sievers, Viviana Acquaviva, Graeme E Addison, Peter AR Ade, Paula Aguirre, Mandana Amiri, John William Appel, et al. The Atacama Cosmology Telescope: data characterization and mapmaking. *The Astrophysical Journal*, 762(1):10, 2013.

- [29] Frank D Egitto and Luis J Matienzo. Plasma modification of polymer surfaces for adhesion improvement. *IBM Journal of Research and Development*, 38(4):423–439, 1994.
- [30] DJ Fixsen, ES Cheng, JM Gales, John C Mather, RA Shafer, and EL Wright. The Cosmic Microwave Background spectrum from the full COBE FIRAS data set. *The Astrophysical Journal*, 473(2):576, 1996.
- [31] R Flitsch and D-Y Shih. A study of modified polyimide surfaces as related to adhesion. *Journal of Vacuum Science & Technology A*, 8(3):2376–2381, 1990.
- [32] TH Geballe, BT Matthias, E Corenzwit, and GW Hull Jr. Superconductivity in molybdenum. *Physical Review Letters*, 8(8):313, 1962.
- [33] AK Geim, SV Dubonos, IV Grigorieva, KS Novoselov, AA Zhukov, and S Yu Shapoval. Microfabricated adhesive mimicking gecko foot-hair. *Nature materials*, 2(7):461–463, 2003.
- [34] K. Gilleo. *Handbook of Flexible Circuits*. Springer US, 1998.
- [35] Evangelos Gogolides, Vassilios Constantoudis, George Kokkoris, Dimitrios Kontziampasis, Katerina Tsougeni, George Boulousis, Marilena Vlachopoulou, and Angeliki Tserepi. Controlling roughness: from etching to nanotexturing and plasma-directed organization on organic and inorganic materials. *Journal of Physics D: Applied Physics*, 44(17):174021, 2011.
- [36] Matthew J Griffin, James J Bock, and Walter K Gear. Relative performance of filled and feedhorn-coupled focal-plane architectures. *Applied Optics*, 41(31):6543–6554, 2002.

- [37] M. Grunze, G. Hähner, Ch. Wöll, and W. Schrepp. Interphase orientation of polyimide on polycrystalline gold, silver and si(100). *Surface and Interface Analysis*, 20(5):393–401, 1993.
- [38] Nick Hand, Graeme E. Addison, Eric Aubourg, Nick Battaglia, Elia S. Battistelli, Dmitry Bizyaev, J. Richard Bond, Howard Brewington, Jon Brinkmann, Benjamin R. Brown, Sudeep Das, Kyle S. Dawson, Mark J. Devlin, Joanna Dunkley, Rolando Dunner, Daniel J. Eisenstein, Joseph W. Fowler, Megan B. Gralla, Amir Hajian, Mark Halpern, Matt Hilton, Adam D. Hincks, Renée Hlozek, John P. Hughes, Leopoldo Infante, Kent D. Irwin, Arthur Kosowsky, Yen-Ting Lin, Elena Malanushenko, Viktor Malanushenko, Tobias A. Marriage, Danica Marsden, Felipe Menanteau, Kavilan Moodley, Michael D. Niemack, Michael R. Nolta, Daniel Oravetz, Lyman A. Page, Nathalie Palanque-Delabrouille, Kaike Pan, Erik D. Reese, David J. Schlegel, Donald P. Schneider, Neelima Sehgal, Alaina Shelden, Jon Sievers, Cristóbal Sifón, Audrey Simmons, Stephanie Snedden, David N. Spergel, Suzanne T. Staggs, Daniel S. Swetz, Eric R. Switzer, Hy Trac, Benjamin A. Weaver, Edward J. Wollack, Christophe Yeche, and Caroline Zunckel. Evidence of galaxy cluster motions with the Kinematic Sunyaev-Zel’dovich Effect. *Phys. Rev. Lett.*, 109:041101, Jul 2012.
- [39] D. Hanson, S. Hoover, A. Crites, P. A. R. Ade, K. A. Aird, J. E. Austermann, J. A. Beall, A. N. Bender, B. A. Benson, L. E. Bleem, J. J. Bock, J. E. Carlstrom, C. L. Chang, H. C. Chiang, H-M. Cho, A. Conley, T. M. Crawford, T. de Haan, M. A. Dobbs, W. Everett, J. Gallicchio, J. Gao, E. M. George, N. W. Halverson, N. Harrington, J. W. Henning, G. C. Hilton, G. P. Holder, W. L. Holzapfel, J. D. Hrubes, N. Huang, J. Hubmayr, K. D. Irwin, R. Keisler, L. Knox, A. T. Lee, E. Leitch, D. Li, C. Liang, D. Luong-Van, G. Marsden, J. J. McMahon, J. Mehl, S. S. Meyer, L. Mocuano, T. E. Montroy, T. Natoli, J. P. Nibarger,

- V. Novosad, S. Padin, C. Pryke, C. L. Reichardt, J. E. Ruhl, B. R. Saliwanchik, J. T. Sayre, K. K. Schaffer, B. Schulz, G. Smecher, A. A. Stark, K. T. Story, C. Tucker, K. Vanderlinde, J. D. Vieira, M. P. Viero, G. Wang, V. Yefremenko, O. Zahn, and M. Zemcov. Detection of B -Mode Polarization in the Cosmic Microwave Background with data from the South Pole Telescope. *Phys. Rev. Lett.*, 111:141301, Sep 2013.
- [40] D Hanson, S Hoover, A Crites, PAR Ade, KA Aird, JE Austermann, JA Beall, AN Bender, BA Benson, LE Bleem, et al. Detection of B-mode polarization in the cosmic microwave background with data from the South Pole Telescope. *Physical Review Letters*, 111(14):141301, 2013.
- [41] Matthew Hasselfield, Matt Hilton, Tobias A. Marriage, Graeme E. Addison, L. Felipe Barrientos, Nicholas Battaglia, Elia S. Battistelli, J. Richard Bond, Devin Crichton, Sudeep Das, Mark J. Devlin, Simon R. Dicker, Joanna Dunkley, Rolando Dnner, Joseph W. Fowler, Megan B. Gralla, Amir Hajian, Mark Halpern, Adam D. Hincks, Rene Hlozek, John P. Hughes, Leopoldo Infante, Kent D. Irwin, Arthur Kosowsky, Danica Marsden, Felipe Menanteau, Kavilan Moodley, Michael D. Niemack, Michael R. Nolta, Lyman A. Page, Bruce Partridge, Erik D. Reese, Benjamin L. Schmitt, Neelima Sehgal, Blake D. Sherwin, Jon Sievers, Cristbal Sifn, David N. Spergel, Suzanne T. Staggs, Daniel S. Swetz, Eric R. Switzer, Robert Thornton, Hy Trac, and Edward J. Wollack. The Atacama Cosmology Telescope: Sunyaev-Zel'dovich selected galaxy clusters at 148 ghz from three seasons of data. *Journal of Cosmology and Astroparticle Physics*, 2013(07):008, 2013.
- [42] S.W. Henderson, R. Allison, J. Austermann, T. Baildon, N. Battaglia, J.A. Beall, D. Becker, F. De Bernardis, J.R. Bond, E. Calabrese, S.K. Choi, K.P. Coughlin, K.T. Crowley, R. Datta, M.J. Devlin, S.M. Duff, R. Dunner, J. Dunkley, A. van

- Engelen, P.A. Gallardo, E. Grace, M. Hasselfield, F. Hills, G.C. Hilton, A.D. Hincks, R. Hlozek, S.P. Ho, J. Hubmayr, K. Huffenberger, J.P. Hughes, K.D. Irwin, B.J. Koopman, A.B. Kosowsky, D. Li, J. McMahon, C. Munson, F. Nati, L. Newburgh, M.D. Niemack, P. Niraula, L.A. Page, C.G. Pappas, M. Salatino, A. Schillaci, B.L. Schmitt, N. Sehgal, B.D. Sherwin, J.L. Sievers, S.M. Simon, S.T. Staggs, J.R. Stevens, R. Thornton, J. Van Lanen, E.M. Vavagiakis, J.T. Ward, and E.J. Wollack. Advanced ACTPol cryogenic detector arrays and readout. *Journal of Low Temperature Physics*, 2016.
- [43] GC Hilton, John M Martinis, KD Irwin, NE Bergren, DA Wollman, ME Huber, S Deiker, and SW Nam. Microfabricated transition-edge X-ray detectors. *Applied Superconductivity, IEEE Transactions on*, 11(1):739–742, 2001.
- [44] S. P. Ho, C. G. Pappas, J. Austermann, J. A. Beall, D. Becker, S. K. Choi, R. Datta, S. M. Duff, P. A. Gallardo, E. Grace, M. Hasselfield, S. W. Henderson, G. C. Hilton, J. Hubmayr, B. J. Koopman, J. V. Lanen, D. Li, J. McMahon, F. Nati, M. D. Niemack, P. Niraula, M. Salatino, A. Schillaci, B. L. Schmitt, S. M. Simon, S. T. Staggs, J.R. Stevens, J. T. Ward, E. J. Wollack, and E. M. Vavagiakis. The first multichroic polarimeter array on the Atacama Cosmology Telescope: Characterization and performance. *Journal of Low Temperature Physics*, 2016.
- [45] Wayne Hu and Scott Dodelson. Cosmic Microwave Background anisotropies. *Annual Review of Astronomy and Astrophysics*, 40:171, 2002. Copyright - Copyright Annual Reviews, Inc. 2002; Last updated - 2014-05-24.
- [46] Wayne Hu and Martin White. A CMB polarization primer. *New Astronomy*, 2(4):323–344, 1997.

- [47] J Hubmayr, JW Appel, JE Austermann, JA Beall, D Becker, BA Benson, LE Bleem, JE Carlstrom, CL Chang, HM Cho, et al. An all silicon feedhorn-coupled focal plane for cosmic microwave background polarimetry. *Journal of Low Temperature Physics*, 167(5-6):904–910, 2012.
- [48] Kazuhide Ichikawa, Toyokazu Sekiguchi, and Tomo Takahashi. Primordial helium abundance from CMB: A constraint from recent observations and a forecast. *Physical Review D*, 78(4):043509, 2008.
- [49] KD Irwin. Squid multiplexers for transition-edge sensors. *Physica C: Superconductivity*, 368(1):203–210, 2002.
- [50] KD Irwin, GC Hilton, DA Wollman, and John M Martinis. Thermal-response time of superconducting transition-edge microcalorimeters. *Journal of Applied Physics*, 83(8):3978–3985, 1998.
- [51] Kent D Irwin and Gene C Hilton. Transition-edge sensors. In *Cryogenic particle detection*, pages 63–150. Springer, 2005.
- [52] R Keisler, S Hoover, N Harrington, JW Henning, PAR Ade, KA Aird, JE Austermann, JA Beall, AN Bender, BA Benson, et al. Measurements of sub-degree b-mode polarization in the cosmic microwave background from 100 square degrees of sptpol data. *arXiv preprint arXiv:1503.02315*, 2015.
- [53] R Keisler, CL Reichardt, KA Aird, BA Benson, LE Bleem, JE Carlstrom, CL Chang, HM Cho, TM Crawford, AT Crites, et al. A measurement of the damping tail of the cosmic microwave background power spectrum with the South Pole Telescope. *The Astrophysical Journal*, 743(1):28, 2011.
- [54] Soo Hong Kim, Sun Woong Na, N-E Lee, Yun Woo Nam, and Young-Ho Kim. Effect of surface roughness on the adhesion properties of cu/cr films on polyimide

- substrate treated by inductively coupled oxygen plasma. *Surface and Coatings Technology*, 200(7):2072–2079, 2005.
- [55] AG Kozorezov, AA Golubov, DDE Martin, PAJ de Korte, MA Lindeman, RA Hjemmering, and JK Wigmore. Microscopic model of a transition edge sensor as a weak link. *Applied Superconductivity, IEEE Transactions on*, 21(3):250–253, 2011.
- [56] A. Kusaka, T. Essinger-Hileman, J. W. Appel, P. Gallardo, K. D. Irwin, N. Jarosik, M. R. Nolta, L. A. Page, L. P. Parker, S. Raghunathan, J. L. Sievers, S. M. Simon, S. T. Staggs, and K. Visnjic. Modulation of cosmic microwave background polarization with a warm rapidly rotating half-wave plate on the Atacama B-Mode Search instrument. *Review of Scientific Instruments*, 85(2):–, 2014.
- [57] D Larson, J Dunkley, G Hinshaw, E Komatsu, MR Nolta, CL Bennett, B Gold, M Halpern, RS Hill, N Jarosik, et al. Seven-year Wilkinson Microwave Anisotropy Probe (WMAP) observations: power spectra and WMAP-derived parameters. *The Astrophysical Journal Supplement Series*, 192(2):16, 2011.
- [58] Oliver P. Lay and Nils W. Halverson. The impact of atmospheric fluctuations on degree-scale imaging of the Cosmic Microwave Background. *The Astrophysical Journal*, 543(2):787, 2000.
- [59] Di-Jie Li, J Gao, JE Austermann, JA Beall, Daniel Becker, Hyeonwoo Cho, Anna E Fox, Nils Halverson, Jason Henning, GC Hilton, et al. Improvements in silicon oxide dielectric loss for superconducting microwave detector circuits. *Applied Superconductivity, IEEE Transactions on*, 23(3):1501204–1501204, 2013.
- [60] D. Lu and C.P. Wong. *Materials for Advanced Packaging*. Springer, 2008.

- [61] Mathew Madhavacheril, Neelima Sehgal, Rupert Allison, Nick Battaglia, J Richard Bond, Erminia Calabrese, Jerod Caligiuri, Kevin Coughlin, Devin Crichton, Rahul Datta, et al. Evidence of lensing of the Cosmic Microwave Background by dark matter halos. *Physical review letters*, 114(15):151302, 2015.
- [62] Tobias A. Marriage, Viviana Acquaviva, Peter A. R. Ade, Paula Aguirre, Mandana Amiri, John William Appel, L. Felipe Barrientos, Elia S. Battistelli, J. Richard Bond, Ben Brown, Bryce Burger, Jay Chervenak, Sudeep Das, Mark J. Devlin, Simon R. Dicker, W. Bertrand Doriese, Joanna Dunkley, Rolando Dnner, Thomas Essinger-Hileman, Ryan P. Fisher, Joseph W. Fowler, Amir Hajian, Mark Halpern, Matthew Hasselfield, Carlos Hernandez-Monteagudo, Gene C. Hilton, Matt Hilton, Adam D. Hincks, Rene Hlozek, Kevin M. Huffenberger, David Handel Hughes, John P. Hughes, Leopoldo Infante, Kent D. Irwin, Jean Baptiste Juin, Madhuri Kaul, Jeff Klein, Arthur Kosowsky, Judy M. Lau, Michele Limon, Yen-Ting Lin, Robert H. Lupton, Danica Marsden, Krista Martocci, Phil Mauskopf, Felipe Menanteau, Kavilan Moodley, Harvey Moseley, Calvin B. Netterfield, Michael D. Niemack, Michael R. Nolta, Lyman A. Page, Lucas Parker, Bruce Partridge, Hernan Quintana, Erik D. Reese, Beth Reid, Neelima Sehgal, Blake D. Sherwin, Jon Sievers, David N. Spergel, Suzanne T. Staggs, Daniel S. Swetz, Eric R. Switzer, Robert Thornton, Hy Trac, Carole Tucker, Ryan Warne, Grant Wilson, Ed Wollack, and Yue Zhao. The Atacama Cosmology Telescope: Sunyaev-zel'dovich-selected galaxy clusters at 148ghz in the 2008 survey. *The Astrophysical Journal*, 737(2):61, 2011.
- [63] John M Martinis, GC Hilton, KD Irwin, and DA Wollman. Calculation of T_c in a normal-superconductor bilayer using the microscopic-based Usadel theory. *Nuclear Instruments and Methods in Physics Research Section A: Accelerators, Spectrometers, Detectors and Associated Equipment*, 444(1):23–27, 2000.

- [64] J McMahon, JW Appel, JE Austermann, JA Beall, D Becker, BA Benson, LE Bleem, J Britton, CL Chang, JE Carlstrom, et al. Planar orthomode transducers for feedhorn-coupled TES polarimeters. In *Aip Conference Proceedings*, volume 31, page 490, 2009.
- [65] J McMahon, J Beall, D Becker, HM Cho, R Datta, A Fox, N Halverson, J Hubmayr, K Irwin, J Nibarger, et al. Multi-choic feed-horn coupled TES polarimeters. *Journal of Low Temperature Physics*, 167(5-6):879–884, 2012.
- [66] J. McMahon, J. Beall, D. Becker, H.M. Cho, R. Datta, A. Fox, N. Halverson, J. Hubmayr, K. Irwin, J. Nibarger, M. Niemack, and H. Smith. Multi-choic feed-horn coupled TES polarimeters. *Journal of Low Temperature Physics*, 167(5-6):879–884, 2012.
- [67] W. Meyer, M. Grunze, R. Lamb, A. Ortega-Vilamil, W. Schrepp, and W. Braun. Langmuir-blodgett deposited polyimide films on gold and silver surfaces. *Surface Science*, 273(1):205 – 218, 1992.
- [68] HD Microsystems. HD 4100 Process Guide. 2009.
- [69] HD Microsystems. HD PI2545 Process Guide. 2009.
- [70] HD Microsystems. HD PI2611 Process Guide. 2009.
- [71] Sigurd Naess, Matthew Hasselfield, Jeff McMahon, Michael D Niemack, Graeme E Addison, Peter AR Ade, Rupert Allison, Mandana Amiri, Nick Battaglia, James A Beall, et al. The Atacama Cosmology Telescope: CMB polarization at 200 GHz. *Journal of Cosmology and Astroparticle Physics*, 2014(10):007, 2014.

- [72] MD Niemack, PAR Ade, J Aguirre, F Barrientos, JA Beall, JR Bond, J Britton, HM Cho, S Das, MJ Devlin, et al. ACTPol: A polarization-sensitive receiver for the Atacama Cosmology Telescope. *Proc. SPIE*, pages 77411S–77411S, 2010.
- [73] Michael D. Niemack. *Towards Dark Energy: Design, Development, and Preliminary Data from ACT*. Physics PhD thesis, Princeton University, Princeton, NJ, USA, 2008.
- [74] C. G. Pappas, J. Beall, J. Brevick, H. M. Cho, M. J. Devlin, A. Fox, E. A. Grace, G. C. Hilton, J. Hubmayr, K. D. Irwin, J. Klein, D. Li, M. Lungu, L. B. Newburgh, J. P. Nibarger, M. D. Niemack, J. J. McMahon, L. A. Page, B. L. Schmitt, S. T. Staggs, J. Van Lanen, and E. J. Wollack. Optical efficiency and R(T,I) measurements of ACTPol TESes using time domain multiplexing electronics. *Journal of Low Temperature Physics*, 176(5-6):749–754, 2014.
- [75] C.G. Pappas. Towards a 100,000 TES focal plane array:A robust, high-density, superconducting cable interface. *Applied Superconductivity, IEEE Transactions on*, 25(3):1–5, June 2015.
- [76] C.G. Pappas, J. Austermann, J. A. Beall, S. M. Duff, P. A. Gallardo, E. Grace, S. W. Henderson, S.P. Ho, B. J. Koopman, D. Li, J. McMahon, F. Nati, M. D. Niemack, P. Niraula, M. Salatino, A. Schillaci, B. L. Schmitt, S. M. Simon, S.T. Staggs, J. R. Stevens, E. M. Vavagiakis, J. T. Ward, and E. J. Wollack. High-density superconducting cables for Advanced ACTPol. *Journal of Low Temperature Physics*, 2016.
- [77] Arthur L Ruoff, Edward J Kramer, and Che-Yu Li. Improvement of adhesion of copper on polyimide by reactive ion-beam etching. *IBM journal of research and development*, 32(5):626–630, 1988.

- [78] John E Sadleir, Stephen J Smith, Simon R Bandler, James A Chervenak, and John R Clem. Longitudinal proximity effects in superconducting transition-edge sensors. *Physical review letters*, 104(4):047003, 2010.
- [79] John E Sadleir, Stephen J Smith, Ian K Robinson, Fred M Finkbeiner, James A Chervenak, Simon R Bandler, Megan E Eckart, and Caroline A Kilbourne. Proximity effects and nonequilibrium superconductivity in transition-edge sensors. *Physical Review B*, 84(18):184502, 2011.
- [80] Emmanuel Schaan, Simone Ferraro, Mariana Vargas-Magaña, Kendrick M Smith, Shirley Ho, Simone Aiola, Nicholas Battaglia, J Richard Bond, Francesco De Bernardis, Erminia Calabrese, et al. Evidence for the kinematic Sunyaev-Zeldovich effect with ACTPol and velocity reconstruction from BOSS. *arXiv preprint arXiv:1510.06442*, 2015.
- [81] Blake D Sherwin, Joanna Dunkley, Sudeep Das, John W Appel, J Richard Bond, C Sofia Carvalho, Mark J Devlin, Rolando Dünner, Thomas Essinger-Hileman, Joseph W Fowler, et al. Evidence for dark energy from the cosmic microwave background alone using the Atacama Cosmology Telescope lensing measurements. *Physical Review Letters*, 107(2):021302, 2011.
- [82] V Shvarts, Z Zhao, MJ Devlin, J Klein, M Lungu, B Schmitt, and R Thornton. Cryogen-free dilution refrigerator for ACTPol polarization-sensitive receiver. In *Journal of Physics: Conference Series*, volume 568, page 032016. IOP Publishing, 2014.
- [83] Jonathan L Sievers, Renée A Hlozek, Michael R Nolta, Viviana Acquaviva, Graeme E Addison, Peter AR Ade, Paula Aguirre, Mandana Amiri, John William Appel, L Felipe Barrientos, et al. The Atacama Cosmology Tele-

- scope: Cosmological parameters from three seasons of data. *Journal of Cosmology and Astroparticle Physics*, 2013(10):060, 2013.
- [84] Joseph Silk. Cosmic black-body radiation and galaxy formation. *The Astrophysical Journal*, 151:459, 1968.
- [85] WJ Skocpol, MR Beasley, and M Tinkham. Phase-slip centers and nonequilibrium processes in superconducting tin microbridges. *Journal of Low Temperature Physics*, 16(1-2):145–167, 1974.
- [86] KT Story, CL Reichardt, Z Hou, R Keisler, KA Aird, BA Benson, LE Bleem, JE Carlstrom, CL Chang, H-M Cho, et al. A measurement of the cosmic microwave background damping tail from the 2500-square-degree spt-sz survey. *The Astrophysical Journal*, 779(1):86, 2013.
- [87] DS Swetz, DA Bennett, KD Irwin, DR Schmidt, and JN Ullom. Current distribution and transition width in superconducting transition-edge sensors. *Applied Physics Letters*, 101(24):242603, 2012.
- [88] Michael Tinkham. *Introduction to superconductivity*. Courier Corporation, 2012.
- [89] Joel N Ullom and Douglas A Bennett. Review of superconducting transition-edge sensors for x-ray and gamma-ray spectroscopy. *Superconductor Science and Technology*, 28(8):84003–84038, 2015.
- [90] Alexander van Engelen, Blake D Sherwin, Neelima Sehgal, Graeme E Addison, Rupert Allison, Nick Battaglia, Francesco de Bernardis, Erminia Calabrese, Kevin Coughlin, Devin Crichton, et al. The Atacama Cosmology Telescope: Lensing of CMB temperature and polarization derived from cosmic infrared background cross-correlation. *arXiv preprint arXiv:1412.0626*, 2014.

- [91] H.J. van Weers, G. Kunkel, M.A. Lindeman, and M. Leeman. Niobium flex cable for low temperature high density interconnects. *Cryogenics*, (0):1 – 4, 2013.
- [92] Hiromichi Watanabe, Naofumi Yamada, and Masahiro Okaji. Linear thermal expansion coefficient of silicon from 293 to 1000 k. *International Journal of Thermophysics*, 25(1):221–236, 2004.
- [93] K.R. Williams, K. Gupta, and M. Wasilik. Etch rates for micromachining processing-part ii. *Microelectromechanical Systems, Journal of*, 12(6):761–778, Dec 2003.
- [94] KW Yoon, JW Appel, JE Austermann, JA Beall, D Becker, BA Benson, LE Bleem, J Britton, CL Chang, JE Carlstrom, et al. Feedhorn-coupled TES polarimeters for next-generation CMB instruments. In *THE THIRTEENTH INTERNATIONAL WORKSHOP ON LOW TEMPERATURE DETECTORSLTD13*, volume 1185, pages 515–518. AIP Publishing, 2009.
- [95] Azeem Zulfiqar, Andrea Pfreundt, Winnie Edith Svendsen, and Maria Dimaki. Fabrication of polyimide based microfluidic channels for biosensor devices. *Journal of Micromechanics and Microengineering*, 25(3):035022, 2015.